

5-2017

Comparison of RANS Modeling to Dual-Plane PIV Measurements of the Turbulent Tip Vortex Trailed from a Hovering Rotor

Zachary Lietzau

Follow this and additional works at: <https://commons.erau.edu/edt>



Part of the [Aerospace Engineering Commons](#)

Scholarly Commons Citation

Lietzau, Zachary, "Comparison of RANS Modeling to Dual-Plane PIV Measurements of the Turbulent Tip Vortex Trailed from a Hovering Rotor" (2017). *Dissertations and Theses*. 337.
<https://commons.erau.edu/edt/337>

This Thesis - Open Access is brought to you for free and open access by Scholarly Commons. It has been accepted for inclusion in Dissertations and Theses by an authorized administrator of Scholarly Commons. For more information, please contact commons@erau.edu.

COMPARISON OF RANS MODELING TO DUAL-PLANE PIV MEASUREMENTS
OF THE TURBULENT TIP VORTEX TRAILED FROM A HOVERING ROTOR

A Thesis

Submitted to the Faculty

of

Embry-Riddle Aeronautical University

by

Zachary Lietzau

In Partial Fulfillment of the

Requirements for the Degree

of

Master of Science in Aerospace Engineering

May 2017

Embry-Riddle Aeronautical University

Daytona Beach, Florida

COMPARISON OF RANS MODELING TO DUAL-PLANE PIV MEASUREMENTS
OF THE TURBULENT TIP VORTEX TRAILED FROM A HOVERING ROTOR

by

Zachary Lietzau

A Thesis prepared under the direction of the candidate's committee chairmen,
Dr. J. Gordon Leishman and Dr. John Ekaterinaris, Department of Aerospace Engineering,
and has been approved by the members of the thesis committee. It was submitted to the
School of Graduate Studies and Research and was accepted in partial fulfillment of the
requirements for the degree of Master of Science in Aerospace Engineering.

THESIS COMMITTEE



Co-Chairman, Dr. J. Gordon Leishman



Co-Chairman, Dr. John Ekaterinaris



Member, Dr. William Engblom



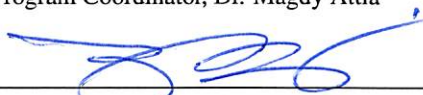
Member, Dr. Tasos Lyrintzis



Graduate Program Coordinator, Dr. Magdy Attia

4.26.2017

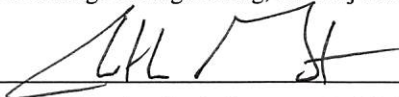
Date



Dean of College of Engineering, Dr. Maj Mirmirani

4/26/2017

Date



Vice Chancellor, Academic Support, Dr. Christopher Grant

4/26/2017

Date

ACKNOWLEDGMENTS

Several individuals helped to make the writing of this thesis possible, and I wish to express my gratitude for all of their support. Firstly, my advisors, Dr. J. Gordon Leishman and Dr. John Ekaterinaris, answered countless questions, sitting down with me for hours at a time to improve my understanding of difficult concepts and steer me in the right direction. Dr. Leishman's vast knowledge in all things rotorcraft along with Dr. Ekaterinaris' expertise in computational modeling provided a wealth of information that was critical in overcoming the challenges presented by this research. My additional committee members, Dr. Engblom and Dr. Lyrintzis, also provided valuable feedback throughout the writing of this thesis, and I am grateful for all of the time and effort they put in to helping me achieve my academic goals.

While the culmination of my academic and extra-curricular experience at Embry-Riddle has shaped me up to this point, two graduate courses can be directly attributed with instilling in me the desire to carry out this thesis. Specifically, Dr. Engblom's course in Computational Fluid Dynamics (CFD) laid the foundation for my understanding of computational modeling, and guidance from himself and Dr. Ekaterinaris has since fueled my passion for the subject. Also, Dr. Leishman's graduate course in rotorcraft aerodynamics was one of the best and most influential classes I have taken, and my decision to pursue this research project stemmed from the inspiration I gained from his instruction of the course.

The extensive computational work carried out for this thesis was made possible through a summer internship with the Army Aviation Development Directorate (ADD) at Ames Research Center under the mentorship of Dr. Roger Strawn, who provided me access to the computing resources made available through the DoD High Performance Computing Modernization Program (HPCMP). During my internship, I had the pleasure of working with Rohit Jain and Dr. Mani Ramasamy, with whom I am submitting a paper to the American Helicopter Society (AHS) Conference. Dr. Buning, one of the key developers of the OVERFLOW research code, kindly provided me with information regarding the various turbulence modeling corrections terms, and Dr. Milluzzo provided additional PIV measurements of the one-bladed rotor wake up to two revolutions. I am grateful to each of them as well.

Lastly, I want to thank all of the close friends I have made in Air Force ROTC, the AIAA Design/Build/Fly team, Fellowship of Christian Athletes, and the Track & Field team. I especially want to thank my roommate and best friend, Dan; my parents, Bill and Diane; my sister, Rae; and most of all, my fiancé, Michelle. She has supported me through countless difficult decisions, including spending the majority of our engagement apart while I complete this thesis in Florida, and she motivates me in all that I do.

TABLE OF CONTENTS

	Page
LIST OF TABLES	vi
LIST OF FIGURES	vii
NOMENCLATURE	x
ABSTRACT	xi
1 Introduction	1
1.1 Background	2
1.2 Best Practices for Rotor Simulations	10
1.2.1 Grid Generation	10
1.2.2 Numerical Discretization	13
1.3 Turbulence Modeling	14
1.4 Outline of the Presented Work	17
2 Methodology	19
2.1 Experiment	19
2.2 Governing Equations	23
2.3 Turbulence Models	34
2.3.1 Spalart-Allmaras (SA)	36
2.3.2 k - ω Shear Stress Transport (SST)	37
2.3.3 Rotational Correction Terms	38
2.4 Numerical Method	43
2.4.1 Implicit Temporal Discretization	44
2.4.2 Spatial Discretization	45
2.5 Numerical Grid	45
2.5.1 Near-Body Grid	47
2.5.2 Off-Body Grid	52
2.5.3 Grid Connectivity	57
2.5.4 Boundary Conditions	60
2.6 Setup for Comparative Analysis	61
2.6.1 Baseline Comparisons	62
2.6.2 Starting Condition	64
3 Results	73
3.1 Computational Cost	73
3.2 Velocity Profiles	74

	Page
3.3 Core Properties	80
3.4 Circulation	84
3.5 Vorticity	86
3.6 Persistence	90
3.7 Turbulence	97
4 Conclusions & Recommendations	106
4.1 Conclusions	106
4.2 Recommendations for Future Work	109
A Locating the Vortex Center	120
B Calculating Core Size and Peak Swirl Velocity	122
C Calculating Vortex Circulation	123
D OVERFLOW Input Files	126
D.1 Namelist Input (over.namelist)	126
D.2 Configuration File (Config.xml)	134
E Fortran 90 Codes	136
E.1 DES Transient Data Averaging	136

LIST OF TABLES

Table	Page
2.1 One-Bladed Rotor Geometry (from Ref. 1).	20
2.2 Grid Comparison for 6th-Order Scheme (FSO=5)	47
3.1 Turbulence Modeling Computational Cost	74

LIST OF FIGURES

Figure	Page
1.1 Flow visualization of tip vortex condensation trails. [Ref. 5]	3
1.2 Schematic outlining key features of a rotor wake. [Ref. 6]	5
1.3 Relaminarization of a vortex core. [Ref. 1]	8
1.4 Some methods for efficiently resolving the vortex wake. [Refs. 21, 22] . . .	12
2.1 Dual-Plane PIV schematic.	21
2.2 Experimental setup showing the Nd:YAG lasers (left) and cameras (right). .	22
2.3 Example transformation from curvilinear to Cartesian coordinates from Ref. 33	27
2.4 Top view of surface grid.	48
2.5 Isometric view of surface grid.	49
2.6 Isometric view of tip grid.	51
2.7 Overlap between tip cap (black) and surface grid (gray).	52
2.8 Cross section of off-body grid colored by vorticity magnitude and plotted with a Q-criterion iso-contour to show extent of wake.	53
2.9 Grid refinement region behind blade tip containing five wake planes.	54
2.10 Initial considerations of AMR colored by vorticity along the x -axis.	56
2.11 Top view of wake modeled using AMR and colored by vorticity magnitude. .	57
2.12 Front view of grid overlap at blade tip.	58
2.13 Overlap with refined OB-grid ($\Delta = 0.00625c$) at blade trailing edge.	59
2.14 Overlap with unrefined OB-grid ($\Delta = 0.05c$) along blade surface.	59
2.15 Baseline comparison incorporating two transitional models for the immediate roll-up at $\zeta = 2^\circ$	63
2.16 Flow field after 2 rotor revolutions from impulsive start.	66
2.17 Flow field after 6.5 rotor revolutions from impulsive start.	66
2.18 Flow field after 11.25 rotor revolutions from impulsive start.	67

Figure	Page
2.19 Flow field after 13.25 rotor revolutions from impulsive start.	67
2.20 Flow field after 20 rotor revolutions from impulsive start.	68
2.21 Balsa dust flow visualization of an impulsively started rotor.	69
2.22 Smoke flow visualization of a rotor wake, approximately 7 revolutions after undergoing a rapid increase in blade pitch.	69
2.23 Flow field after 10 revolutions using inflow start condition.	71
3.1 Effect of grid refinement for inviscid off-body solutions.	76
3.2 Effect of grid refinement for inviscid off-body solutions.	77
3.3 Swirl velocity at 15° of wake age for baseline (inviscid) case, laminar case, and standard turbulence models.	79
3.4 Swirl velocity at 15° of wake age.	80
3.5 Core radius for baseline cases and standard turbulence models.	82
3.6 Peak swirl velocity for baseline cases and standard turbulence models.	82
3.7 Core radius for various turbulence model corrections.	83
3.8 Peak swirl velocity for various turbulence model corrections.	83
3.9 Circulation plotted throughout the refined region.	84
3.10 Circulation plotted throughout the refined region.	85
3.11 Baseline vorticity magnitude comparison at $\zeta = 15^\circ$	87
3.12 SA comparison of vorticity magnitude at $\zeta = 15^\circ$	88
3.13 SST comparison of vorticity magnitude at $\zeta = 15^\circ$	89
3.14 Iso-surfaces of Q-criterion colored by w -velocity for SA case.	90
3.15 Iso-surfaces of Q-criterion colored by w -velocity for SA-R case.	90
3.16 Iso-surfaces of Q-criterion colored by w -velocity for SA-RC case.	91
3.17 Iso-surfaces of Q-criterion colored by w -velocity for SST case.	91
3.18 Iso-surfaces of Q-criterion colored by w -velocity for SST-R case.	92
3.19 Iso-surfaces of Q-criterion colored by w -velocity for SST-RC case.	92
3.20 Experimental flow field measurements of out-of-plane vorticity.	93
3.21 SA-RC prediction of out-of-plane vorticity.	93
3.22 Iso-surfaces of Q-criterion colored by vorticity for SA-DES case.	94

Figure	Page
3.23 Core radius plotted over one complete revolution.	95
3.24 Core radius plotted in refined region up to $\zeta = 15^\circ$	95
3.25 Vortex core growth shown directly following refined grid region.	96
3.26 Top view of tip vortex transition from highly refined to less refined grid.	96
3.27 Distribution of $\sqrt{u'^2}$ from measurements.	98
3.28 Distribution of $\sqrt{v'^2}$ from measurements.	98
3.29 Measurements of the fluctuating in-plane velocity in the vortex core.	98
3.30 Measurements of the Reynolds stress, $\overline{u'v'}$, in the vortex core.	99
3.31 Eddy viscosity distribution for SA case	100
3.32 Eddy viscosity distribution for SA-R case	100
3.33 Eddy viscosity distribution for SA-RC case	100
3.34 Eddy viscosity distribution for SST case	101
3.35 Eddy viscosity distribution for SST-R case	101
3.36 Eddy viscosity distribution for SST-RC case	101
3.37 Reynolds stress approximation of $\overline{u'v'}$ for SA case	102
3.38 Reynolds stress approximation of $\overline{u'v'}$ for SA-R case	102
3.39 Reynolds stress approximation of $\overline{u'v'}$ for SA-RC case	102
3.40 Reynolds stress approximation of $\overline{u'v'}$ for SST case	103
3.41 Reynolds stress approximation of $\overline{u'v'}$ for SST-R case	103
3.42 Reynolds stress approximation of $\overline{u'v'}$ for SST-RC case	103
3.43 Reynolds stress approximation of $\overline{u'v'}$ for SA-DES case	105
A.1 Helicity-based method for determining vortex center.	121
C.1 Grid interpolation used for numerical integration of vortex circulation.	123
C.2 Circulation from experimental measurements.	125

NOMENCLATURE

A	Rotor disk area
c	Blade chord
C_T	Rotor thrust coefficient, $T/\rho A \Omega^2 R^2$
k	Turbulent kinetic energy, $\frac{1}{2}(\overline{u'^2} + \overline{v'^2} + \overline{w'^2})$
r_c	Core radius of the tip vortex
R	Radius of blade
Re_v	Vortex Reynolds number, Γ_v/ν
S_{ij}	Strain rate tensor, $\frac{1}{2}\left(\frac{\partial u_i}{\partial x_j} + \frac{\partial u_j}{\partial x_i}\right)$
u, v, w	Cartesian velocity components
u^*	Friction velocity, $\sqrt{\tau_w/\rho}$
$\overline{u'v'}$	Reynolds shear stress
V_{ax}	Axial velocity of the tip vortex
V_θ	Swirl velocity of the tip vortex
$\sqrt{\overline{u'^2}}, \sqrt{\overline{v'^2}}, \sqrt{\overline{w'^2}}$	RMS velocities
V_{tip}	Tip speed of blade
y^+	Non-dimensional wall distance, u^*d/ν
Γ_v	Total vortex circulation
ζ	Wake age
ν	Kinematic (molecular) viscosity
ν_t	Eddy viscosity
ρ	Air density
σ	Solidity
τ	Shear stress
τ_w	Wall shear stress
Ω	Rotational speed of the rotor
ω	Specific rate of dissipation in $k-\omega$ model
ω_i	Vorticity vector
AMR	Adaptive Mesh Refinement
CFD	Computational Fluid Dynamics
DES	Detached Eddy Simulation
LES	Large Eddy Simulation
PIV	Particle Image Velocimetry
RANS	Reynolds-Averaged Navier-Stokes
SA	Spalart-Allmaras
SST	Shear Stress Transport

ABSTRACT

Lietzau, Zachary MSAE, Embry-Riddle Aeronautical University, May 2017. Comparison of RANS Modeling to Dual-Plane PIV Measurements of the Turbulent Tip Vortex Trailed from a Hovering Rotor.

Numerical simulations using the Reynolds-Averaged Navier-Stokes (RANS) equations were conducted to study the development and turbulent decay of the tip vortices in the wake produced by a hovering rotor. The computational results were compared to detailed, dual-plane Particle Image Velocimetry (PIV) measurements of a turbulent tip vortex trailed from a single-bladed rotor. The work investigated both the required mesh resolution and most suitable turbulence closure models with rotational/curvature corrections by assessing their predictions of the tip vortex properties and the overall physical nature of the rotor wake. It was found that even when using a higher-order accurate central differencing scheme, a minimum off-body grid spacing equal to 0.625% of the chord length was required to accurately predict the core dimension, peak swirl velocity and strength of the tip vortex. The rotational/curvature corrections applied to the Spalart-Allmaras turbulence model better preserved the vortex characteristics to longer wake ages than the same corrections applied to the $k-\omega$ SST model. In both cases, the correction proposed by Spalart and Shur outperformed the simplified correction proposed by Dacles-Mariani et al., with the latter providing little impact on the $k-\omega$ SST model. Lastly, Detached Eddy Simulation (DES) of the wake was studied in addition to the various RANS models with corrections to assess the effect of modeling anisotropic turbulence in the tip vortex.

1. Introduction

The work presented in this thesis has investigated the detailed flow physics of a helicopter rotor wake in the hovering flight condition. Toward this end, Reynolds-Averaged Navier-Stokes (RANS) simulations of a single-bladed rotor were conducted using NASA's state-of-the-art OVERFLOW 2.21 finite difference flow solver. Detailed comparisons were drawn between the computational results and dual plane Particle Image Velocimetry (PIV) measurements of the turbulent tip vortex trailed from the rotor blade [Ref. 1]. The effects of various turbulence closure models with rotational and streamline curvature corrections were studied, along with the spatial resolution and numerical accuracy required to model the mean flow features of the vortex.

In this introductory section, the fluid dynamics of the helicopter rotor wake in hover are briefly reviewed, along with existing research literature pertaining to the CFD modeling of helicopter rotor wakes. Specifically, this section outlines the motivation for this thesis, provides an overview of current "best practices" when using CFD for rotor simulations, and summarizes the relevant turbulence closure models used for the RANS simulations with the various "corrections" to these models that have been developed for application to vortical rotor wake flows.

1.1 Background

Even after decades of analysis and experimentation in the field of rotorcraft aerodynamics, the level of confidence with which helicopter performance can be predicted, at least a priori, is still well below that of conventional airplanes [Ref. 2]. While the levels of predictive engineering confidence for new fixed wing aircraft before they make their first flight is approaching 99%, predictions of helicopters and other rotorcraft can only be made with perhaps 80% confidence. In this context, engineering predictions include performance, loads, and stability and control, among many other things. The consequence is that new helicopters and other rotorcraft generally undergo lengthy development programs after the first flight. Numerous flight tests are often required to progressively improve upon the basic design to eventually meet the intended performance goals of the rotorcraft, whereas airplanes can be brought to service far more quickly. The shortcomings of predictive rotorcraft models result from the inherent difficulty associated with capturing the flow field produced by a rotor.

A helicopter rotor creates a complex, three-dimensional, vortical wake that is dominated by the concentrated vortices trailed from the blade tips. It is the induced velocity field from these vortices that defines much of the aerodynamic loads on the blades and hence the rotor performance, i.e., thrust, power and efficiency. Even with vast improvements in modeling capabilities through Computational Fluid Dynamics (CFD), the detailed flow physics defining a hovering rotor remain too complex to model with guaranteed accuracy. An example of this is seen each year in the hover prediction workshop results presented at

the AIAA SciTech conference [Refs. 3, 4] by the disparate predictions of the rotor wake geometry and rotor performance characteristics.



Figure 1.1 Flow visualization of tip vortex condensation trails. [Ref. 5]

One of the greatest factors limiting the predictive confidence of modern rotorcraft simulations is in their ability to capture the blade tip vortices, which spiral down below the rotor remaining in close proximity to the rotor and airframe, as shown in Fig. 1.1. In this particular image, the vortices are rendered visible by the natural condensation of water vapor in the lower pressure and temperature regions of the vortex cores. Vortices are commonly observed trailing from the wing tips of fixed-wing aircraft as well, but these are left behind the wing and the long term behavior of the vortices does not affect the aircraft, e.g., parts

of the tip vortices that extend 30 or more chord lengths downstream behind the wing will have very little effect.

However, the spiraling or helical form of the path of rotor tip vortices below the rotor makes the wake behavior much more complicated, as the vortices remain in close proximity to the rotor blades and the aircraft as a whole for a relatively long period of time. Time in this context is usually measured in terms of rotor revolutions; the tip vortices may remain close to the rotor for four to six rotor revolutions or hundreds of blade chord lengths, and so the longer term behavior of the vortices becomes more important for a rotor. The blade tip vortices trailed from other blades may also interact with each other, which leads to various distortions of the wake structure from its otherwise nominally helical form in the hover state.

The rotor wake developments are also affected by the airframe (see Fig. 1.1). The airframe not only distorts the wake, but the wake itself can have profound effects on the overall flow on the airframe. Therefore, the modeling of the rotor wake becomes key in the development of aerodynamics models that can predict not only the loads and performance of the rotor(s) but also the aerodynamic characteristics of the entire aircraft.

The wake structure produced by a rotor was first experimentally studied in 1956 by Gray [Ref. 6] using smoke flow visualization, with an outcome being the summary schematic in Fig. 1.2. This interpretation of the hovering rotor wake has formed a basis for much subsequent research, particularly into the characteristics of the blade tip vortices [Ref. 5]. Today, an increasing emphasis is being placed on the accurate prediction of the finer structures found in rotor wakes, such as the vortex sheets [Ref. 7]. But even as measurement capabil-

ities improve, the details of the vortex wake remain elusive to understand, especially as the vortices age in the flow.

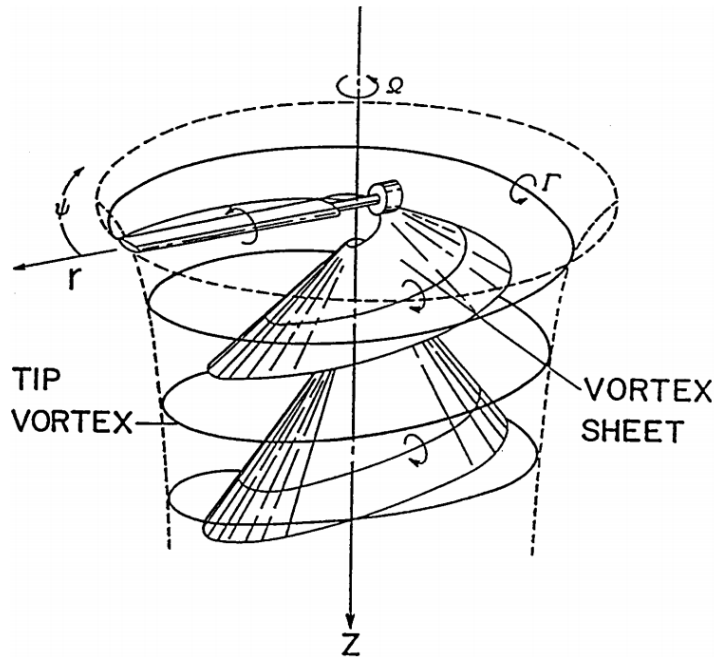


Figure 1.2 Schematic outlining key features of a rotor wake. [Ref. 6]

The rotor wake and the blade tip vortices have far reaching effects beyond affecting rotor performance in hover and forward flight because they interact with the airframe and tail rotor (if one is used). These interactions often lead to adverse effects on aircraft loads and handling qualities (e.g., effects of the rotor wake on the lift produced on the horizontal tail) and are usually a source of vibrations as individual vortices impinge on the airframe surface. Also, noise considerations that have their source in the rotor and its wake have become more important as the need for stealth helicopters grows in the military and the general public remains concerned about the obtrusive nature of rotorcraft noise compared to fixed-wing aircraft.

The foregoing issues demonstrate the need for accurate modeling of the rotor wake and blade tip vortices as they convect throughout the flow surrounding the helicopter. Although many forms of analytical models of vortex wakes have been developed to predict the strength, position and influence of the tip vortices, these models tend to be too generalized to capture the flow details and instabilities developed by the vortices, which meander in the downstream wake in an aperiodic manner [Ref. 8]. The transient characteristics of the longer-term development of the rotor wake are not adequately captured using analytical types of models, including incarnations of momentum theory, dynamic inflow, or even free-vortex wakes [Ref. 5]. While these simpler methods provide a reasonable approximation of the wake and are often used in comprehensive rotorcraft analysis, continued advances in the field of rotorcraft CFD offer the best first-principles based predictive capabilities for modeling the flow.

The most commonly implemented CFD approach for modeling complex aerodynamic problems is through the numerical solution of the Reynolds-Averaged Navier-Stokes (RANS) equations. In the past decades, RANS methods have become well-developed for such rotor flow simulations. However, the RANS equations require closure of the Reynolds stress terms, which is accomplished only by using turbulence models. Two of the most commonly used turbulence models, which have been considered in this thesis, are the Spalart-Allmaras (SA) one-equation model [Ref. 9] and the $k-\omega$ SST two-equation model [Ref. 10]. There are many correction terms and other variations to these well-established one and two-equation turbulence models. However, in practice, the rather ad hoc use of these models including correction terms has lead to inconsistent outcomes and so different interpretations regard-

ing the development of the rotor wake. It is becoming clear that much of the uncertainty in RANS predictions of rotor wakes lies in choosing the most appropriate turbulence model that will accurately capture the formation, structure, and persistence of the tip vortices as they age in the rotor wake.

While several parametric studies have been conducted to analyze the effect of turbulence models on rotor performance [Refs. 11, 12] and similar integrated performance metrics, little research has been done in quantitatively assessing the effect of various available turbulence models in direct comparison to tip vortex measurements. One reason is that only a limited number of measurements of the turbulent flow structure in rotor tip vortices have been made. Turbulence is, by definition, a stochastic process, so turbulence measurements require hundreds or thousands of three-dimensional flow field realizations to be able to acquire the necessary turbulence statistics. Such measurements were performed by Ramasamy et al. [Ref. 1] for a simplified one-bladed rotor and serve as the baseline for the present computational analysis. However, until such measurements become more generally available, especially for a full-scale rotor system, the nature of turbulence in the rotor wake, specifically in the vicinity of the vortex core, cannot be fully understood.

The challenge of modeling turbulence in the vortex becomes clear even on the basis of vortex measurements performed thus far [Refs. 1, 13], which suggest a broad range of scales of non-isotropic turbulence throughout the vortex flow. For example, Fig. 1.3 shows a smoke flow visualization of a developed blade tip vortex in which the inner zone, labeled as “1”, is free of large turbulent eddies, whereas zone “2” is characteristic of a transitional region with eddies of different length scales, and zone “3” shows an outer,

essentially potential flow region [Ref. 1]. A particularly interesting aspect of this image is that the inner region of the vortex flow appears completely smooth and laminar, with almost perfectly circular pathlines. The flow visualization also shows that there is a process of relaminarization of some of the turbulent eddies in the outer region of the vortex as they spiral around the vortex core, the eddies being sheared and stretched in the regions of high streamline curvature. Therefore, the nearly laminar core, as well as the relaminarization of any surrounding turbulence, becomes at least partially responsible for the persistence of the vortices in the rotor wake because it limits the radial spread and diffusion of vorticity.

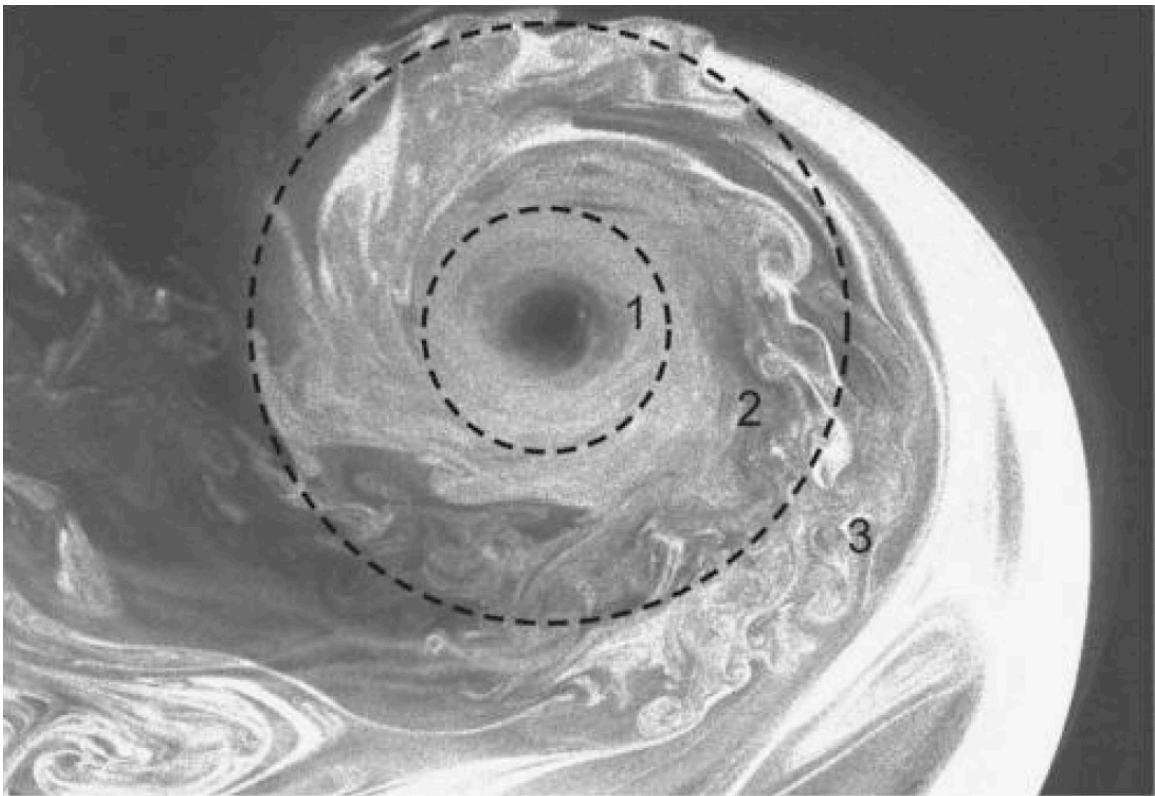


Figure 1.3 Relaminarization of a vortex core. [Ref. 1]

Considering that many RANS turbulence models scale the turbulent eddy viscosity by the value of computed vorticity and a turbulent length scale assumed to be equal to the distance to the nearest wall, it becomes clear as to why RANS simulations tend to overpredict turbulence in the vortex cores [Refs. 14–16]. The net effect of this behavior in the RANS modeling, as opposed to Large Eddy Simulation (LES) or Detached Eddy Simulation (DES), is the more rapid diffusion of the initial concentrated vorticity and the commensurately shorter persistence of the vortices in the rotor wake, perhaps as short as only one rotor revolution.

One consequence of this is that it reduces the induced velocity field from the tip vortices as they are convected away from the rotor, which in turn affects the induced velocity and angles of attack at each of the blade elements, ultimately altering blade loads and rotor performance [Ref. 16]. Although, it must also be noted that deficiencies in the turbulence model are not the only cause of this problem. Numerical methods are not free of dissipation and dispersion errors, thus the spatial discretization also plays a significant role in the distortion of the captured vortices.

A primary goal of the present study was to objectively compare the aforementioned eddy viscosity turbulence models and their respective correction terms to detailed flow measurements in a rotor wake. To this end, the present work compared RANS predictions to dual-plane PIV measurements made on a simplified, one-bladed rotor experiment performed at the University of Maryland [Ref. 1]. This rotor flow field was modeled by the OVERFLOW code [Ref. 17], which has been used extensively for helicopter aerodynamics simulations [Ref. 18]. Several comparisons between the various RANS modeling parame-

ters and flow field measurements were performed to identify the required mesh resolution, order of accuracy, and appropriate turbulence models that lead to acceptable correlations with the measured characteristics of the rotor wake.

1.2 Best Practices for Rotor Simulations

The state-of-the-art modeling capabilities available in OVERFLOW for rotorcraft applications [Ref. 19] are largely due to the overset (Chimera) grid technology and the extensive simulation parameters and tools made available to the user. These options are well documented in the OVERFLOW User's Manual [Ref. 17], which is kept up to date with improvements and additions to the code. Although, proper application of these parameters is a complex task that cannot be fully understood by the manual alone, but only by studying literature that details how to effectively apply the OVERFLOW solver specifically to rotorcraft problems. It is important to note that the purpose of studying best practices regarding solver input parameters is to ensure the computed solution is carried out as close to first principles as possible.

1.2.1 Grid Generation

The first and most perhaps important step in resolving the flow physics is establishing a near-body grid for all components of the rotor geometry. OVERFLOW's overset grid framework can efficiently solve rotor problems by allowing the entire domain to comprise of structured, curvilinear, body-fitted grids and a Cartesian-type background mesh. The

Chimera Grid Tools 2.1 (CGT) software package was utilized to generate the grid around the single rotor blade. Again, the CGT User's Manual [Ref. 20] offers detailed information on each of the grid generation and manipulation tools, but other external literature was relied upon as well to best model the blade geometry.

Near-body structured grids can only be formed in a limited range of topologies. For example, Meakin [Ref. 21] recommends that “cap” and “O”-grid topologies are used for the body-fitted grids, rather than “C”-grids. This is because the “C”-grid retains the fine spacing near the blade surface leading to poor connectivity with the adjacent, uniform off-body mesh. While these topologies of near-body grids continue to be used today, there is now far less restriction on near-body grid size, with single rotor blades commonly using several million grid cells [Ref. 12] to wall spacing that is fine enough to accurately capture near wall flow. This latter requirement typically corresponds to a minimum dimensionless wall distance, y^+ , of less than or equal to one. However, this formulation introduces a quantity referred to as the friction velocity, u^* , and is used to define the viscous sublayer of the turbulent boundary layer.

The OVERFLOW-D code provides a mode that automatically generates and assembles off-body Cartesian-type grids, given a minimum cell size and the far-field boundary positions. Additional control of the off-body grid is available using refinement regions. One level of refinement splits a given cell in half along each dimension, such that one cell is equivalent to eight refined cells.

One method of efficiently capturing the helical nature of the rotor wake is to use a fully cylindrical domain [Ref. 22]. Similarly, one could overset a cylindrical annulus-type

mesh on an otherwise Cartesian background grid [Ref. 21]. These methods (each shown in Fig. 1.4) were used early on when grid size was far more limited by computational restraints. Another example of a cylindrical grid with refinement in the tip vortex region is given by Ref. 23, which introduced an improved algorithm using a fourth-order upwind scheme that better preserved the rotor wake. However, there has been a transition to using entirely Cartesian off-body grids in recent years from the time savings and computer load distribution considerations in parallel processing.

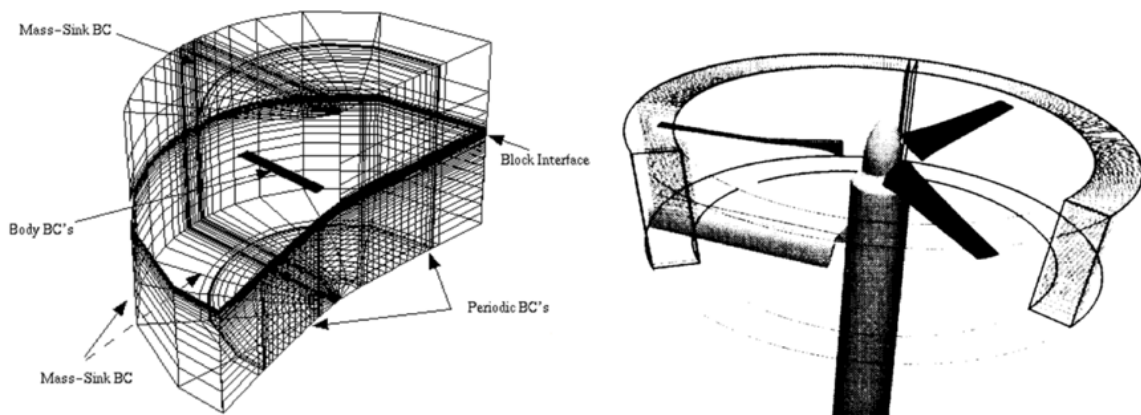


Figure 1.4 Some methods for efficiently resolving the vortex wake. [Refs. 21, 22]

Other researchers have used OVERFLOW's recently implemented adaptive mesh refinement (AMR) feature to more efficiently capture the tip vortex for several revolutions [Ref. 24]. This method actively increases the number of grid cells in areas where the vorticity magnitude exceeds a specified threshold, and decreases the number of cells in areas that fall below a minimum threshold.

The numerical methods themselves also play an important role in the modeling outcomes, as well as the nature of the grids used. For higher order accurate numerical schemes, most authors suggest at least 10–12 grid points in each direction must exist inside the vortex dimension of the vortex core [Ref. 25]. Indeed, measurements suggest that to capture the steep velocity gradients and other rapidly changing flow quantities within the dimensions of the vortex core, at least 10 measurement points are needed. More points would be required for lower-order schemes to ensure that the vortices are not affected by artificial forms of numerical diffusion. For example, a validation study of OVERFLOW modeling a wingtip vortex varied the number of points inside the core from 15 to 30 to maintain the core size and velocity profile. Somewhat contradictory to these recommendations, however, a number of rotor simulations have used a minimum off-body grid spacing of 10% chord [Refs. 25, 26]. The disparity between the high grid resolution required to capture the tip vortex properties and the minimum off-body spacing used in most modern rotor simulations indicates significant latitude for improvement in the computational modeling of the tip vortex throughout the wake.

1.2.2 Numerical Discretization

A detailed explanation of the choices that can be made for temporal and spatial accuracy of the numerical scheme is provided in [Ref. 16]. These simulation parameters allowed for highly accurate prediction of the UH-60 isolated rotor performance in hover. The authors used the Pulliam-Chaussee diagonal algorithm to obtain 2nd-order temporal discretization, noting that a 2nd-order subiteration drop between time steps indicates good convergence.

Also, using a physical time step equivalent to $1/4^\circ$ of a rotor revolution, the number of Newton subiterations was varied from 10–100, showing little change in the solution above 20 subiterations.

State-of-the-art, high-order accurate central differencing discretization is currently obtained in OVERFLOW for certain isolated rotor cases, which use a 6th-order central difference scheme with 8th-order dissipation used for the Euler terms and 2nd-order artificial dissipation used for the and shock capturing [Ref. 18].

1.3 Turbulence Modeling

Turbulent flow is characterized by the presence of a large range of excited length scales, in contrast to the smooth, layered streamlines indicative of the laminar flow regime [Ref. 14]. For this reason, visualization of turbulent flow fields often shows self-similar behavior, in which energy is cascaded from larger to smaller eddies, eventually dissipating through viscous shear stresses at the Kolmogorov scales, i.e., $\eta = (v^3/\epsilon)^{1/4}$, $u_\eta = (v\epsilon)^{1/4}$, and $\tau_\eta = (v/\epsilon)^{1/2}$ [Refs. 27, 28].

In fluids such as air that have a low molecular viscosity, even a small puff of wind or smoke rising from a candle provides enough kinetic energy from buoyancy for turbulent flow to occur. Therefore, accurately modeling the effects of turbulence regarding the viscous diffusion of energy in turbulent rotor wakes is an unavoidable impediment limiting the advancement of rotorcraft simulations.

A brief examination into the current state of turbulence modeling for RANS simulations was conducted to obtain an understanding of existing results and relevant comparisons

between outcomes from different codes. Two turbulence models were examined in more detail and ultimately used in the current study, namely the one-equation model developed by Spalart and Allmaras (SA) [Ref. 9] and the $k-\omega$ SST two-equation model developed by Menter [Ref. 10]. Each model is widely used in research and industrial application because of their computational efficiency and accuracy in predicting a wide range of flow problems. However, it has become apparent that the ability to capturing the physical characteristics of rotor blade tip vortices requires empirically based “correction” terms that have their basis in the physically observed nature of vortex flows, as previously described. To this end, several modifications have been developed and specifically applied to the SA and the $k-\omega$ SST turbulence models to suppress the creation of turbulence in regions of the flow where there is high streamline curvature.

However, the use of these corrective terms seems inconsistent among users in the field of rotorcraft CFD, thereby leading to differences in the development of the vortex flows, as well as the overall rotor wake [Ref. 3]. These differences primarily manifest in the prediction of the tip vortex by an overprediction of the core size, the underprediction of the magnitude and concentration of the vorticity, and the premature radial diffusion of vorticity away from the code compared to physical observations of the rotor wake.

There is published work that has assessed the effect of turbulence modeling parameters on the agreement of integrated parameters such as rotor thrust, power and figure of merit where compared to experimental data. However, much more limited studies have been performed to assess the quantitative accuracy such turbulence models in defining the turbulent nature of actual tip vortices. For example, Ref. 11 and Ref. 12 each study the effect of

turbulence model settings on the predicted rotor efficiency, and the latter also compares the results to a case with a fully inviscid off-body mesh. These outcomes provide valuable insight to the overall effect of turbulence modeling on the integrated rotor performance, but in no way assess the effects on the rotor wake.

Because of the stochastic nature of turbulence and the scale at which the smallest eddies dissipate into heat, it is only feasible to model the effects of turbulence than its exact nature. This is where turbulence models become useful. Rather than solving the full Navier-Stokes equations to capture the intricate, transient features of turbulent flow, the equations are solved numerically for each flow parameter in terms of a time averaged and fluctuating component. Turbulence models then yield the additional terms that time averaging procedure creates, in what are known as the Reynolds-Averaged Navier-Stokes (RANS) equations.

A broad family of turbulence models capture the effect of the fluctuating components of the flows velocity in terms of an eddy viscosity, analogous to the molecular viscosity inherent to every fluid. Most eddy viscosity models utilize the Boussinesq hypothesis, which uses isotropy to significantly simplify the calculations of the six unique components of the fluctuating velocity tensor. However, the deficiencies of this assumption, as addressed in Ref. 14 and others, raise the question of why the focus of this study is on RANS closure models. The answer is simply that the scope has been primarily focused on the common engineering problem of choosing a suitable turbulence model.

An alternative to eddy-viscosity models are the 7-equation Reynolds-stress models, which are available with many commercial CFD solvers, but often fall outside the compu-

tational limitations of the industry professionals and researchers using the CFD software, especially given the complexity of rotorcraft modeling. These models still fundamentally solve for the effect of turbulent flow rather than capturing the transient fluctuations over a range of length scales, but avoid the pitfalls of the Boussinesq assumption by incorporating anisotropy in the turbulent fluctuations. Therefore, the theory behind the Reynolds stress models is acknowledged, but not considered in the present analysis. Additionally, anisotropic (cubic) eddy viscosity models exist, but are far less commonly used. More recently, Large Eddy Simulation (LES) and Detached Eddy Simulation (DES) are becoming increasingly viable options as computational resources improve, the latter being compared to RANS predictions in the present study.

1.4 Outline of the Presented Work

This thesis is organized as follows. The current chapter gives a summary of the problem and prior work. In Chapter 2, the physics and experimental investigations of rotor blade flows is described in greater detail. In Chapter 3, the numerical method including grid generation and turbulence model parameters are given. The results obtained with the adopted numerical approach are shown in Chapter 4 and detailed comparisons with experimental measurements are performed.

It was found that even when using a higher-order accurate central differencing scheme, a minimum off-body grid spacing of 0.625% chord length was required to accurately capture the core dimension, peak swirl velocity and strength of the tip vortex. The rotational/curvature corrections applied to the Spalart-Allmaras turbulence model better pre-

served the vortex characteristics to longer wake ages than the same corrections applied to the k - ω SST model. In both cases, the correction proposed by Spalart and Shur [Ref. 29] outperformed the simplified correction proposed by Dacles-Mariani et al. [Ref. 45], with the latter providing little impact on the k - ω SST model.

While the focus of this research is on RANS closure models, an additional simulation using DES was performed to assess a fundamentally anisotropic turbulence model against the measurements. Even though DES reached better quantitative agreement with the measured distribution of Reynolds stress, it was found that using DES did not improve the mean flow predictions.

2. Methodology

The process of modeling a hovering rotor with enough detail to provide quantitative agreement to experimental measurements proved to be a difficult task, and required many decisions to be made regarding the turbulence modeling parameters, grid size, numerical scheme, and additional simulation settings. This chapter begins by outlining the single-bladed rotor experiment being modeled, and then summarizes the governing equations used for the numerical simulation of the rotor blade, the various turbulence models and corrections employed by the RANS simulation, and finally the numerical discretization of the entire domain using overset grids. Some of the investigations that were conducted throughout this process, such as the outcomes of the grid-independence study and the starting condition used to develop the wake geometry, only provided intermediate conclusions towards the objectives of this study.

2.1 Experiment

The RANS predictions conducted in the present study were validated against flow field measurements that were originally reported by Ramasamy and Leishman [Ref. 1], where the wake behind a hovering, single-bladed rotor was measured using a dual-plane PIV technique (see Figs. 2.1 and 2.2). Most of the rotor parameters used in the experiment are listed in Table 2.1. The single blade rotor system used a counter balance, and was

allowed to teeter freely on a central hinge at the rotational axis. All flow measurements were conducted in a specially designed test cell surrounded by honeycomb flow conditioning screens. The wake was allowed to propagate approximately 18 rotor radii downstream before encountering flow diverters.

Table 2.1 One-Bladed Rotor Geometry (from Ref. 1).

Chord, c	44.5 mm (1.75 in.)
Radius, R	406 mm (16 in.)
Solidity, σ	0.0349
Root Cutout	20%
Airfoil	NACA 2415
Tip Reynolds Number, Re_{tip}	280,000
Tip Speed, V_{tip}	89.28 m/s (292.9 ft/s)
Tip Mach Number, M_{tip}	0.26
Collective Pitch	4.5°
Blade Loading Coefficient, C_T/σ	0.064
Rotational Speed, Ω	70 π rad/s ($f=35$ Hz)

The advantages of using a single-blade rotor system include the ability to create and study a helical vortex filament without interference from tip vortices generated by other blades. Also, a single tip vortex is more spatially and temporally stable than two or more adjacent vortices, thereby allowing the vortex structure to be studied relatively free of the high aperiodicity issues that typically affect multi-bladed rotor experiments. The PIV measurements were suitably corrected for any remaining aperiodicity using the helicity based method, as described by Ramasamy et al. [Ref. 32].

The laser sheets of the PIV system were arranged so as to make measurements on two closely adjacent, parallel planes (see Figs. 2.1, 2.2), simultaneously providing all three components of velocity in one plane and two components of velocity in the second plane.

This approach allowed for several snapshot type measurements of the vortex flow to be compared and phase averaged at effectively coincident spatial locations. Velocity measurements were made at wake ages of 0° , 2° , 4° , 7° , 10° , 15° , 30° , 45° , 90° , and 270° . Notice that the wake age is defined by the angle ζ , in degrees, that the blade has subtended with a given point. Specifically, the plane passing from the axis of the rotor blade through the trailing edge of the blade tip marked a wake age of $\zeta = 0^\circ$, and subsequent wake ages were measured behind the rotor blade from this plane.

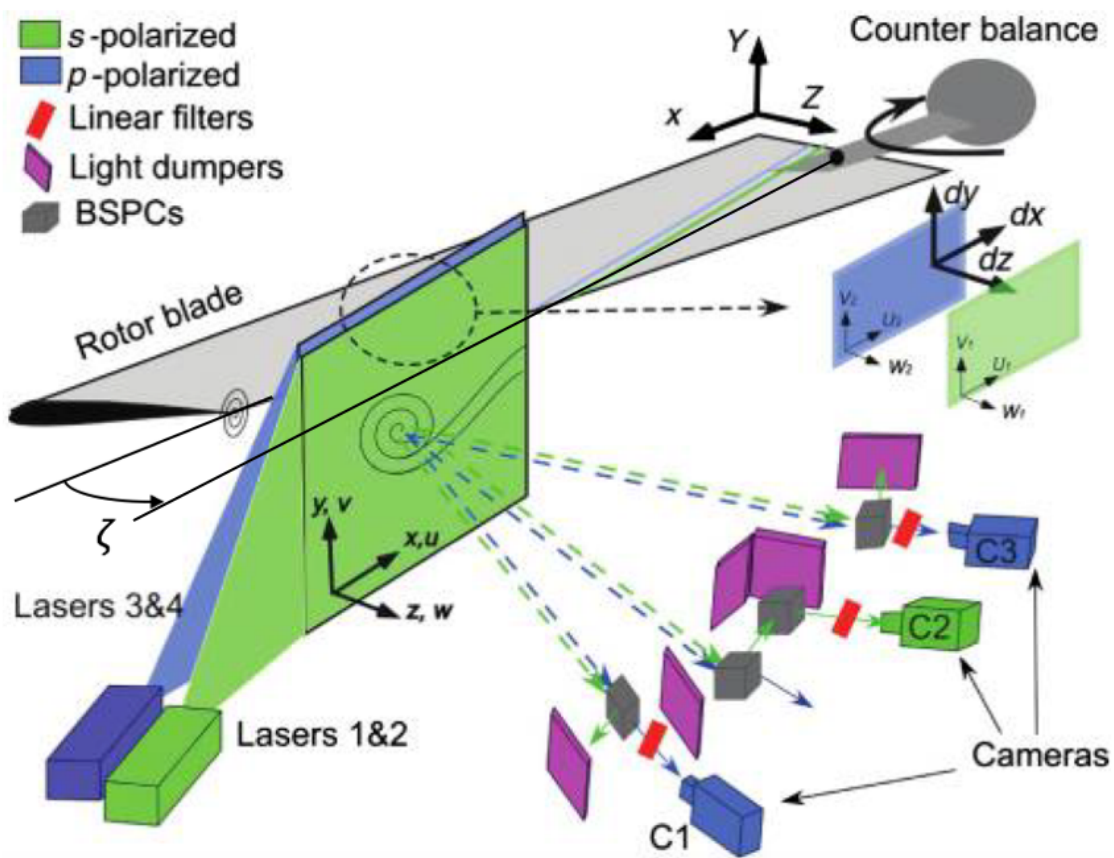


Figure 2.1 Dual-Plane PIV schematic.

The phase-locked, dual-plane particle image velocimetry technique (DP-PIV) used in the measurements consisted of three dual-head Nd:YAG lasers and three cameras as shown in Fig. 2.2.

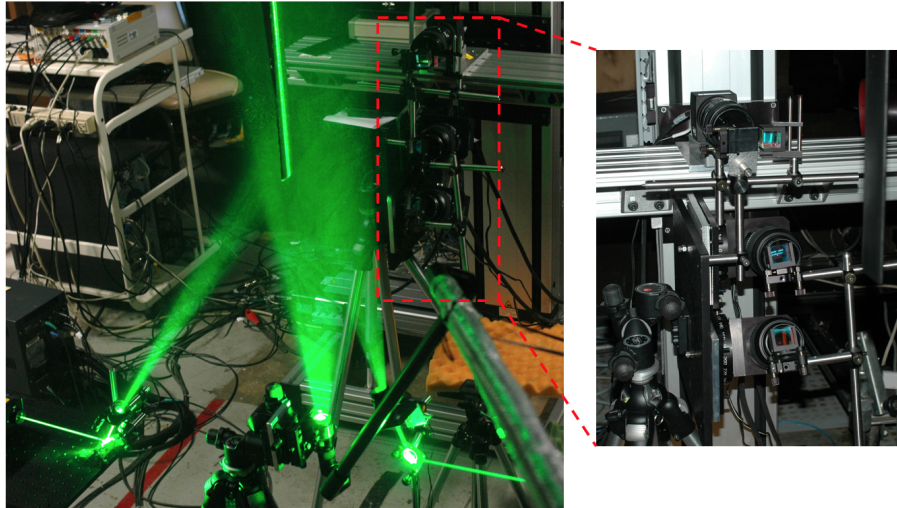


Figure 2.2 Experimental setup showing the Nd:YAG lasers (left) and cameras (right).

The resulting phase-averaged velocity field provided three velocity components in one plane and two components in the second plane. Applying the continuity equation to obtain the final out-of-plane velocity component allowed for all nine components of the strain tensor to be extracted from the measurements. Also, the ability to acquire a significant number of flow field realizations at each wake age (several thousand) allowed for measurements of the first- and second-order turbulent stress terms. In the present study, the strain rate and turbulent stress measurements were compared with RANS predictions along with conventional analysis of tip vortex properties such as core size, peak swirl velocity and circulation.

2.2 Governing Equations

The Navier-Stokes equations model the physical behavior of nearly all fluid flows. In essence, the differential form of these equations applies Newton's second law to a given fluid element in the form of conservation of momentum, i.e.,

$$\rho \frac{Du_i}{Dt} = \frac{\partial p}{\partial x_i} + \frac{\partial \sigma_{ij}}{\partial x_j} \quad (2.1)$$

where the viscous stress is given by $\sigma_{ij} = \mu \tau_{ij} = \mu \left[2S_{ij} - \frac{2}{3} \frac{\partial u_k}{\partial x_k} \delta_{ij} \right]$ and $S_{ij} = \frac{1}{2} \left(\frac{\partial u_i}{\partial x_j} + \frac{\partial u_j}{\partial x_i} \right)$. Tensor notation is used to abbreviate this equation, such that the velocity can be written in its full form as $u_i = (u_1, u_2, u_3) = (u, v, w)$.

The conservation of momentum equation is solved in parallel with the conservation of mass (i.e., continuity equation) and conservation of energy such that the Navier-Stokes equations commonly refer to this set of three conservation equations as a whole. The continuity (conservation of mass) equation is

$$\frac{\partial \rho}{\partial t} + \frac{\partial \rho u_i}{\partial x_i} = 0 \quad (2.2)$$

and the conservation of energy equation is

$$\frac{\partial E}{\partial t} + \frac{\partial}{\partial x_j} [(E + p)u_j - \sigma_{ij}u_i + q_j] = 0 \quad (2.3)$$

where $E = \rho e$ is the internal energy, the heat flux is $q_j = -\frac{\mu}{RePr(\gamma-1)M^2} \frac{\partial T}{\partial x_j}$, and Pr is the Prandtl number, defined as $Pr = C_p \frac{\mu}{\kappa}$.

The Navier-Stokes equations comprise partial differential equations that are non-linear and of mixed first and second-order, making analytical solutions unobtainable. Therefore, these equations can only be solved numerically, which is the purpose of computational fluid dynamics (CFD).

In obtaining a numerical solution to the Navier-Stokes equations, it is useful to write them in vector conservation law form. For example, continuity can be written as

$$\frac{\partial \rho}{\partial t} + \nabla \cdot (\rho \vec{u}) = 0 \quad (2.4)$$

conservation of momentum as

$$\frac{\partial \rho \vec{u}}{\partial t} + \nabla \cdot (\rho \vec{u} \otimes \vec{u}) + \nabla p - \nabla \cdot \vec{\sigma} = 0 \quad (2.5)$$

where $\vec{\sigma} = \mu \left[2\vec{S} - \frac{2}{3}\nabla \cdot \vec{u} \right]$ and $\vec{S} = \frac{1}{2} ((\nabla \vec{u}) + (\nabla \vec{u})^T)$. Lastly, conservation of energy can be written as

$$\frac{\partial E}{\partial t} + \nabla \cdot \left[(E + p)\vec{u} - \vec{\sigma}\vec{u} + \vec{q} \right] = 0 \quad (2.6)$$

These equations, alone, do not exceed the number of unknown fluid properties they require. Therefore, additional equations of state are required for closure of the Navier-Stokes equations. Namely, the equation of state used to close the equations is given as

$$p = (\gamma - 1) \left(E - \frac{1}{2} \rho u_i u_i \right) \quad (2.7)$$

For a rotating reference frame, the time derivative of all vector quantities provide added terms to Eq. 2.1 from the chain rule of differentiation. It can be shown that the inertial time rate of change of a single velocity component (e.g., acceleration along the prescribed x -axis) in a reference frame rotating with a constant speed, Ω , can be calculated as follows for a point at a radial position, r . The two additional terms introduced represent the centrifugal and Coriolis accelerations, respectively, i.e.,

$$\frac{D\vec{V}}{Dt} = \left(\frac{D\vec{V}}{Dt}\right)_{\text{rot}} + \vec{\Omega} \times (\vec{\Omega} \times \vec{r}) + 2\vec{\Omega} \times \vec{V}_{\text{rot}} \quad (2.8)$$

When implemented into the Navier-Stokes equations, the conservation of momentum can then be written in the following form

$$\frac{\partial \rho \vec{u}}{\partial t} + \nabla \cdot (\rho \vec{u} \times \vec{u}) = -\nabla p - \vec{\Omega} \times (\vec{\Omega} \times \vec{r}) - 2\vec{\Omega} \times \vec{V} + \nabla \cdot \vec{\sigma} \quad (2.9)$$

Common practice in CFD is to write the Navier-Stokes equations collectively in conservation law form by collecting the conserved quantities into a single vector, denoted by $\mathbf{Q} = [\rho, \rho u, \rho v, \rho w, E]^T$. The conservation law form of the governing equations for a Cartesian coordinate system is

$$\frac{\partial \mathbf{Q}}{\partial t} = \frac{\partial (\mathbf{F} - \mathbf{F}_v)}{\partial x} + \frac{\partial (\mathbf{G} - \mathbf{G}_v)}{\partial y} + \frac{\partial (\mathbf{H} - \mathbf{H}_v)}{\partial z} \quad (2.10)$$

where \mathbf{F} , \mathbf{G} , and \mathbf{H} are the inviscid flux vectors (from the convective terms in the Euler equations) and \mathbf{F}_v , \mathbf{G}_v , and \mathbf{H}_v are viscous flux vectors. For simplicity, these vectors are

defined below for a 2-dimensional case, but the 3-dimensional equations have a similar form.

$$\mathbf{F} = \begin{bmatrix} \rho u \\ \rho u^2 + p \\ \rho uv \\ u(E + p) \end{bmatrix}, \quad \mathbf{F}_v = \begin{bmatrix} 0 \\ \tau_{xx} \\ \tau_{xy} \\ f_4 \end{bmatrix}, \quad \mathbf{G} = \begin{bmatrix} \rho v \\ \rho v^2 + p \\ \rho uv \\ v(E + p) \end{bmatrix}, \quad \mathbf{G}_v = \begin{bmatrix} 0 \\ \tau_{xy} \\ \tau_{yy} \\ g_4 \end{bmatrix} \quad (2.11)$$

where

$$\begin{aligned} \tau_{xx} &= (4u_x + 2v_y)/3 \\ \tau_{xy} &= (u_y + 2v_x)/3 \\ \tau_{yy} &= (-2u_x + 4v_y)/3 \\ f_4 &= u\tau_{xx} + v\tau_{xy} + \mu Pr^{-1}(\gamma - 1)^{-1} \delta_x a^2 \\ g_4 &= u\tau_{xy} + v\tau_{yy} + \mu Pr^{-1}(\gamma - 1)^{-1} \delta_y a^2 \end{aligned} \quad (2.12)$$

The governing equations can be transformed from Cartesian to generalized curvilinear coordinates using the transformations

$$\tau = t, \quad \xi = \xi(x, y, z, t), \quad \eta = \eta(x, y, z, t), \quad \zeta = \zeta(x, y, z, t) \quad (2.13)$$

This transformation is depicted for a two-dimensional grid in Fig. 2.3 from Ref 33. Applying the chain rule, the temporal and spatial derivatives in the computational domain can be re-written in terms of the variables τ , ξ , η , and ζ . These derivatives are abbreviated using

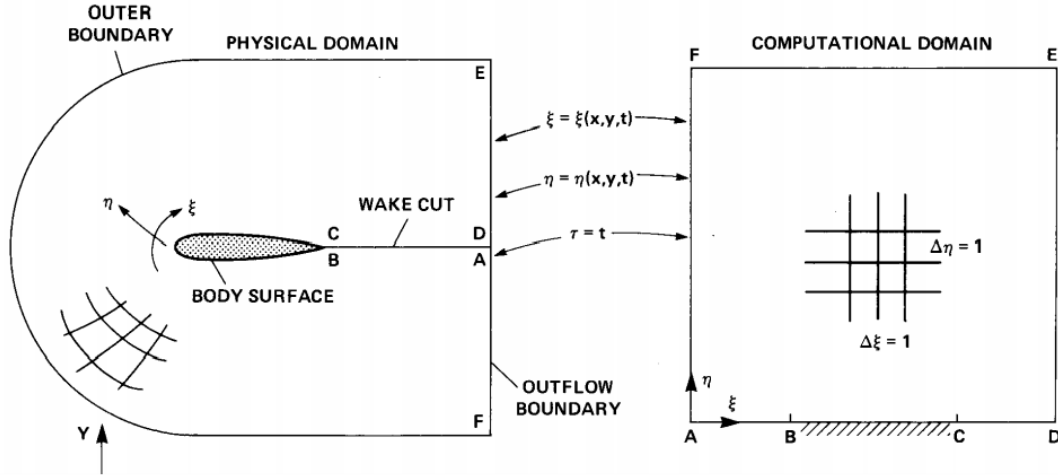


Figure 2.3 Example transformation from curvilinear to Cartesian coordinates from Ref. 33

subscript notation, such that the time derivative is written as $\partial_t = \frac{\partial(\cdot)}{\partial t}$ and the derivative of a spatial x coordinate with respect to computational time can be written as $x_\tau = \frac{\partial x}{\partial \tau}$, and so on. Then, the transformed partial derivatives can be written as

$$\begin{bmatrix} \delta_\tau \\ \delta_\xi \\ \delta_\eta \\ \delta_\zeta \end{bmatrix} = \begin{bmatrix} 1 & x_\tau & y_\tau & z_\tau \\ 0 & x_\xi & y_\xi & z_\xi \\ 0 & x_\eta & y_\eta & z_\eta \\ 0 & x_\zeta & y_\zeta & z_\zeta \end{bmatrix} \begin{bmatrix} \delta_t \\ \delta_x \\ \delta_y \\ \delta_z \end{bmatrix}, \quad (2.14)$$

The inviscid and viscous flux vectors also transform in the curvilinear coordinate system and the conservation law form of the Navier-Stokes equations in generalized curvilinear coordinates can be written as

$$\frac{\partial \hat{Q}}{\partial \tau} = \frac{\partial(\hat{F} - \hat{F}_v)}{\partial \xi} + \frac{\partial(\hat{G} - \hat{G}_v)}{\partial \eta} + \frac{\partial(\hat{H} - \hat{H}_v)}{\partial \zeta} = \text{RHS} \quad (2.15)$$

where the flux vectors are now defined as

$$\hat{Q} = J^{-1} \begin{bmatrix} \rho \\ \rho u \\ \rho v \\ \rho w \\ E \end{bmatrix}, \quad \hat{F} = J^{-1} \begin{bmatrix} \rho U \\ \rho u U + \xi_x p \\ \rho v U + \xi_y p \\ \rho w U + \xi_z p \\ U(E + p) + \xi_t p \end{bmatrix}, \quad (2.16)$$

$$\hat{G} = J^{-1} \begin{bmatrix} \rho V \\ \rho u V + \xi_x p \\ \rho v V + \xi_y p \\ \rho w V + \xi_z p \\ V(E + p) + \xi_t p \end{bmatrix}, \quad \hat{H} = J^{-1} \begin{bmatrix} \rho W \\ \rho u W + \xi_x p \\ \rho v W + \xi_y p \\ \rho w W + \xi_z p \\ W(E + p) + \xi_t p \end{bmatrix}$$

with

$$\begin{aligned}
 U &= \xi_t + \xi_x u + \xi_y v + \xi_z w \\
 V &= \eta_t + \eta_x u + \eta_y v + \eta_z w \\
 W &= \zeta_t + \zeta_x u + \zeta_y v + \zeta_z w
 \end{aligned}
 \tag{2.17}$$

The partial derivatives in the right hand side of the equation (RHS) in Eq. 2.15 are calculated in discrete form using central finite differences to evaluate the derivatives. Therefore, artificial dissipation must be added to avoid nonlinear numerical instability. Time advancement can be obtained using an implicit, discrete, unfactored form [Ref. 34], i.e.,

$$\left[I + \frac{\Delta t}{1 + \theta} (\delta_\xi A + \delta_\eta B + \delta_\zeta C) \right] \Delta Q^{n+1} = \left[\frac{\theta}{1 + \theta} \Delta q^n - \frac{\Delta t}{1 + \theta} RHS^n \right]
 \tag{2.18}$$

where n indicates the time step, $\theta = \frac{1}{2}$ for second-order time accuracy, and

$$A = \frac{\partial F}{\partial Q}, \quad B = \frac{\partial G}{\partial Q}, \quad C = \frac{\partial H}{\partial Q}
 \tag{2.19}$$

define the flux Jacobian matrices.

Direct numerical simulation (DNS) is currently not possible for the complex flows of interest for most engineering applications. Even the resolution of the largest and most prevalent turbulent eddies in such flows (i.e., LES) lies beyond the computational resources of many industry and academic researchers who are attempting full-scale rotorcraft simu-

lations. This is why the RANS equations are far more commonly employed to approximate the behavior of complex, turbulent flow fields.

The general principle behind RANS equations is that the quantities defining highly unsteady, random velocity component, u_i can be decomposed into a mean \bar{u}_i and fluctuating u'_i component, such that $u_i = \bar{u}_i + u'_i$. When this decomposition is substituted into the N-S equations, the time average of the mean and fluctuating components multiplied together drops to zero because the time average of the fluctuating component alone is zero. The time average of the product of two fluctuating components, however, is not zero. With this in mind, the RANS equation for incompressible flow can be written as follows

$$\rho \frac{D\bar{u}_i}{Dt} = \rho \frac{\partial \bar{u}_i}{\partial t} + \rho \bar{u}_j \frac{\partial \bar{u}_i}{\partial x_j} = -\frac{\partial \bar{p}}{\partial x_i} + \mu \frac{\partial^2 \bar{u}_i}{\partial x_j \partial x_j} - \rho \frac{\partial \overline{u'_i u'_j}}{\partial x_j} \quad (2.20)$$

A Reynolds-stress tensor is extracted from this equation as

$$\tau_{ij} = -\rho \overline{u'_i u'_j} \quad (2.21)$$

The Reynolds-stress tensor (Eq. 2.21), representing the time average of the fluctuating components of velocity, introduce six more unknowns. Solving for these values individually results in the full Reynolds stress equation, i.e.,

$$\frac{\partial \tau_{ij}}{\partial t} + \bar{u}_k \frac{\partial \tau_{ik}}{\partial x_k} = -\tau_{ij} \frac{\partial \bar{u}_j}{\partial x_k} - \tau_{jk} \frac{\partial \bar{u}_i}{\partial x_k} + \epsilon_{ij} - \Pi_{ij} + \frac{\partial}{\partial x_k} \left[\nu \frac{\partial \tau_{ij}}{\partial x_k} + C_{ijk} \right] \quad (2.22)$$

where the following additional unknowns are introduced

$$\Pi_{ij} = \overline{p' \left(\frac{\partial u'_i}{\partial x_j} + \frac{\partial u'_j}{\partial x_i} \right)} \quad (2.23)$$

$$\varepsilon_{ij} = 2\mu \overline{\frac{\partial u'_i}{\partial x_k} \frac{\partial u'_j}{\partial x_k}} \quad (2.24)$$

$$C_{ijk} = \overline{\rho u'_i u'_j u'_k} + \overline{p' u'_i} \delta_{jk} + \overline{p' u'_j} \delta_{ik} \quad (2.25)$$

The full Reynolds stress equation (Eq. 2.22) contains a total of 22 new unknowns: 10 from the $\overline{\rho u'_i u'_j u'_k}$ terms, 6 from the $2\mu \overline{\frac{\partial u'_i}{\partial x_k} \frac{\partial u'_j}{\partial x_k}}$ terms, and 6 from the $\overline{u'_i \frac{\partial p'}{\partial x_j} + u'_j \frac{\partial p'}{\partial x_i}}$ terms. This outcome demonstrates the essence of the fundamental closure problem of the RANS equations, rendering the RANS equations unsolvable without the implementation of some semi-empirical closure model for the stress terms [Ref. 14].

For the compressible flow equations to account for the coupling of density in the Reynolds decomposition, Favre averaging is performed. Favre averaging splits a single velocity component, u , as

$$u(\vec{x}, t) = \tilde{u}(\vec{x}, t) + u''(\vec{x}, t) \quad (2.26)$$

so that $\overline{\rho u''} = 0$ where $\overline{(\cdot)}$ is the Reynolds averaging operator. Then,

$$\overline{\rho u} = \overline{\rho \tilde{u}} + \overline{\rho u''} = \overline{\rho \tilde{u}} \quad (2.27)$$

and

$$\tilde{u} = \frac{\overline{\rho u}}{\overline{\rho}} \quad (2.28)$$

Notice that Reynolds averaging for $\overline{\rho uv}$ leads to

$$\overline{\rho uv} = \overline{\rho} \overline{uv} + \overline{\rho u'v'} + \overline{\rho' u'v} + \overline{\rho' v' u} + \overline{\rho' u'v'} \quad (2.29)$$

while Favre decomposition yields

$$\rho uv = \rho(\tilde{u} + u'')(\tilde{v} + v'') = \rho \tilde{u} \tilde{v} + \rho u'' \tilde{v} + \rho v'' \tilde{u} + \rho u'' v'' \quad (2.30)$$

and, therefore, Favre averaging obtains

$$\overline{\rho uv} = \overline{\rho} \widetilde{u\tilde{v}} + \overline{\rho u'' v''} \quad (2.31)$$

This final expression given by Eq. 2.31 is simpler and has the same structure as the conventional Reynolds averaging for uv for constant density (i.e., incompressible) flows, i.e.,

$$\overline{uv} = \overline{u} \overline{v} + \overline{u'v'} \quad (2.32)$$

of which the last term, $\overline{u'v'}$, is simply replaced by $\widetilde{u''v''}$ from Favre averaging.

Performing Favre averaging for the Navier-Stoke equations, continuity can be written as

$$\frac{\partial \overline{\rho}}{\partial t} + \frac{\partial \overline{\rho \tilde{u}_i}}{\partial x_i} = 0 \quad (2.33)$$

conservation of momentum as

$$\frac{\partial \bar{\rho} \tilde{u}_i}{\partial t} + \frac{\partial}{\partial x_j} \left(\bar{\rho} \tilde{u}_i \tilde{u}_j + \bar{p} \delta_{ij} - \bar{\sigma}_{ij} + \bar{\rho} \widetilde{u'_i u'_j} \right) = 0 \quad (2.34)$$

and application of the Favre operator to the total energy, $E = \rho e$, yields,

$$\bar{\rho} \tilde{e} = \frac{\bar{p}}{\gamma - 1} + \frac{1}{2} \bar{\rho} \widetilde{u_i u_i} \quad (2.35)$$

However, there are additional terms in the energy equation for LES [Ref. 35], i.e.,

$$\frac{\partial \bar{\rho} \tilde{e}}{\partial t} + \frac{\partial (\bar{\rho} \tilde{e} + \bar{p}) u_i}{\partial x_j} - \frac{\partial \bar{\sigma}_{ij}}{\partial x_j} + \frac{\partial \bar{q}_j}{\partial x_j} = - \frac{\partial}{\partial x_j} \left[(\overline{\rho u_j e} - \bar{\rho} \tilde{u}_j \tilde{e}) + (\overline{u_j p} - \tilde{u}_j \bar{p}) - \overline{\sigma_{ij} u_j} - \bar{q}_j \right] \quad (2.36)$$

Adopting the eddy viscosity hypothesis, the fluctuating stress term $\bar{\rho} \widetilde{u'_i u'_j}$ in the momentum equation is replaced as

$$\bar{\rho} \widetilde{u'_i u'_j} = \mu_t \left[2 \tilde{S}_{ij} - \frac{2}{3} \frac{\partial \tilde{u}_k}{\partial x_k} \delta_{ij} \right] = \mu_t \tilde{\tau}_{ij} \quad (2.37)$$

Lastly, the additional terms in the energy equation can be ignored for low Mach number flows and the energy equation for the RANS equations becomes

$$\frac{\partial \bar{\rho} \tilde{e}}{\partial t} + \frac{\partial}{\partial x_j} \left[(\bar{\rho} \tilde{e} + \bar{p}) \tilde{u}_j - (\mu + \mu_t) \tilde{\tau}_{ij} \tilde{u}_i - \bar{q}_j \right] = 0 \quad (2.38)$$

2.3 Turbulence Models

Various closure models to the RANS equations are available in the OVERFLOW code. One and two-equation models that simplify the Reynolds-stress calculation by assuming isotropic turbulence through the Boussinesq hypothesis, described later in this section, are used far more commonly than those that solve for each component of the Reynolds-stress tensor. The two models considered in the present work are the SA one-equation model and the $k-\omega$ SST two-equation model. The main difference between two-equation and one-equation models is the lack of the turbulent length scale in the latter [Ref. 14]. One-equation models are generally characterized as being incomplete because they require a specific flow dimension to be assigned as the length scale. In the SA model, this distance is measured from the point where the turbulence quantity is being calculated to the nearest wall. Two-equation models are considered complete because they directly calculate the turbulent length scale. The trade-off between them is that solving two transport equations requires more computational time.

Much of the following information detailing these models is summarized by NASA's Turbulence Modeling Resource [Ref. 36]. Also, an abundance of information on the foundation and development of these models can be obtained from the monogram "Turbulence Modeling for CFD" by Wilcox [Ref. 14] and "Turbulent Flows" by Pope [Ref. 15].

The eddy viscosity turbulence models stem from the Boussinesq hypothesis, which assumes an isotropic distribution of stress in turbulent flow. It introduces an approximate

value of turbulent eddy viscosity, μ_t , analogous to the molecular viscosity of a fluid to populate the Reynolds stress tensor, i.e.,

$$\tau_{ij} = \mu_t \left(2S_{ij} - \frac{2}{3} S_{kk} S_{ij} \right) \quad (2.39)$$

The mean strain rate tensor used here is defined as

$$S_{ij} = \frac{1}{2} \left(\frac{\partial u_i}{\partial x_j} + \frac{\partial u_j}{\partial x_i} \right) \quad (2.40)$$

Rather than forming a separate equation for each independent value of the Reynolds-stress tensor as in Reynolds-stress models, one and two-equation turbulence models have been developed to approximate the eddy viscosity and turbulent kinetic energy, k , in the Boussinesq approximation. While many experimental investigations have addressed the inadequacy of this assumption for flows with separation or swirl, such as the observed anisotropic turbulence in a tip vortex [Ref. 1], eddy viscosity models remain in use because of their simplicity over full Reynolds-stress models.

In general, the majority of turbulence models that have been developed over the years base their equations on dimensional analysis and physical reasoning. However, in seeking robust solutions to the complex problem of turbulence, these models have become overly elaborate. A brief overview of the SA and k - ω SST models is now provided, as well as a description of the various corrections that have been developed to improve their predictive capability for fully separated, vortical flow.

2.3.1 Spalart-Allmaras (SA)

The one-equation SA turbulence model defines the turbulent eddy viscosity as $\nu_t = \tilde{\nu} f_{v1}$, where the empirical function f_{v1} is given by

$$f_{v1} = \frac{\left(\frac{\tilde{\nu}}{\nu}\right)^3}{\left(\frac{\tilde{\nu}}{\nu}\right)^3 + C_{v1}^3} \quad (2.41)$$

The quantity, $\tilde{\nu}$, is determined by the numerical solution of the following transport equation

$$\frac{D\tilde{\nu}}{Dt} = P(\tilde{\nu}) - D(\tilde{\nu}) + \delta(\tilde{\nu}) \quad (2.42)$$

In Eq. 2.42, the production term, $P(\tilde{\nu})$, estimates the rate at which kinetic energy is transferred from the mean flow to turbulence, and is given by

$$P(\tilde{\nu}) = C_{b1}\tilde{\nu}\left(\omega + \frac{\tilde{\nu}}{\kappa^2 d^2} f_{v2}\right) \quad (2.43)$$

Notice that the SA model uses a vorticity, ω , based production term. The diffusion term, $D(\tilde{\nu})$, refers to the diffusion of turbulent energy caused by molecular transport and other processes, and is given by

$$D(\tilde{\nu}) = C_{w1} f_w \left(\frac{\tilde{\nu}}{d}\right)^2 \quad (2.44)$$

Lastly, the dissipation, $\delta(\tilde{\nu})$, represents the rate at which turbulent kinetic energy is converted into heat. This term is a trade-off between the fluctuating part of the strain rate and the fluctuating viscous stresses and is not to be confused with numerical dissipation,

which tends to smooth out sharp gradients in coarser grids. The dissipation term is defined as

$$\delta(\tilde{\nu}) = \frac{1}{\sigma} [\nabla \cdot p(\mathbf{v} + \tilde{\nu}) \nabla \tilde{\nu} + C_{b2} (\nabla \tilde{\nu})^2] \quad (2.45)$$

The constants suggested by Ref. 9 are $C_{v1} = 7.1$, $C_{b1} = 0.1355$, $C_{b2} = 0.622$, $\kappa = 0.41$, $\sigma = 2/3$, and $C_{w1} = \frac{C_{b1}}{\kappa^2} + \frac{1+C_{b2}}{\sigma}$. Besides the eight closure coefficients and three damping functions, four more coefficients and two more functions are included in the model to account for transitional flow effects, as described by Ref. 9.

Notice that the eddy viscosity, ν_t , can become negative depending on the value of $\tilde{\nu}$ (see Eq. 2.41), so the equation requires careful implementation inside actual numerical schemes; see Lorin et al. [Ref. 37].

2.3.2 k - ω Shear Stress Transport (SST)

Menter's k - ω SST model uses two transport equations, one for the turbulent kinetic energy, k , and the second for the specific rate of dissipation, ω , not to be confused with vorticity. This model effectively combines the best characteristics of the k - ω and k - ϵ models. Several turbulence models have been developed with the turbulent kinetic energy, $k \equiv \frac{1}{2}(\bar{u}'^2 + \bar{v}'^2 + \bar{w}'^2)$, at their foundation [Ref. 14].

$$\frac{\partial(\rho k)}{\partial t} + \frac{\partial(u_j k)}{\partial x_j} = P - \beta^* \rho \omega k + \frac{\partial}{\partial x_j} \left[(\mu + \sigma_k \mu_t) \frac{\partial k}{\partial x_j} \right] \quad (2.46)$$

and

$$\frac{\partial(\rho\omega)}{\partial t} + \frac{\partial(u_j\omega)}{\partial x_j} = \frac{\gamma}{\nu_t} P - \beta\rho\omega^2 + \frac{\partial}{\partial x_j} \left[(\mu + \sigma_k\mu_\omega) \frac{\partial\omega}{\partial x_j} \right] + 2(1 - F_1) \frac{\rho\sigma_{\omega 2}}{\omega} \frac{\partial k}{\partial x_j} \frac{\partial\omega}{\partial x_j} \quad (2.47)$$

The two transport equations, given above, closely resemble those implemented in the original k - ω model originally proposed by Wilcox, but with modifications to utilize the k - ϵ model for separated flows. The method by which Menter implemented both the features of the k - ω and k - ϵ models into the k - ω SST model was by multiplying the k - ω transport equation by a blending function F_1 , and the k - ϵ equation by $1 - F_1$. The value of the blending function F_1 was set equal to 1 near the wall where the k - ω model performs best and 0 away from the wall where the k - ϵ model is more applicable.

The term “shear stress transport” comes from the Johnson-King half-equation model [Ref. 14], which only requires the numerical solution of an ordinary differential equation to model the maximum shear stress rather than a partial differential equation. This model was designed exclusively for boundary layers flows, and works well with strong adverse pressure gradients, which strengthens the expected capabilities of the k - ω model in wall-bounded flows.

2.3.3 Rotational Correction Terms

The turbulence models previously described generally perform well for turbulent boundary layers and flows with a limited amount of flow separation, but the problem becomes far more difficult away from the walls. Pure shear flows, especially highly anisotropic cases

with coherent swirling structures which naturally include the blade tip vortices, are classes of flows that are known to be difficult to model using RANS. For these types of flows, eddy viscosity models are hindered by the often indiscernible length scale of the turbulent eddies and the limitations of the Boussinesq hypothesis in assuming isotropic turbulence with a linear stress-strain relationship.

The first challenge in overcoming these deficiencies is in stratifying steady, rotational flow features from turbulent eddies. The second challenge is defining a correction function to the turbulence model in these regions that is physically consistent with the observed (measured) flow. Bradshaw [Ref. 38] originally proposed that the Richardson number be used to stratify flow by its mean streamline curvature, and also applied this principle to the analysis of turbulent flow in cases of high streamline curvature [Ref. 39]. Implementation of this criteria for vortical flows has also been suggested by other researchers such as Wilcox [Ref. 40], Cotel and Breidenthal [Refs. 41, 42], and Ramasamy et al. [Ref. 43].

An inertial form of the Richardson number, Ri , is given by

$$Ri = \frac{2v_\theta}{r^2} \frac{\partial v_\theta r}{\partial r} \bigg/ \left(r \frac{\partial v_\theta r}{\partial r} \right)^2 \quad (2.48)$$

where the vortex Reynolds number is $Re_v = \Gamma_v/\nu$. Empirical studies have found that there is a threshold where turbulence occurs inside a vortex when the local Richardson number exceeds a $Re_v^{1/4}$ as documented by [Ref. 42] and also verified by Ramasamy et al. [Ref.

43]. Hellsten [Ref. 44] proposed an implementation of the Richardson number correction to the k - ω SST model by redefining the Richardson in the following form

$$Ri = \frac{|\omega|}{|S|} \left(\frac{|\omega|}{|S|} - 1 \right) \quad (2.49)$$

where $|\omega|$ denotes the vorticity magnitude and $|S|$ denotes the strain rate magnitude. While this correction is not currently available in OVERFLOW, the general principles help to relate the experimental work to some of the more complex turbulence correction terms. Also, this Richardson number criteria for stratifying flow with high mean streamline curvature has not been used directly in the corrections being considered in this study. It was found, however, that it helps to provide an understanding of the equations that are used by these corrections to reduce turbulence in the vortex core.

An overview of the correction terms currently available for use in the OVERFLOW code is given in Ref. 45 and is now briefly described. The first is labeled “General Rotational Correction” (IRC=2 option in the OVERFLOW namelist input), and is referred to throughout this work with a “-R” extension (e.g., SA-R and SST-R). The second term is labeled the “Spalart-Shur Rotation/Curvature Correction” (IRC=1 option), and is referred to in this work as a “-RC” extension (e.g., SA-RC and SST-RC).

General Rotational Correction (IRC=2)

For the general rotational flow correction applied to the Spalart Allmaras model, the correction function denoted as f_{r1} can be implemented by direct multiplication to the turbulence production term. The production term in the SA model now becomes

$$P(\tilde{\nu}) = C_{b1}\tilde{\nu} \left(\Omega + \frac{\tilde{\nu}}{\kappa^2 d^2} f_{v2} \right) f_{r1} \quad (2.50)$$

and the production term in the k - ω SST transport equations, P_k (as defined by Ref. 10) takes the form

$$P_k = \mu_t S_{ij}^2 f_{r1} \quad (2.51)$$

Dacles-Mariani et al. [Ref. 45] proposed a simplified vorticity-strain substitution to reduce eddy viscosity in regions of pure flow rotation. This approach is the simplest correction currently available for rotational flow.

This correction term was developed for use with the SA model, with the idea being initially suggested by Spalart [Ref. 45], and formal validation studies have been carried out for the SA implementation [Ref. 31]. Although, the same methodology described in the original paper has been followed to include the term into the SST model as well, as described in Ref. 46. The correction function in either case can be written as a function of r^* , i.e.,

$$f_{r1}(r^*) = 1 + C_{\text{rot}} \min(0, r^* - 1) \quad (2.52)$$

where

$$r^* = |S|/|\boldsymbol{\omega}| \quad (2.53)$$

Notice that this definition of r^* can be substituted into the Richardson number defined by Eq. 2.49 to obtain

$$Ri = \frac{1}{r^*} \left(\frac{1}{r^*} - 1 \right) \quad (2.54)$$

The empirical constant C_{rot} is given a value of 2 in [Ref. 31] and [Ref. 45]. The magnitude of the strain is then calculated using

$$|S| = \sqrt{2S_{ij}S_{ij}} \quad (2.55)$$

Spalart-Shur Rotation/Curvature Correction (IRC=1)

The rotational/curvature correction proposed by Spalart and Shur [Ref. 29] is more mathematically involved, but still widely used in practice. Their work is largely based on the investigation of streamline curvature performed by Knight and Saffman [Ref. 47], essentially modeling the “gyroscopic stability effect” referred to in their paper. This approach is accomplished through an empirically based transport equation of the ratio of strain rate magnitude to vorticity magnitude.

While the SA-RC makes no explicit mention of the Richardson number, both Ref. 29 and Ref. 47 cite the original work done by Bradshaw. With this in mind, Spalart and Shur defined the rotational correction function f_{r1} as documented in Ref. 29, i.e.,

$$f_{r1}(r^*, \tilde{r}) = (1 + C_{r1}) \frac{2r^*}{1 + r^*} [1 - C_{r3} \arctan C_{r2} \tilde{r}] - C_{r1} \quad (2.56)$$

with the additional variable, \tilde{r} , defined by a separate function of strain rate and vorticity as given by

$$\tilde{r} = \frac{2\omega_{ik}S_{ik}}{D^4} \left(\frac{DS_{ij}}{Dt} + (\epsilon_{imn}S_{jn} + \epsilon_{jmn}S_{in})\Omega'_m \right) \quad (2.57)$$

where $D^2 = \frac{1}{2}(|S|^2 + |\omega|^2)$ and Ω'_m is the rotation rate of the reference frame. In dealing with rotorcraft simulations, this value is often set equal to the rotational velocity of the rotor. The constants and additional calculations suggested for the SA model are given in Ref. 29.

Smirnov and Menter describe an implementation of the SA-RC term for the $k-\omega$ SST model in [Ref. 48], when they modified the empirical coefficients to $C_{r1} = 1.0$, $C_{r2} = 12$, and $C_{r3} = 1.0$ and defining $D^2 = \frac{1}{2}(S^2 + 0.09\omega^2)$. However, at the time of this writing the SA-RC correction applied to the $k-\omega$ model is by direct application of the function, f_{r1} , as described previously.

2.4 Numerical Method

The computational model used a non-inertial reference frame and non-dimensional variables that correlate to the experimental parameters [Ref. 17], such that one unit of

length in the computational domain was equal to the blade chord length of 44.5 mm used for the rotor system. The remainder of this section outlines the solver inputs required to obtain a time-accurate solution to the RANS equations using OVERFLOW.

2.4.1 Implicit Temporal Discretization

The RANS equations were advanced in time using 2nd-order temporal accuracy with the Pulliam-Chaussee [Ref. 49], pentadiagonal ADI solver. The time step was chosen to correspond to 0.25° of blade rotation, and within each time step, 20 subiterations were performed using a dual time stepping procedure in the near-body grids. The dual time stepping allowed each temporal subiteration to maintain a specified CFL number of 10 in the blade surface grid region and 5 in the root and tip grids. The off-body grids used a local time-step factor of 2 to improve computational efficiency. Convergence was ensured by a 3.5-order subiteration drop in the flow field each time step, and the L_2 norm of the residuals dropped to the order of 10^{-10} for both the off-body and near-body grids.

To apply the implicit algorithm, the strong conservation-law form of the Navier-Stokes equations is written in delta form [Ref. 49] and the following implicit approximate factorization scheme is employed.

$$\left[I + h\delta_\xi \hat{A}^k \right] \left[I + h\delta_\eta \hat{B}^k \right] \left[I + h\delta_\zeta \hat{C}^k \right] \Delta \hat{Q}^k = -hR^{k,n} + D \quad (2.58)$$

where

$$R^{k,n} = \frac{3\hat{Q}^k - 4\hat{Q}^n + Q^{n-1}}{2\Delta t} + (\hat{F} - \hat{F}_v)_\xi^k + (\hat{G} - \hat{G}_v)_\eta^k + (\hat{H} - \hat{H}_v)_\zeta^k \quad (2.59)$$

$$h = \frac{2\Delta t \Delta \tau}{2\Delta t + 3\Delta \tau} \quad (2.60)$$

and D is the numerical dissipation.

2.4.2 Spatial Discretization

Evaluation of the convective terms was obtained by employing 4th or 6th-order central differencing (FSO=3 and FSO=5 options respectively in the OVERFLOW input). The artificial dissipation used to maintain the stability of this numerical scheme was 6th-order, and the overset grid methodology used trilinear interpolation (i.e., three overlapping nodes) to maintain higher-order numerical accuracy between adjacent grids. However, to maintain reasonable computational cost, the viscous terms were discretized with 2nd-order accuracy so that, overall, the spatial discretization of the OVERFLOW code is formally 2nd-order accurate. The 4th-order central differencing scheme (FSO=3) for the convective terms was used to develop the solution over the first 12 rotor revolutions, and provided a baseline comparison for the effect of the high-order numerical scheme on the wake solution.

2.5 Numerical Grid

Every conventional form of numerical discretization, whether using a finite volume, finite element, or finite difference solution method, is performed on a numerical mesh. The calculations performed for this thesis apply OVERFLOW's finite different approach to curvilinear structured meshes with an overset Cartesian background mesh. The over-

set mesh methodology of OVERFLOW allows only for structured-type grids to be used exclusively throughout the computational domain.

These grids had to accommodate a very broad range of length scales, to efficiently capture the entire flow field with sufficient detail, and to adequately resolve and preserve the tip vortex core and shear layers. The extent of the Cartesian mesh is 20 rotor radii in each direction from the rotational axis. Within this domain, regions of very fine spacing behind the trailing edge of the blade tip were required to capture the formation of the vortex. This was achieved through mesh refinement of the Cartesian-type background mesh.

Given the resolution required to resolve and model the tip vortex, one may ask why the present study models the entire flow field encompassing the rotor. Indeed, several computational analyses of the tip vortex, such as Refs. [Ref. 50] and 46, have been carried out at a much smaller scale only in the vicinity of a blade or wing tip. However, outside of research and academia, the grid scale obtained by these studies is rarely obtained in industrial modeling of most practical engineering flows. Rather, full flow field simulations are commonly performed with an emphasis on integrated performance measurements rather than detailed analysis of the vortex wake. The present study intends to bridge the gap between these two methods by modeling the entire rotor wake, but refining the near-wake close to the resolution of the unique, available PIV measurements [Ref. 1]. The following sections describe the near-body and off-body meshes employed for the simulations.

2.5.1 Near-Body Grid

Table 2.2 outlines the total grid size and computational wall-time for various levels of refinement. The third case, with $\Delta = 0.00625c$, was chosen for each of the fully developed simulations in the present study.

Table 2.2 Grid Comparison for 6th-Order Scheme (FSO=5)

OB Spacing	Grid Points	Wall Clock Time[†]/Rev (hr:min)
$\Delta_{\min} = 0.025c$	66.8M	5:16
$\Delta_{\min} = 0.0125c$	68.7M	5:32
$\Delta_{\min} = 0.00625c$	83.5M	6:26
$\Delta_{\min} = 0.005c$	151.7M	13:18

[†]Wall clock times for 3,456, 2.7 GHz, Intel Xeon E5-2697v2 cores.

The three, overlapping, body-fitted grids were developed using Chimera Grid Tools (CGT). They consisted of an O-shaped grid encompassing the surface of the blade, a root cap and a tip cap, each of which was generated by extrusion of a two-dimensional surface grid. This mesh defining the blade surface from root to tip was created using a C++ code, which linearly interpolated points onto the rotor geometry based on the NACA 2415 airfoil coordinates used in the experiment and chosen spanwise sections.

The spanwise grid spacing was prescribed using four such sections between the root cutout at $0.15R$ and the blade tip. The first section began at the blade root, bringing the spacing from $0.0005c$ at the root cutout to $0.01c$ at the beginning of the second section, which maintained this cell size from $0.22R$ to $0.9R$. A third section reduced the spacing to $0.005c$ at $0.96R$ for better refinement near the tip. Then, a final section, further refined the

spanwise grid spacing to $0.00025c$ at the blade tip, this approach is illustrated by the top view of the blade shown in Fig. 2.4, with the sections labeled in the order described above.

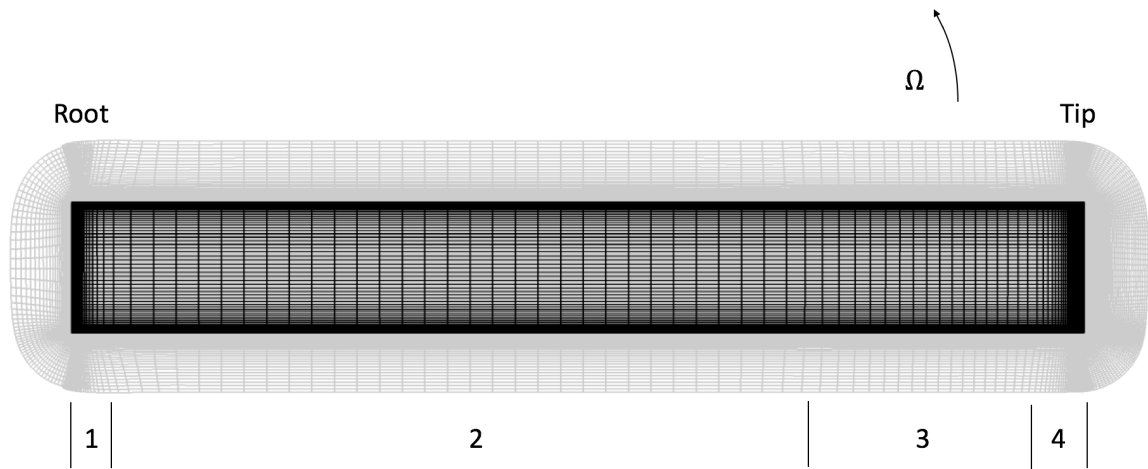


Figure 2.4 Top view of surface grid.

The chordwise spacing was maintained throughout the span of the blade, with a minimum spacing at the trailing edge of $0.0002c$, allowing for 9 nodes to be placed along the blunt trailing edge, and a spacing of $0.0005c$ at the leading edge. This approach allowed for accurate modeling of the streamwise gradient and the pressure distribution over the blade's leading edge and upper and lower surfaces. Also, the densely packed region behind the trailing edge allowed for the detailed resolution of the wake.

The surface grid was extruded normal to the blade using CGTs "HYPGEN" hyperbolic mesh generator. The HYPGEN input used the "splay-type" boundary conditions at the blade root and tip to ensure that the extrusion wrapped each layer of the tip grids inward over the blade surface. This extrusion methodology ensured sufficient overlap between the grids that a scheme of high-order spatial accuracy would require. Also, to improve

the size agreement in the overlapping region between the near-body grids, two layers were removed from the root and tip of the surface grid, as shown in Figs. 2.4 and 2.5, by direct manipulation of the plot3D unstructured data files. The resulting volume grid contained 1.63 million nodes over the blade surface alone.

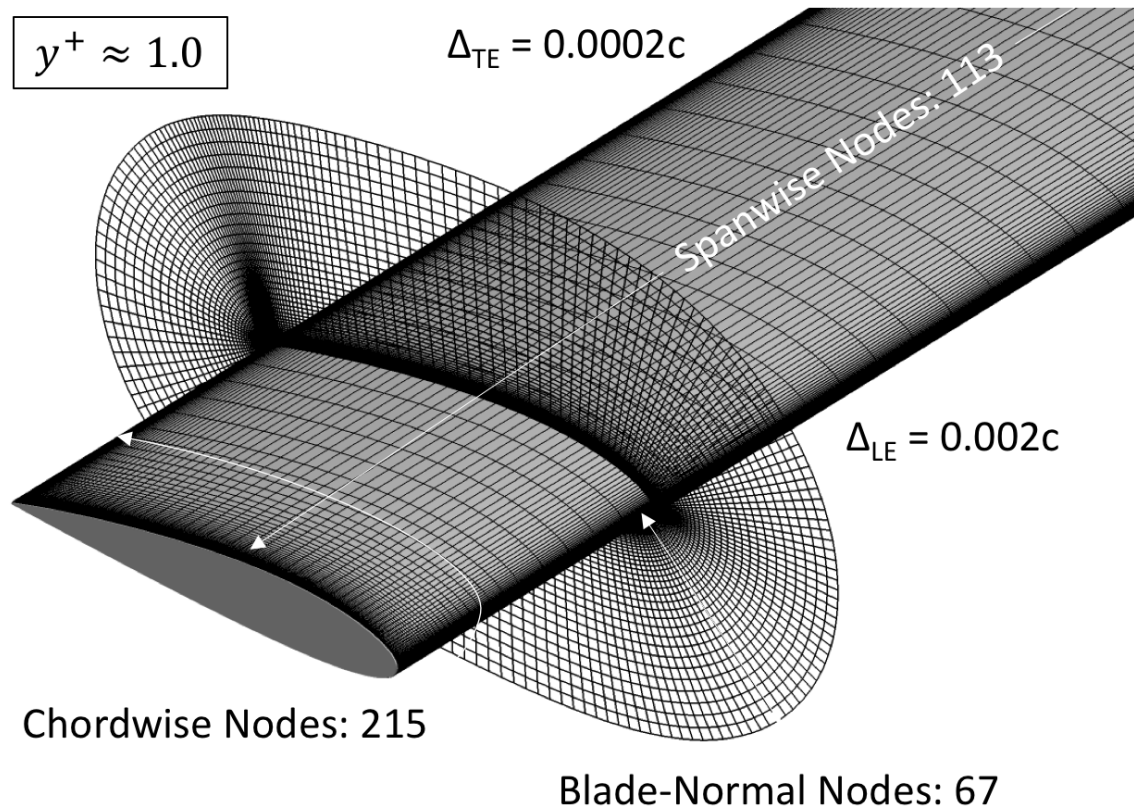


Figure 2.5 Isometric view of surface grid.

While near-body grids typically extend one or more chord lengths from the blade surface, the present grid extended only half of a chord length. This choice of reducing the volume of the body-fitted, curvilinear grid allowed for the numerical solution to be efficiently transferred from the near-body grid to the refined Cartesian-type wake mesh. The

minimum spacing normal to the wall had a value of $7.882 \times 10^{-5}c$, allowing for a y^+ value equal to 1.0, and the number of nodes in the extruded direction was set to 67. This value was chosen because it provided a smooth transition from the fine spacing near the surface to roughly cubical cells further from the wall, while efficiently capturing the flow over the blade. Overlap between the near-body and off-body grids is further analyzed in the following section addressing the off-body Cartesian-style mesh.

The tip grid originated from a root and tip “cap” surface topology. These were generated using the TIPCAP function in CGT, by varying the resolution and smoothing parameters to obtain a well-formed surface cap. Nine points were used along the blunt trailing edge, matching the nodes along the blade surface to improve resolution of the wake. Again, this two-dimensional grid was extruded normal to the blade, with the tip cap being more densely packed than at the root. The boundary layer spacing was again set to a minimum value of $7.882 \times 10^{-5}c$ to ensure a y^+ value of 1.0. The tip grid shown in Fig. 2.6 contains roughly 713,000 nodes.

The overlap between the tip and blade grids is shown in Fig. 2.7. Notice that the surface extends out beyond the root and tip of the blade, while the caps wrap inward over the blade’s surface. This approach was required to exceed the minimum number of overlapping nodes utilized by the higher-order numerical scheme. The overset grid methodology requires that a certain number of points at the boundary of a grid (usually 2–4, depending on the order of the scheme) to have an adjacent donor, or essentially another point from which the solution can be interpolated. Boundary nodes without overlapping donor cells from a nearby mesh are referred to as orphans, and must be avoided because they have an adverse effect on the

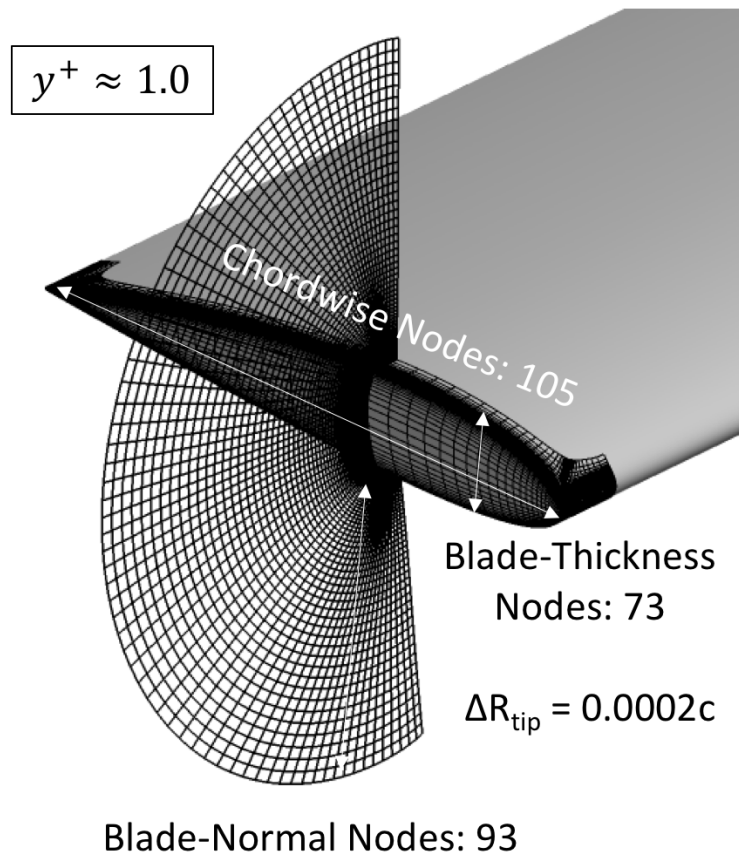


Figure 2.6 Isometric view of tip grid.

solution. In the grids used by the present study, orphan points were avoided entirely to mitigate any potential sources of inaccuracy.

The total size of the body-fitted grid over the blade was 2.7 million nodes. Development of the grid required several iterations with a focus on improving the transition region to the refined off-body grids, especially behind the trailing edge of the blade tip. The near-body grid did not require a formal grid-independence study because the 2.7 million nodes used within a volume extruded only $0.5c$ from the surface far exceeded the grid size required to

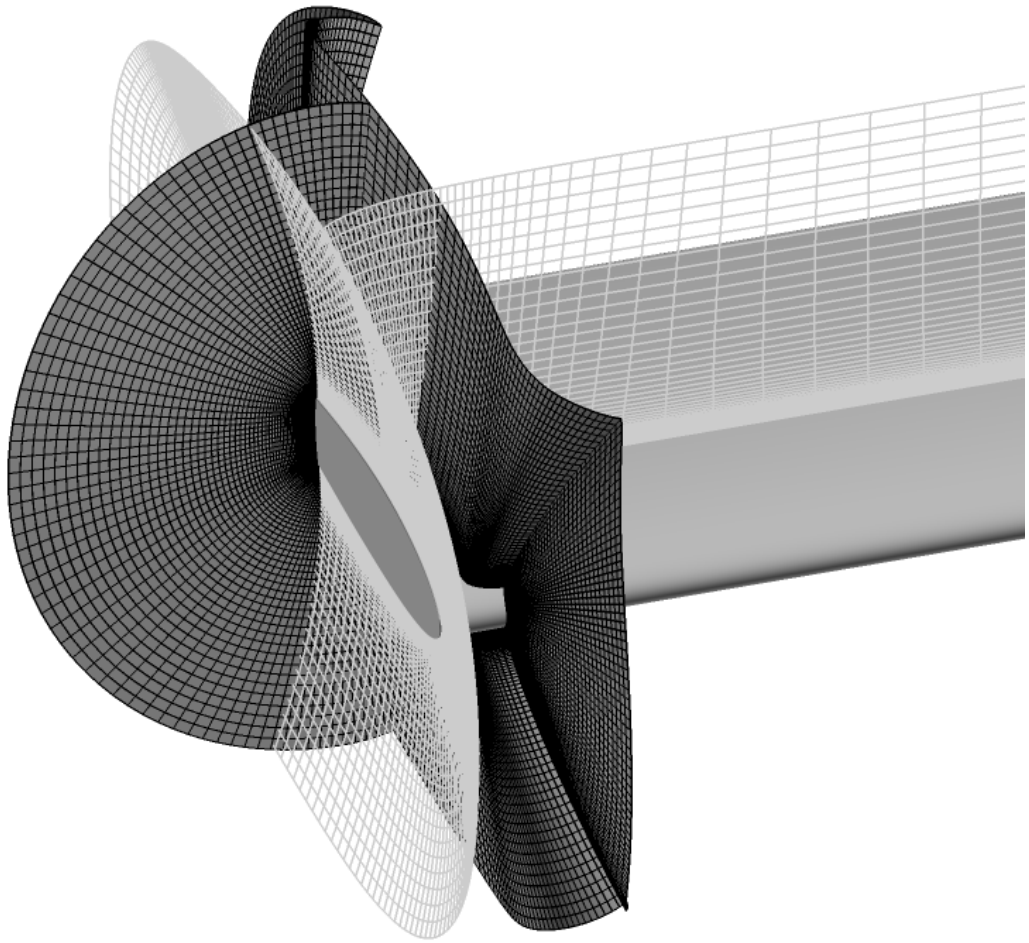


Figure 2.7 Overlap between tip cap (black) and surface grid (gray).

accurately model the flow over the blade. Rather, the primary focus in refining the grid to this size was to model the formation of the tip vortex in as much detail as possible.

2.5.2 Off-Body Grid

The off-body grid (see Figs. 2.8 and 2.9) consisted of a Cartesian-type mesh spanning the entire domain and including five individual wake planes that the solution was interpo-

lated onto, corresponding to the wake ages where measurements were taken. The mesh was initially refined in the region encompassing the entire rotation plane and near-wake. Additional, extensive refinement was performed in the region behind the blade tip. This adaption of the off-body grid brought down the grid spacing from a minimum uniform spacing of $0.05c$ throughout the near-wake to $0.00625c$ spacing behind the blade tip in the region around the tip vortex. This brick-type refinement resulted in the computational grid containing 83.5M points overall.

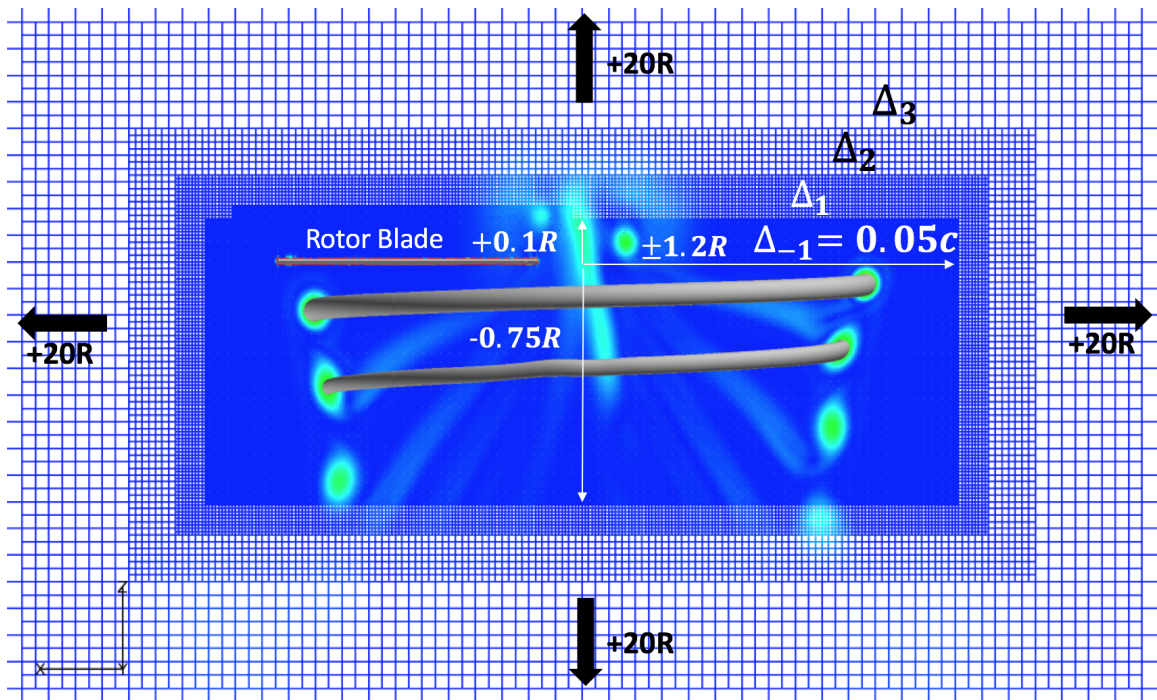


Figure 2.8 Cross section of off-body grid colored by vorticity magnitude and plotted with a Q-criterion iso-contour to show extent of wake.

The objective of the grid refinement was to provide sufficient resolution for the tip vortex, primarily at the locations where experimental measurements are available. The

computed solution, superimposed on the mesh in Fig. 2.8, shows that at least two helical steps of the vortex were able to be well resolved.

The solution was compared to the measurements at various wake stations from the trailing edge of the blade tip to 15° of wake age. The planes were positioned at wake ages of $\zeta = 2^\circ, 4^\circ, 7^\circ, 10^\circ,$ and 15° to allow for direct comparison with the available measured results. The planes (see Fig. 2.9) were initially created to extend two chord lengths in each dimension, with 200 cells, and later refined to a square of one chord length, resulting in a uniform spacing of 0.2225 mm, which was just slightly smaller than the resolution of the PIV measurements. Each wake plane was also extruded one cell in the normal direction to simplify the interpolation of the out-of-plane stress and strain component. Computed solutions from these planes were written periodically to small solution files that consumed significantly less space than the “q.save” solution file for the entire flow field (e.g., 20 MB as opposed to 15+ GB) using the &SPLITM namelist.

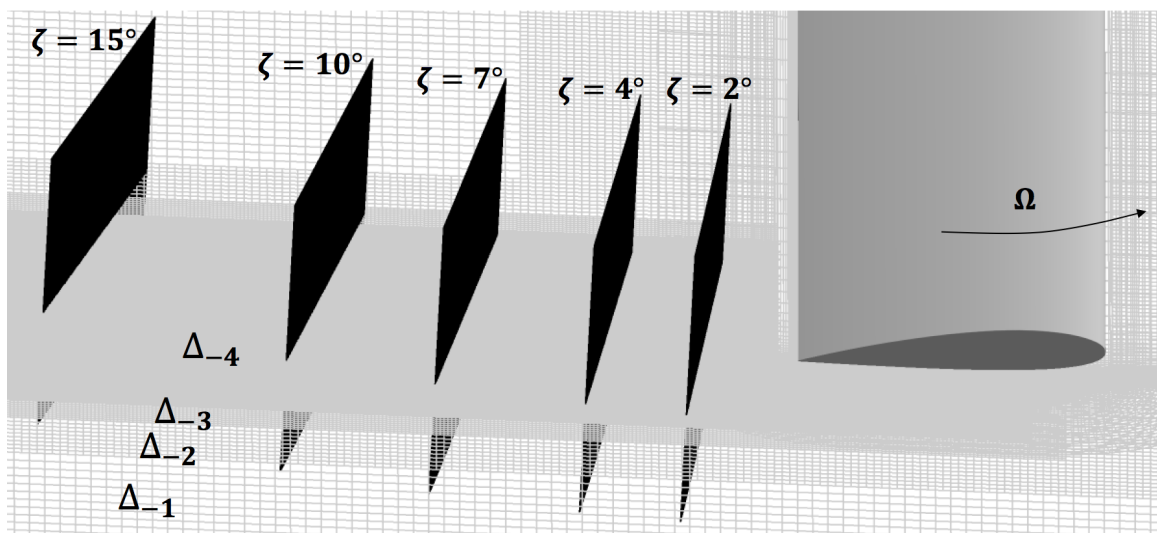


Figure 2.9 Grid refinement region behind blade tip containing five wake planes.

Currently, even the most advanced modern simulations cannot obtain a fully grid-independent solution of a rotor in hover. While integrated quantities such as thrust, power, and figure of merit eventually converge on a value, state-of-the-art rotor simulations have only been able to bring the core size down from 7 times greater than experimental measurement in recent years to 30% greater within the past year [Ref. 18]. Obtaining the latter has required a grid in excess of 500 million cells. Grid size is, therefore, a necessary compromise between computational limitations and the desired level of accuracy for the solution.

An initial investigation of the vortex roll-up quickly demonstrated the need for a more involved study in this region. It immediately became clear that each time the grid was refined, the vortex became tighter and more concentrated. However, a compromise needed to be made between refining the near-wake behind the rotor tip and resolving the entire flow field for a significant distance below the rotor plane. The sharp flow gradients throughout the rotor wake made a fully grid independent solution unobtainable, but one was needed to allow for enough resolution to accurately model the tip vortex.

This challenge was overcome by refining a small region behind the trailing edge of the blade tip, to just over $\zeta = 15^\circ$ down to $0.00625c$ spacing, and by increasing the numerical accuracy by switching from a 4th-order central differencing to 6th-order for the second portion of the grid independence study. The refined case of $0.00625c$ chord spacing corresponded to roughly 7 points within the experimentally measured vortex core. While non-ideal, this provided fine enough resolution to adequately model the velocity profile within the vortex.

Adaptive mesh refinement (AMR) was also considered to more efficiently resolve the wake. Initially, several cases were run with AMR to assess whether it was the best option for capturing the tip vortex (see Figs. 2.10 and 2.11). It was determined, however, that use of AMR would potentially compromise a major focus of this thesis, which is the parametric evaluation of turbulence models and their respective rotation corrections. To provide a fair comparison of these models, the same grid needs to be used for each case.

Because AMR conditionally refines the grid in regions of higher vorticity magnitude, changing the simulation settings such as turbulence model would also likely influence the grid. This approach would introduce an additional variable to the parametric study by causing both the grid and turbulence model to have an interdependent effect on the solution.

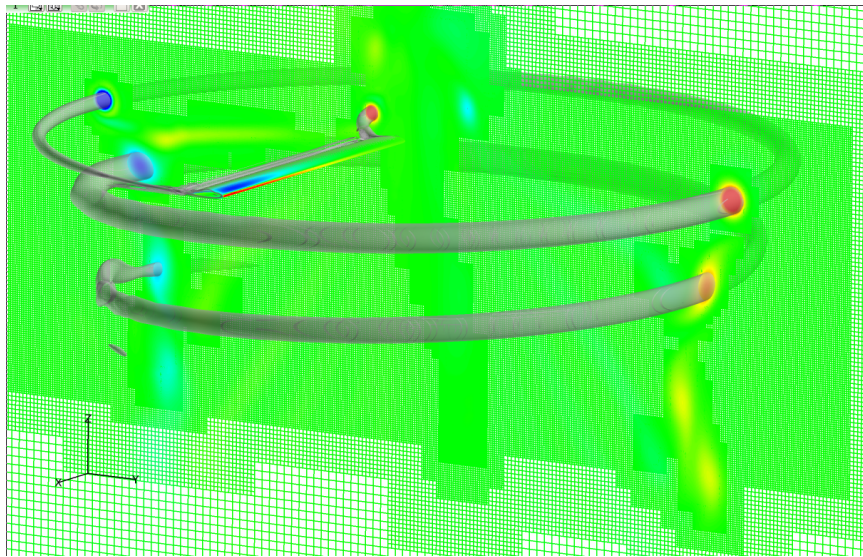


Figure 2.10 Initial considerations of AMR colored by vorticity along the x -axis.

Another tradeoff with AMR is that the grids need to be split fairly often to preserve the development of the helical vortex filament throughout the wake, and this approach takes

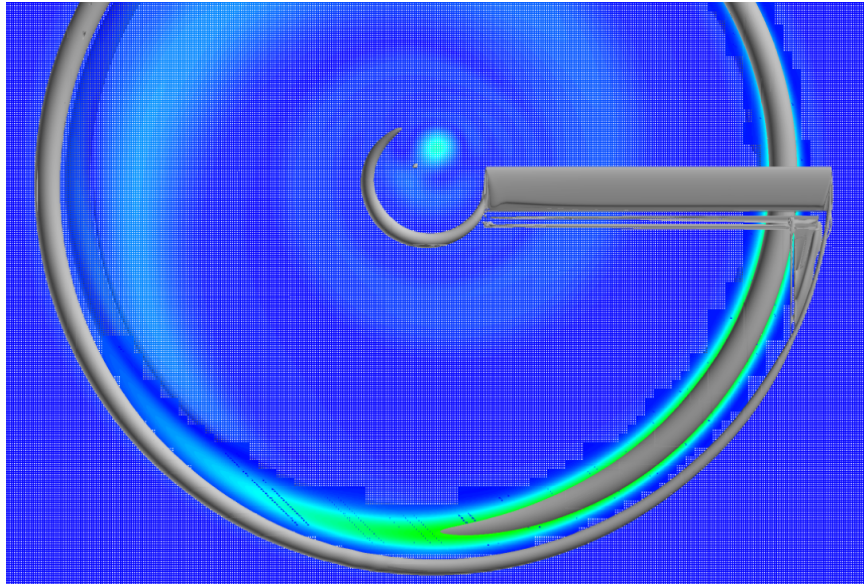


Figure 2.11 Top view of wake modeled using AMR and colored by vorticity magnitude.

additional time in the calculations. Because a very fine spacing was only required in the area containing the wake planes, using AMR only improved the grid spacing beyond this region, increasing the total number of grid cells overall. Therefore, AMR was deemed impractical for this parametric study, but is highly encouraged for limiting the cell size for the full extent of the tip vortex in most hover simulations.

2.5.3 Grid Connectivity

The spacing between the blade and off-body grid is defined in OVERFLOW using the “X-Ray” hole cutting approach introduced by Meakin [Ref. 51]. The position where the off-body grid was cut, relative to the blade geometry, had a significant influence on the near-body and off-body grid connectivity. This parameter, chosen to be 7.5% of the blade chord, required a compromise between the scale of the cells in the refined and unrefined

off-body regions. The spacing was primarily chosen to improve the spacing agreement in the transition to the refined region near the blade tip, which was the primary area of concern regarding the roll-up of the tip vortex. A front view of the blade is shown in Fig. 2.12 to illustrate the overlap between the cap grid and the refinement region. It must be noted that the procedure described above involves an iterative process of trial and error, and, in the absence of objective quantitative criteria, the final results must be visually inspected often.

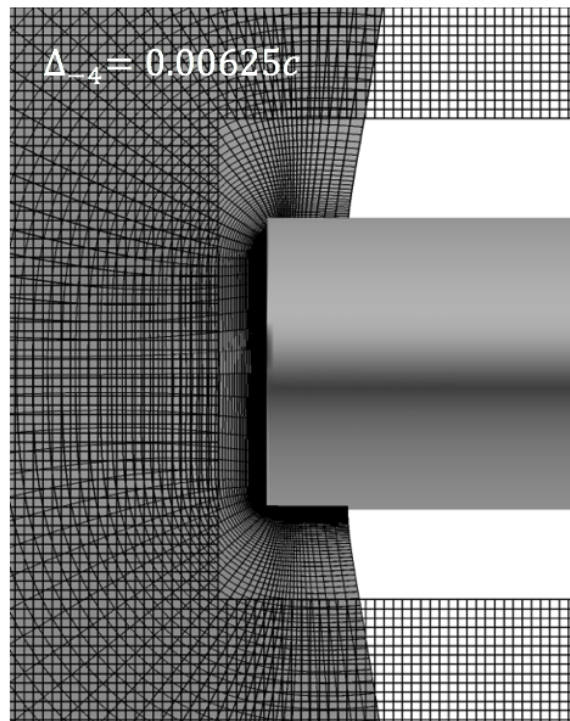


Figure 2.12 Front view of grid overlap at blade tip.

The trailing edge of the blade was also of critical importance because it is the region where the wake and the tip vortex first form. It was explained previously that the region of the near-body grid was designed to connect very well to the wake plane refinement region, which utilized the minimum off-body cell size.

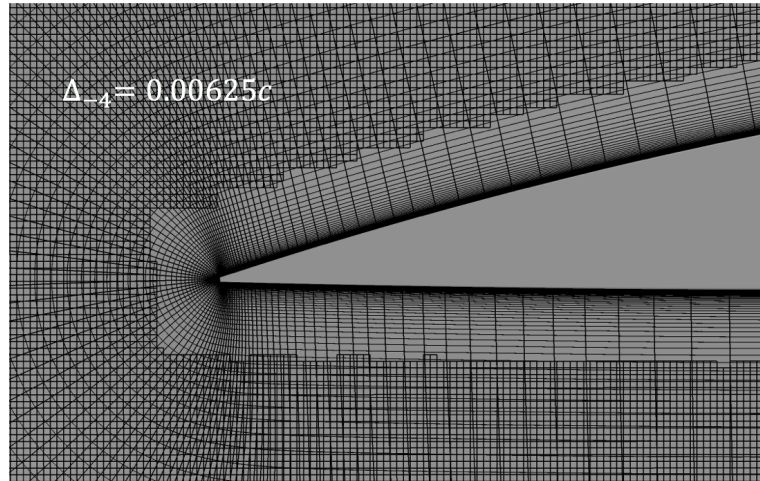


Figure 2.13 Overlap with refined OB-grid ($\Delta = 0.00625c$) at blade trailing edge.

By using such fine near-body spacing in the overlap region, the connectivity with the unrefined off-body grid region was less consistent along the surface of the blade. Along the upper and lower surfaces of the blade, the chordwise and spanwise spacing was significantly increased to match the off-body grid spacing, but the high density of nodes in the blade normal direction caused an inefficient transition to the off-body grid outside of the refinement region; this is shown in Fig. 2.14.

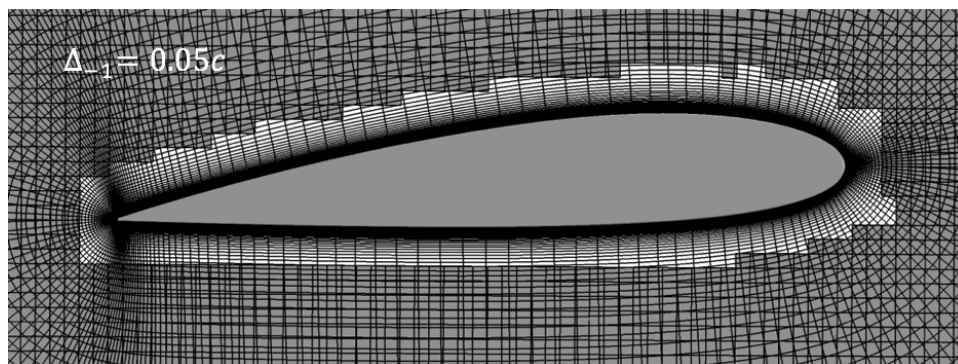


Figure 2.14 Overlap with unrefined OB-grid ($\Delta = 0.05c$) along blade surface.

Overall, the critical region of vortex roll-up behind the trailing edge of the blade tip was well preserved, and the inboard region along the blade span lost detail in the interpolation to the off-body grid, but had little effect on the overall solution. Significant time was devoted to grid generation because as it became clear from the grid independence studies, the grid size plays a more significant role in limiting the persistence of the tip vortex intensity than the turbulence model. By minimizing the grid dependence of the solution as much as possible before conducting the full study of the wake, the effect of turbulence modeling parameters on the solution could now be better understood.

2.5.4 Boundary Conditions

All six far-field walls were prescribed with free stream boundary conditions using 1-dimensional characteristic inflow/outflow relations. Depending on the velocity component normal to the grid boundary, this condition either extrapolates from the computational domain to the boundary or vice versa. The conserved quantities are based on the Riemann invariants of the Navier-Stokes equations. It is recommended as a general far-field boundary condition because of its general applicability.

The grid around the blade surface consisted of one solid wall non-slip boundary condition and one periodic condition where the grid reconnected with itself at the trailing edge. The cap grids also each had one solid wall boundary condition.

2.6 Setup for Comparative Analysis

With the grid and numerical scheme established, initial investigations of the isolated rotor simulation could now be conducted. Several iterations were run for various durations to gain an insight to the effect of certain simulation parameters. Two major decisions were made through this process of trial and error: the first being to maintain the same near-body turbulence model settings, limiting the parametric study to the variation of the aforementioned turbulence model and rotational correction terms in the off-body grids, and the second being to apply a uniform inflow velocity throughout the first six revolutions of the rotor simulation such that started the wake was initialized through a climb condition.

The first set of studies applied various turbulence models to the near-body grids in a baseline comparison, while treating the off-body grids as inviscid. This analysis concluded that the near-body turbulence models had little effect on the initial roll-up of the vortex compared to the differences observed between the various turbulence models over the first 15° of wake age. Therefore, the scope of the parametric analysis was limited to the effect of turbulence modeling in the off-body grid. Also, it showed that the transitional models could be excluded from the comparison because they introduced little effect in the prediction of the turbulent flow after separation.

The second set of studies dealt with the starting condition of the blade. Modeling a single-bladed rotor is in many ways more complicated than a conventional multi-bladed rotor, the most significant difference being the time required for the wake to fully develop. Various methods of efficiently starting the rotor were considered, while ensuring that the

efficacy of the modeling was maintained. These methods included impulsively starting the rotor with no external free-stream velocity, accelerating the rotor in an inertial reference frame (as the non-inertial reference frame cannot be continuously accelerated), and impulsively starting the rotor with a uniform free-stream inflow velocity correlating to a climb condition, which was later turned off. The final method was chosen as it allowed for the wake to fully develop within roughly five rotor revolutions. The inflow velocity was turned off after six revolutions, and the turbulence models were parametrically applied after nine revolutions. This starting condition ensured that a physically representative model of the rotor wake was being used for all cases.

2.6.1 Baseline Comparisons

The transition and rotation corrections were initially compared at the first wake plane to observe whether the formation of the tip vortex was significantly influenced by any of the models under consideration. Because a full comparison including the two transition models is beyond the scope of this study, such a comparison primarily served to ensure that the flow could be well modeled without specifying a transition region along the blade surface or by using a higher equation transition model.

The baseline analysis concluded that there was little variation in the immediate roll-up of the vortex at $\zeta = 2^\circ$ between the different turbulence models and their correction terms. This preliminary study addressed concerns of transitional flow over the rotor blade being improperly predicted as fully turbulent, and also served to provide a reasonable model for the laminar off-body case.

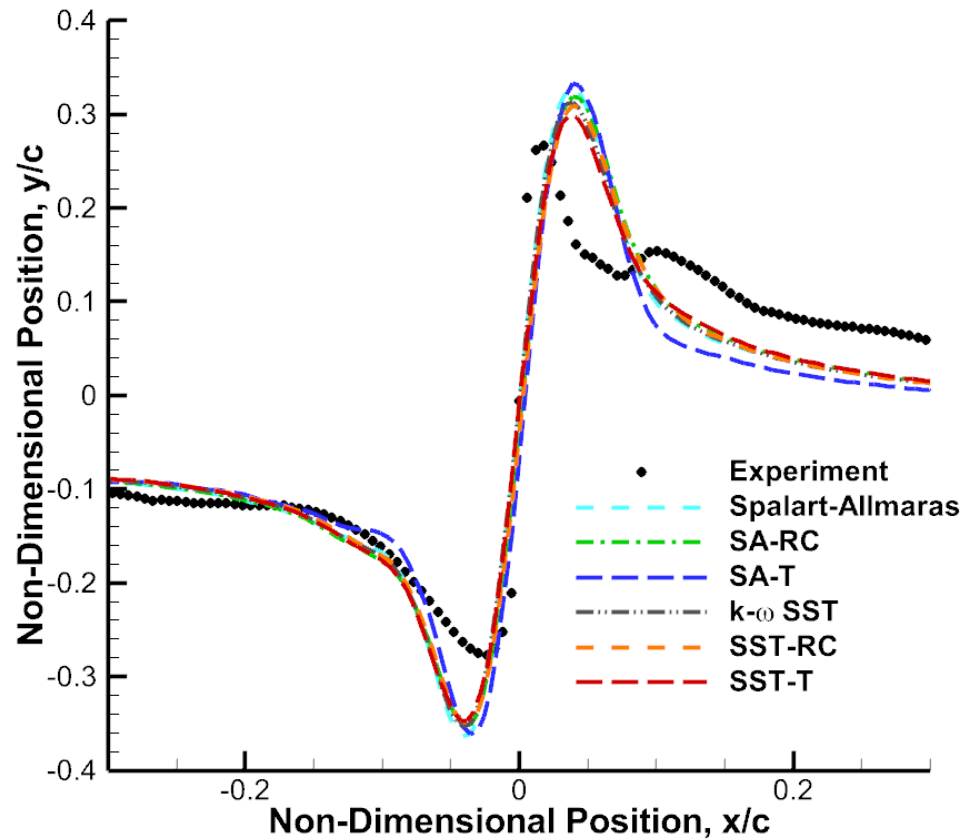


Figure 2.15 Baseline comparison incorporating two transitional models for the immediate roll-up at $\zeta = 2^\circ$.

The work in Ref. 45 had originally shown considered transition to turbulence on the blade surface as it relates to the formative stages of the tip vortex. Dacles-Mariani et al. originally prescribed a trip line in their highly resolved simulation of a wing tip alone, but concluded that removing the trip line and treating the flow as fully turbulent had no noticeable difference. This conclusion resulted from a study on a different experimental set-up, but suggested that off-body turbulence modeling had a greater effect on the tip vortex than accurately capturing the boundary layer transition.

The purpose of this baseline study was also to limit the scope of the study to the comparison of turbulence models applied to the off-body grid. The application of turbulence models for wall-bounded flows is generally understood and not the focus of the present research. The nature of these turbulence in fully separated flows, especially in the core of a vortex, is a far more pressing and relevant problem.

The baseline analysis concluded that the two transition models could be excluded from the study because they provided little change to the results. Also, the overall effects of the turbulence model used in the near-body grid was found to be relatively small, compared to the effect of the various turbulence models and corrections applied to the off-body grid. Therefore, in each case, the Spalart-Shur rotational/curvature correction was used in the near-body grid, to ensure consistency among the various cases, and only the off-body turbulence model was adjusted.

2.6.2 Starting Condition

Interestingly enough, simulating the flow field produced by a single-bladed rotor is in many ways more complicated than a conventional multi-bladed rotor, the most significant difference being the computational time required for the wake to fully develop. This section examines initial setbacks in modeling the rotor from an impulsive start, and discusses the methods considered for handling the starting condition. It was concluded that in dealing with an impulsive start condition, an inflow climb velocity can be applied to the first few revolutions to mitigate early vortex interactions and provide a more physical and steady-state solution of the vortex wake.

Physically, a rotor wake takes time to develop, which means that the rotor must undergo several revolutions before the flow reaches a relatively steady, periodic form suitable for analysis. The flow field measurements were made only after running the rotor at full speed for several minutes, which can often mean thousands of revolutions. Modeling the rotor for this many revolutions is, of course, infeasible by computational means, leading to the challenge of obtaining a time-accurate solution of a fully formed tip vortex.

Therefore, the rotor must undergo several revolutions before the flow reaches a time periodic response that is suitable for analysis and comparison with the measured results. In the experiments, measurements were taken only after running the rotor at full speed for several minutes, corresponding to several thousands of revolutions. Modeling the rotor for this many revolutions is, of course, infeasible by computational means, leading to the challenge of obtaining a time-accurate solution of a fully developed rotor wake and the tip vortex.

During the first several attempts at running the single-bladed rotor simulation, it became apparent that the helical form of the vortex wake would indeed take a very long time to develop. One issue that inhibited the proper development of the wake was a powerful, toroidal vortex created by the overlapping of the first two passes of the tip vortex; this effect is visualized in Fig. 2.16 using an iso-surface of the Q-criterion.

As the rotor blade completed its second pass, the initial tip vortex could be seen entangling with itself and forming a toroidal vortex ring with a net strength higher than that of a single filament from the blade tip. This behavior persisted through the rotor wake, remain-

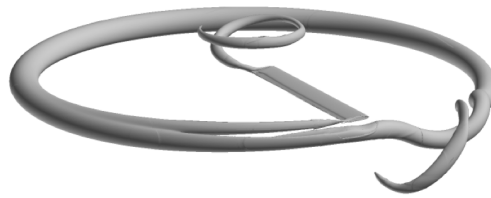
2 Revolutions

Figure 2.16 Flow field after 2 rotor revolutions from impulsive start.

ing in the same spatial location as the non-inertial reference frame rotated in the clockwise direction after 6.5 revolutions (see Fig. 2.17).

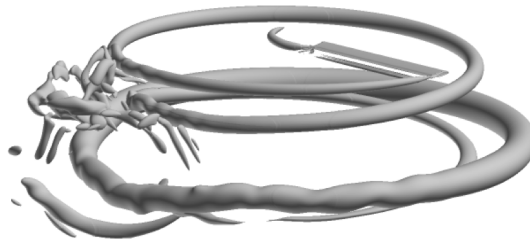
6.5 Revolutions

Figure 2.17 Flow field after 6.5 rotor revolutions from impulsive start.

Even after 11.25 revolutions the behavior continued, as shown by Fig. 2.18, although the majority of the vortex wake had developed its characteristic helical form.

Two revolutions later, at 13.25 revolutions, the tip vortex can be seen persisting through the vortex wake at least five turns in Fig. 2.19. However, the original instability remained, having a substantial influence on the entire wake.

Although the effect of this flow feature on the first few turns of the helical wake would be expected to eventually diffuse over time, it continued to affect the wake, even in the

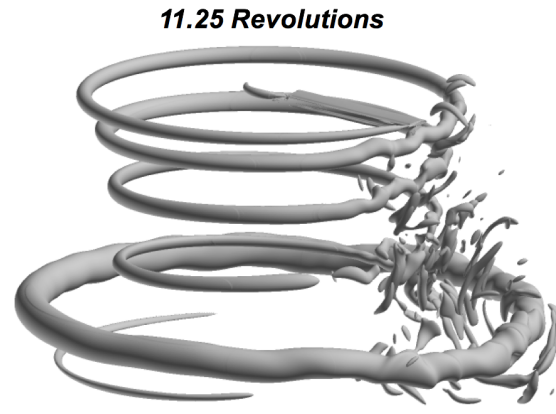


Figure 2.18 Flow field after 11.25 rotor revolutions from impulsive start.

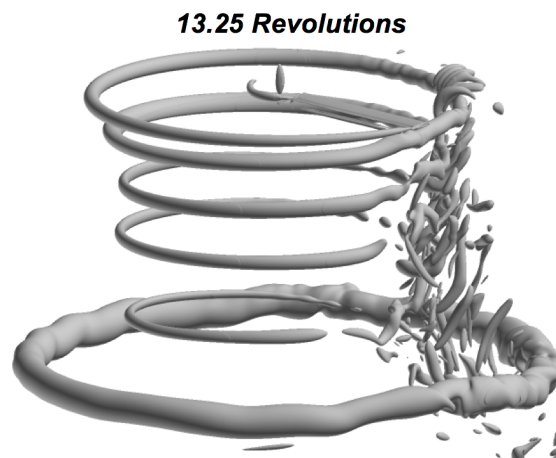


Figure 2.19 Flow field after 13.25 rotor revolutions from impulsive start.

rotational plane of the blade, after 20 revolutions. The residual effect of the starting vortex can still be clearly seen throughout the wake in Fig. 2.20.

The process by which the starting vortex persisted throughout the wake of the rotor blade, affecting each pass of the tip vortex even up to 20 revolutions, was very interesting and unexpected. While further investigation of this behavior is required, it is beyond the scope of this thesis. Rather, this research begins by determining a method to mitigate the

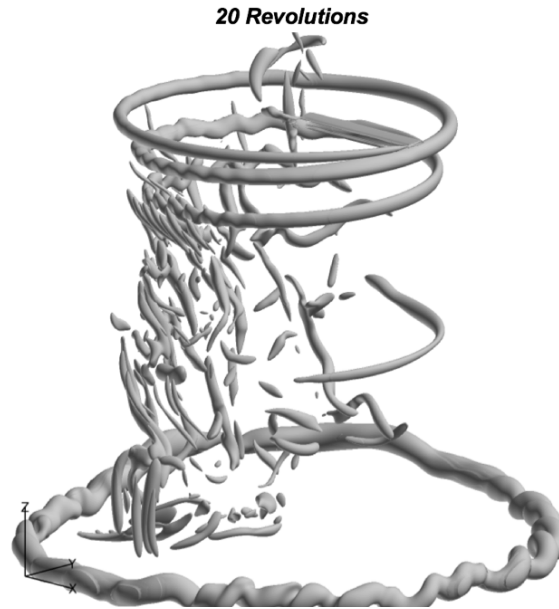


Figure 2.20 Flow field after 20 rotor revolutions from impulsive start.

effect of the starting condition on the hover solution to obtain results for comparison to the experimental data.

The reasoning that this can be done without compromising the efficacy of the model is because the starting behavior of a rotor is generally understood as being a complex phenomena. The rapid start of a rotor was shown by Taylor [Ref. 52] using a balsa dust technique to seed the flow field, which clearly captures the toroidal vortex ring shed from a starting rotor.

Carpenter and Friedovich [Ref. 53] studied the same phenomena by rapidly increasing the pitch of a rotor blade (at roughly 200°s^{-1}) after 0.064 seconds or about 7 revolutions. The results of these two studies, shown in Figs. 2.21 and 2.22, respectively, can be compared to the computational solution of the single-bladed rotor after 6.5 revolutions. This

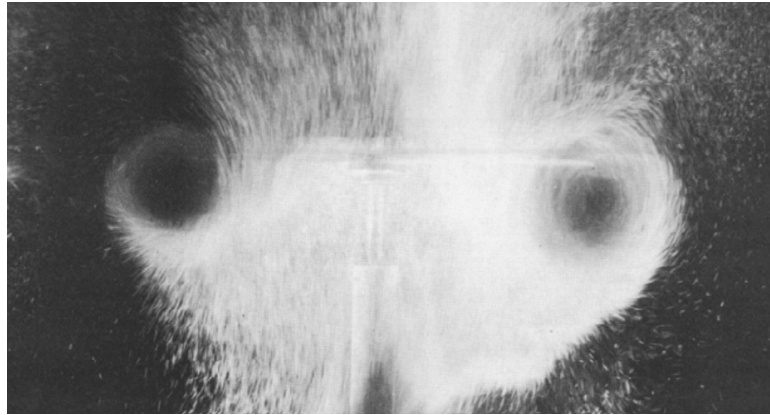


Figure 2.21 Balsa dust flow visualization of an impulsively started rotor.

shows that the computational predictions are not necessarily inaccurate, but are predicting a very complex transient process of the physical wake development.

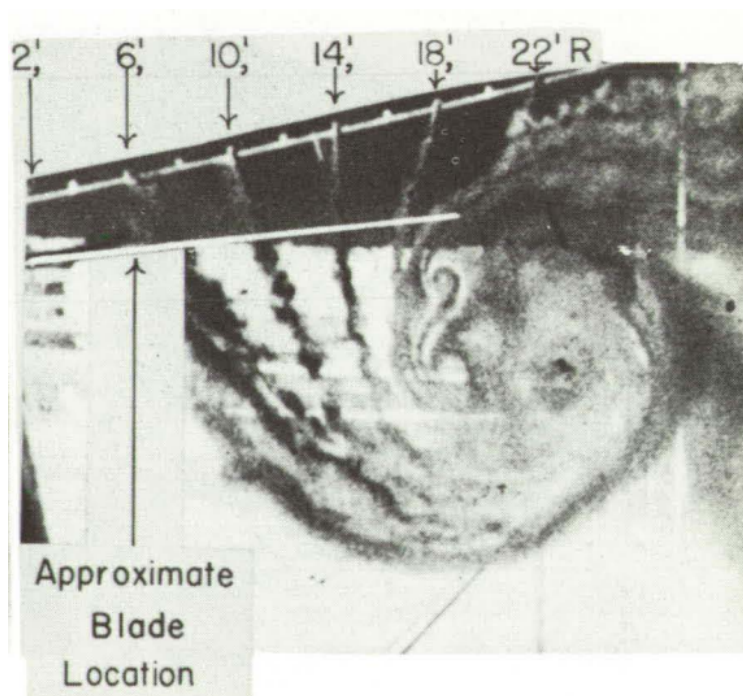


Figure 2.22 Smoke flow visualization of a rotor wake, approximately 7 revolutions after undergoing a rapid increase in blade pitch.

One method of handling the starting condition was to discretely increment the rotors rotational speed at specified time steps. The only way this would be feasible is if the speed were increased at most every 45° or 90°, each time requiring the OVERFLOW solver to reinitialize and redistribute the load for parallel processing. Even then, the discrete increases in rotational velocity would be large enough to disturb the flow field, rendering the solution unsuitable.

Another option for gradually increasing the rotational speed was to switch from a non-inertial to an inertial reference frame. Gradual acceleration of the rotor blade up to its rotational speed of 35 Hz could then be applied using the grid motion input file, such that the wake planes and near-body grids changed position relative to the Cartesian-type, off-body mesh each time step. While this method was found to improve the formation of the tip vortex, it was quickly abandoned because grid adaptation was required to continuously refine the near-wake region around the wake planes.

The next logical step in obtaining a model of the wake was to apply a uniform inflow climb velocity throughout the flow field to convect the start-up and tip vortex from the first revolution below the rotor plane. To mimic the inflow velocity that would be seen by the rotor in hover, the uniform inflow velocity ratio, λ_h from simple momentum theory was calculated by the following expression.

$$\lambda_i = \lambda_h = \sqrt{\frac{C_T}{2}} \quad (2.61)$$

The solidity of the single blade was defined as the ratio of the single, rectangular rotor blade to the area of the disk plane (i.e., $\sigma = \frac{N_b c}{\pi R}$ with $N_b = 1$). Using this equation, and the definition of C_T/σ given by the documentation from the experiment, the thrust coefficient was found to be $C_T = 0.002233$; this value was also confirmed by a simple analysis of the rotor blade using blade element momentum theory.

The inflow velocity ratio was then calculated from the thrust coefficient and multiplied by the tip speed to obtain an estimation of a relatively small dimensional inflow velocity of 2.974 ms^{-1} in hover. This value corresponded to an inflow/free-stream Mach number of $M_i = 0.008687$ compared to the tip/reference Mach number of $M_{\text{tip}} = 0.26$, which were each directly input as flow parameters. This value of uniform inflow was applied to the first six revolutions of the simulation.

Leaving this inflow condition on for six revolutions led to the rotor being in climb condition for the first half of the simulation. However, removing the inflow velocity after the helical form of the tip vortex had fully developed only resulted in a reduction to the helical pitch of the wake, and the wake geometry quickly converged on a solution that was equivalent to the hover condition.

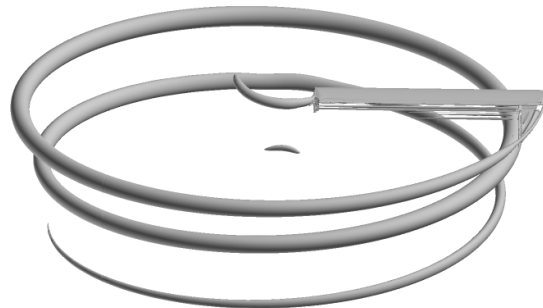


Figure 2.23 Flow field after 10 revolutions using inflow start condition.

The SA and $k-\omega$ SST turbulence models with the Spalart-Shur rotational/curvature correction (described in the Turbulence Modeling Section) were used to develop the solution to 9 revolutions (6 with inflow, 3 without), to provide a fully developed condition for the various other cases to be run from. Each case was then run for an additional 5 revolutions with the specified model, for a total of 14 revolutions overall. Figure 2.23 shows the fully developed inviscid off-body case from an inflow starting condition. With the grid and simulation parameters fully established, the solution could now be obtained for the selected turbulence models and corrections.

3. Results

The results of the present study assess the flow field characteristics pertaining to the formation and convection of the tip vortex throughout the rotor wake, with emphasis on the first 15° of wake age. This analysis is categorized into a comparison of velocity profiles across the vortex, 2-dimensional vorticity distributions at each of the wake planes, core properties such as core size and peak swirl velocity, persistence, and finally turbulence properties. Emphasis was placed on comparing the SA and $k - \omega$ SST models, with and without the available correction terms in OVERFLOW, against measurements from Ramasamy et al. [Ref. 1], while the influence of grid size and spatial numerical accuracy was also addressed.

3.1 Computational Cost

Before comparing the results from each simulation case, the differences in computational cost (i.e., wall clock time for a given number of cores) was compared between the various turbulence models. The inviscid case was used as a baseline for comparison, and the relative computational wall time is listed for each subsequent case as a ratio to the baseline case.

This comparison is provided before the flow field predictions made by these various cases are compared to experimental data because it is important to understand the applicability of each of these solutions. For example, the $k - \omega$ SST model and its associated

Table 3.1 Turbulence Modeling Computational Cost

Case	Correction Applied	Relative Wall Time
Inviscid	None	1
SA	None	1.13
SA-R	Dacles Mariani et al. RC Correction (IRC=2)	1.13
SA-RC	Spalart and Shur RC Correction (IRC=1)	1.31
SST-DES	Detached Eddy Simulation (IDES=2)	1.36
$k-\omega$ SST	None	1.91
SST-R	Dacles Mariani et al. RC Correction (IRC=2)	1.91
SST-RC	Spalart and Shur RC Correction (IRC=1)	2.22

[†]Wall clock times for 3,456, 2.7 GHz, Intel Xeon E5-2697v2 cores.

corrections may not be useful for rotor design purposes because it greatly increases the computational cost. However, DES may be a feasible option given the efficiency of the overset grid framework in OVERFLOW.

3.2 Velocity Profiles

The first level of analysis compared the velocity distribution on a 2-dimensional cut across the tip vortex between the experiment and the various simulations. Parameters such as swirl velocity, core size, vorticity magnitude, and circulation were derived to provide detailed comparisons between the predictions and the measurements, the objective being to compare the effects of each turbulence model and correction term in its ability to predict the mean flow behavior.

This analysis began with a focus on grid-independence, which was of course naturally linked to the chosen accuracy of the numerical scheme. An inviscid (Euler) solution of the off-body grid was used as the baseline case while the grid was progressively refined and

the order of accuracy for the spatial discretization was increased to better capture the tip vortex.

The numerical mesh had to accommodate a very broad range of length scales to efficiently capture the entire flow field with sufficient detail to adequately resolve and preserve the tip vortex core and the shear layers behind the blade. Furthermore, the off-body grid needed to capture the convection of the wake into the far field for several revolutions; capturing the wake to this extent required a compromise between the near-body and off-body grid size because a grid-independent solution of the entire wake was infeasible. Instead, the effect of the grid was analyzed in a small refinement region spanning the first 15° of wake age behind the trailing edge of the blade tip where results would be compared to the available PIV measurements, and the remainder of the off-body grid used a minimum spacing of 5% chord ($0.05c$).

The wake plane at $\zeta = 15^\circ$ was selected to examine the extent of the numerical dissipation from grid size on the solution throughout the refined wake region. The swirl velocity was the chosen parameter for this comparison, being defined by the vertical component of velocity along a horizontal cut through the vortex center. Velocity distributions obtained from inviscid solutions of the off-body mesh using a 4th-order centered stencil with a 4th-order dissipation scheme for different levels of refinement are compared with the measurements in Fig. 3.1.

The comparison in Fig. 3.1 shows that the peak swirl velocity did not reach the measured value until the off-body grid spacing was reduced to $0.00625c$. Even refining the grid

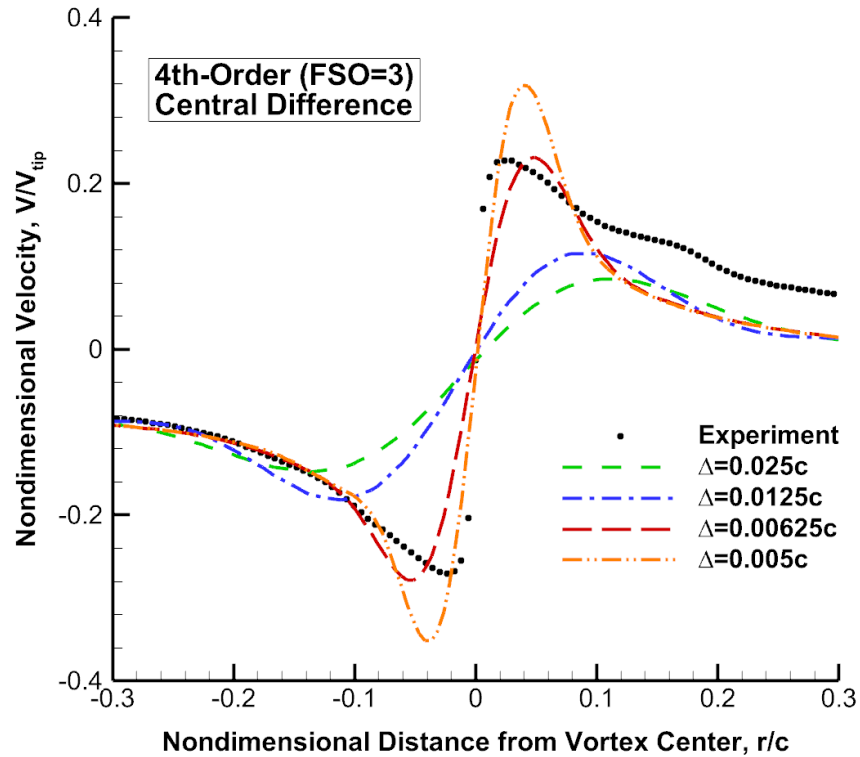


Figure 3.1 Effect of grid refinement for inviscid off-body solutions.

slightly more to $0.005c$ still had a small effect on the solution, but greatly increased the number of total grid points and thus the computational cost.

The grid independence of the solution in the near-wake was further analyzed by switching to a 6th-order centered stencil with 6th-order dissipation. Again, the grid resolution was varied from $0.025c$ to $0.005c$, and the velocity distribution in the vortex was compared to the measurements, as shown in Fig. 3.2. The refined mesh with $0.00625c$ spacing corresponded to roughly 7 points across the vortex core, and the most refined case provided 10 points within the core diameter. Even at this fine resolution, there was some sensitivity of the solution to grid size. However, the 6th-order central differencing scheme clearly im-

proved the accuracy of the solution and improved resolution of the flow gradients in the vortex.

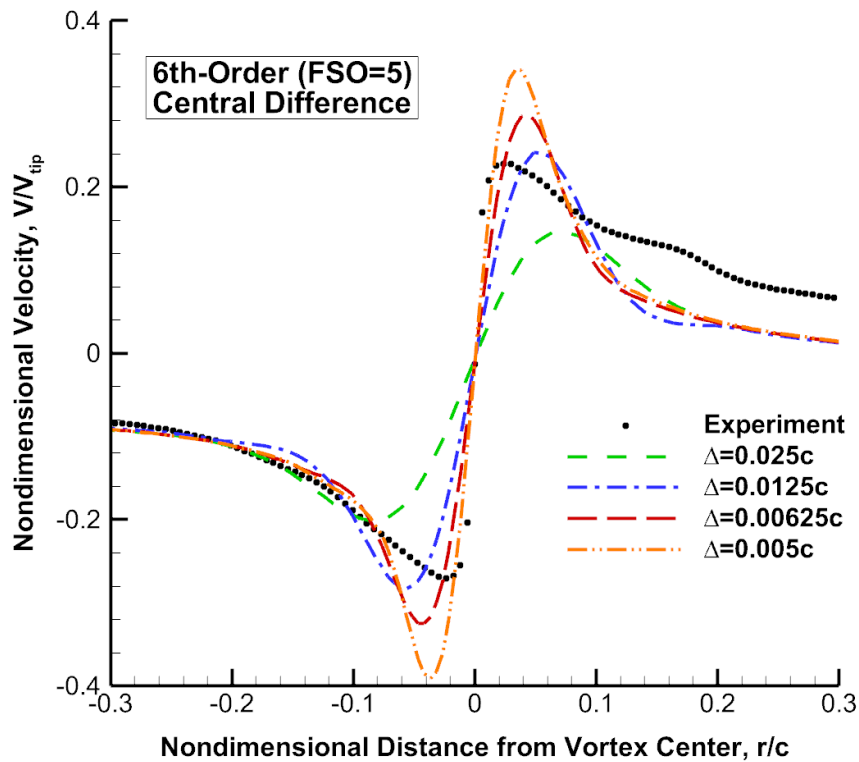


Figure 3.2 Effect of grid refinement for inviscid off-body solutions.

Therefore, the 6th-order central differencing scheme (FSO=5 in OVERFLOW) with $0.00625c$ spacing was deemed acceptable for the remainder of the study. Also, the computational cost of using this higher-order scheme was relatively small compared to the benefits it provided. Specifically, each time step using the FSO=5 scheme in OVERFLOW took approximately 10% longer than that of the 4th-order central differencing scheme (FSO=3), which concurs with the expected behavior described in Ref. 34. It is important to appreciate that the results provided in the grid independence study were not run until full convergence

of the wake was obtained. However, the fully converged solutions presented throughout the remainder of the results shown in this thesis were run for a full 14 rotor revolutions.

After the grid and numerical scheme had been selected, seven additional cases were considered with respect to the viscous treatment of the off-body flow field. First, the N-S equations for a laminar flow case were considered, without applying any type of turbulence model to the off-body grid. The remaining six cases employed various forms of the SA or the $k-\omega$ SST turbulence models, with and without the two available rotational correction terms. Notice that the Spalart-Shur rotational/curvature correction was applied in the near-body grids for each of the cases to capture boundary layer transition and early flow separation. As a result, the vortex was well preserved in the short distance from the blade trailing edge to the first measured wake plane at 2° , and the effects of the various models could be considered from an identical near-body solution, limiting the parametric study to the off-body grid.

The swirl velocity profiles for the inviscid baseline case, viscous, laminar case, and two turbulence models without corrections are shown in Fig. 3.3. It can be seen that the differences between the solutions with and without the turbulence models was very large, with each of the turbulence models clearly increasing the size of the vortex core and markedly reducing the swirl velocity. It is also important to note that both the inviscid and laminar solutions overpredicted the fluid velocity in the vortex. It appears, therefore, that the turbulent flow effects are important for certain regions in the vortex and cannot simply be neglected from the simulation. Rather, the effects of turbulence in the vortex must be modeled with

a better understanding of the turbulence distribution as previously shown by the flow field visualization of the vortex core in Fig. 1.3.

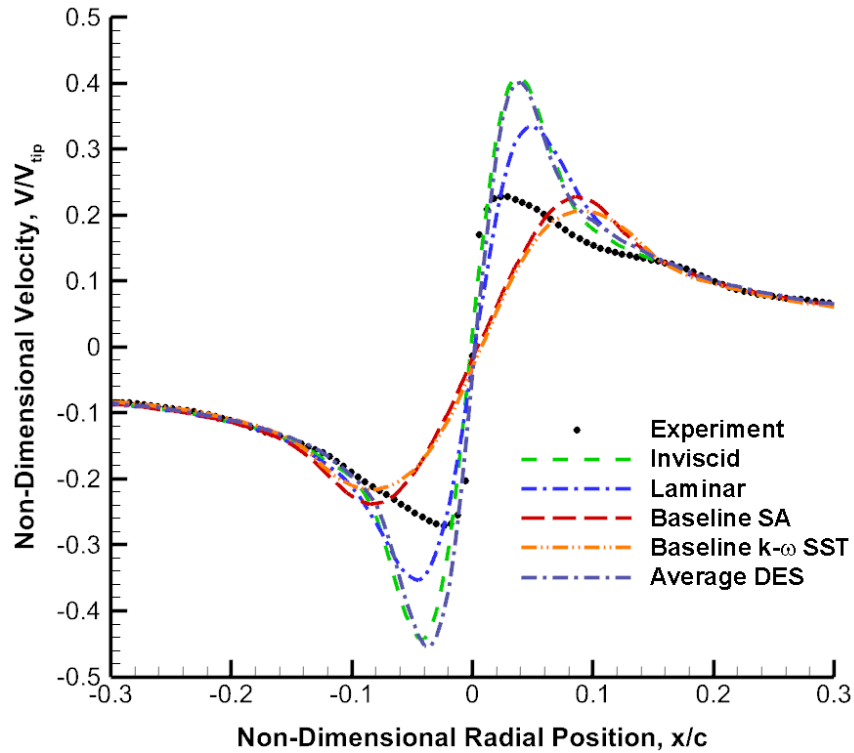


Figure 3.3 Swirl velocity at 15° of wake age for baseline (inviscid) case, laminar case, and standard turbulence models.

The differences between each of these cases and the measured velocity distribution demonstrated the need for corrected turbulence models, which are compared in Fig. 3.4. The velocity profiles predicted by using these corrected turbulence models better agreed with the PIV measurements. Using the Spalart-Shur correction applied to the SST model gave the best agreement with the peak swirl velocity and the same correction applied to the SA model give the best prediction of the core size.

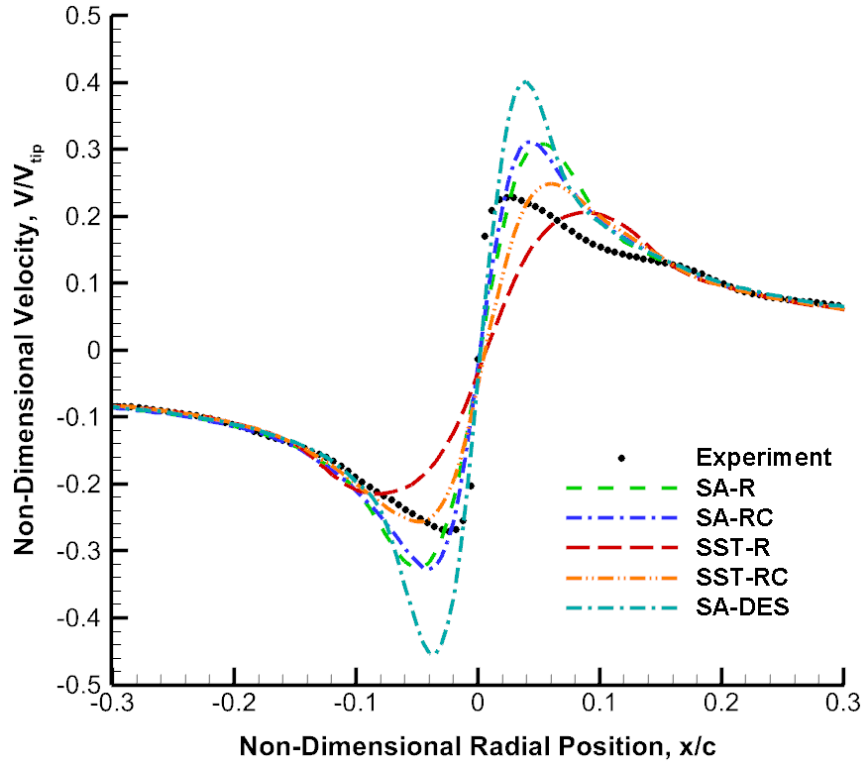


Figure 3.4 Swirl velocity at 15° of wake age.

The mean flowfield predictions using Detached Eddy Simulation (DES) were also included in this comparison. These results showed an overprediction of peak swirl velocity, which came very close to the predictions from the inviscid baseline case. The possible cause for this disagreement between the DES and the measurements is discussed later.

3.3 Core Properties

To better quantify behavior of the vortices in the formative stages, the core radius, r_c , was extracted from both the measurements and the CFD results over the first 15° of wake age. The process by which the core radius was determined was the same for both the

measurements and the computations, and was done by fitting a spline to the swirl velocity profile and locating the maximum value. Then the position of the maximum and minimum velocities was used to determine the core diameter, the half value being defined as the core radius (see Fig. 3.6). Similarly, the difference between the peak values of swirl velocity were determined for each case, half the difference in peak velocities giving the maximum swirl velocity (see Fig. 3.8).

The reason the peak swirl velocities are consistently overpredicted at the first wake age of $\zeta = 2^\circ$ is because the Spalart-Shur (RC) correction was applied to the near-body grid for each of the cases. This decision, described in the Section 2.6.1, allowed for the effects of each turbulence model case to be more easily distinguished by the trend in the flow field throughout the refinement region, while limiting the comparative analysis to turbulence modeling in the off-body grids (i.e., pure shear flow).

Quantifying the differences in the swirl velocity distribution showed exaggerated the differences between each of the cases, although, overall, good agreement was reached with the experiment. The comparisons of peak swirl velocity and core size further demonstrated that the application of the rotational corrections in each case reduced core size and increased swirl velocity. Each of the correction terms applied to the SA model seemed to overpredict the velocity in the core beyond a level that was indicated by the PIV measurements.

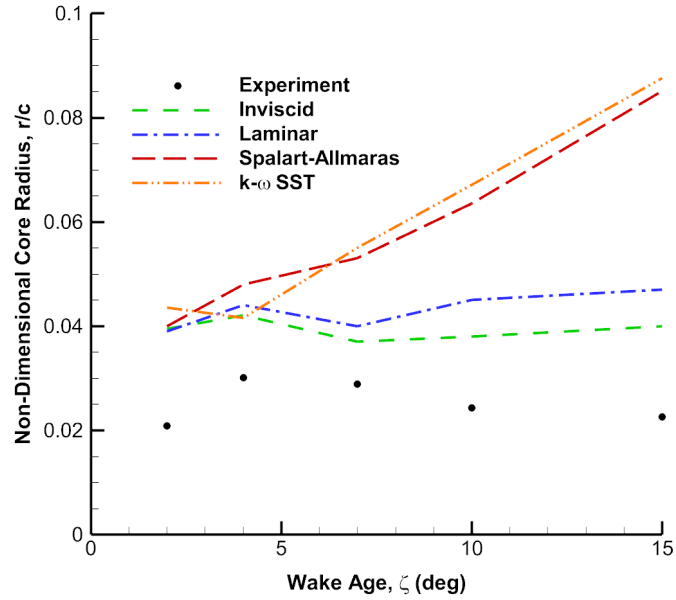


Figure 3.5 Core radius for baseline cases and standard turbulence models.

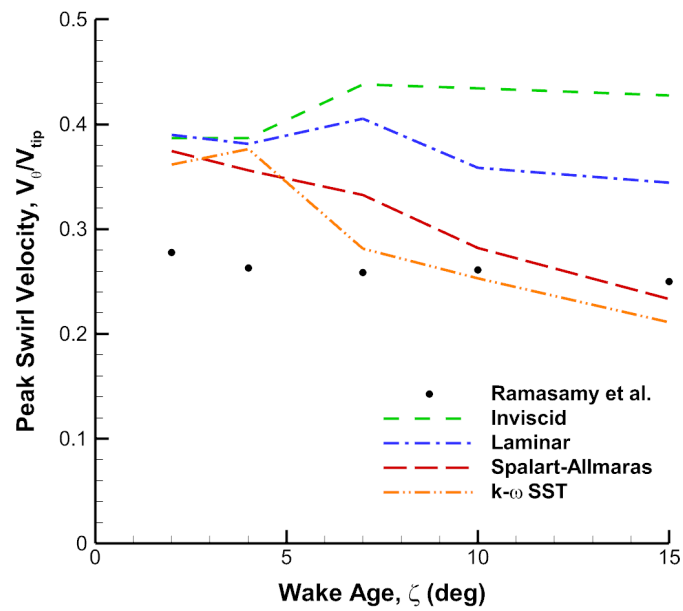


Figure 3.6 Peak swirl velocity for baseline cases and standard turbulence models.

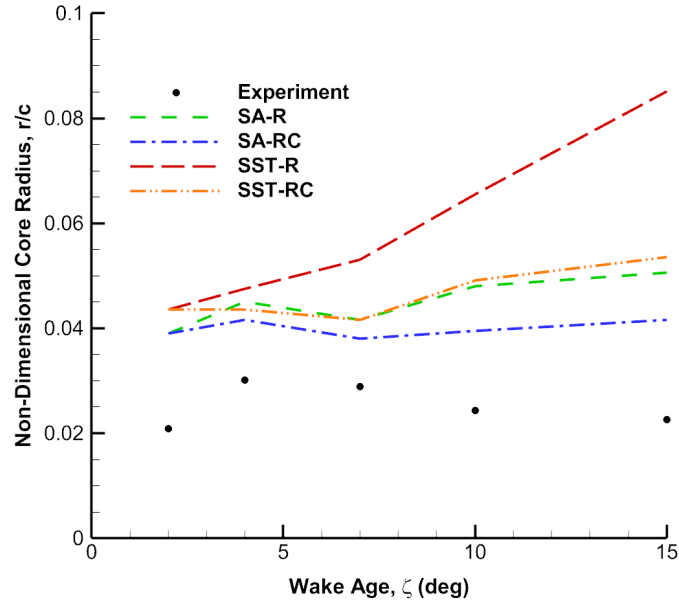


Figure 3.7 Core radius for various turbulence model corrections.

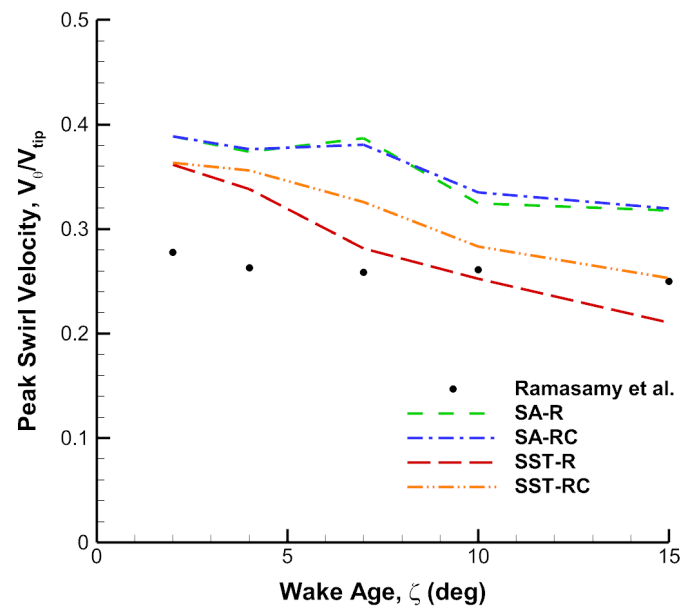


Figure 3.8 Peak swirl velocity for various turbulence model corrections.

3.4 Circulation

Despite differences in core radius and peak swirl velocity from the available measurements, the circulation, which was determined by numerical integration of the velocity around the vortex core, remained relatively constant with wake age and was accurately predicted by each of the cases, as shown in Fig. 3.9. The three computational solutions shown previously that gave disparate predictions of the swirl velocity distributions provided very close agreement to the overall circulation. This was an important finding, because it shows that the simulations predict and preserve the strength of the vortex well, regardless of the applied turbulence model.

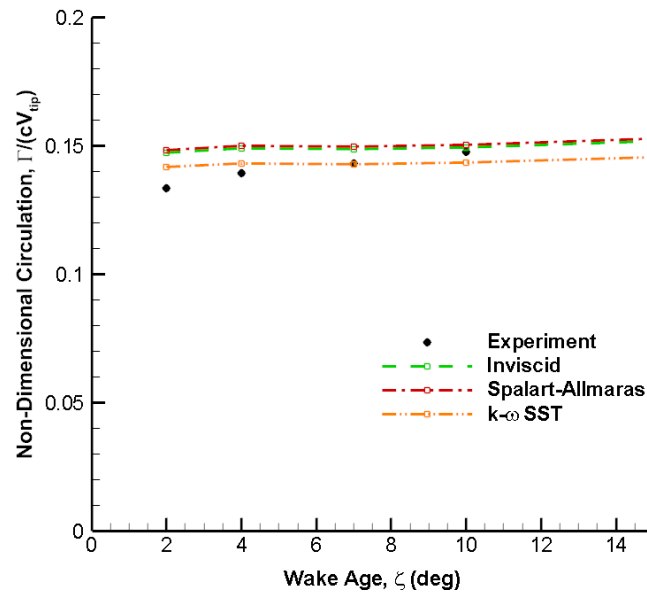


Figure 3.9 Circulation plotted throughout the refined region.

The circulation was calculated by numerically integrating around concentric closed paths along the vortex center, as described by Appendix C. The values from this integration are shown over a range of radial positions in Fig. 3.10. Despite the differences

in these values near the center of the vortex, the total vortex circulation is taken as the asymptotic value each of the curves approach, which are in good agreement.

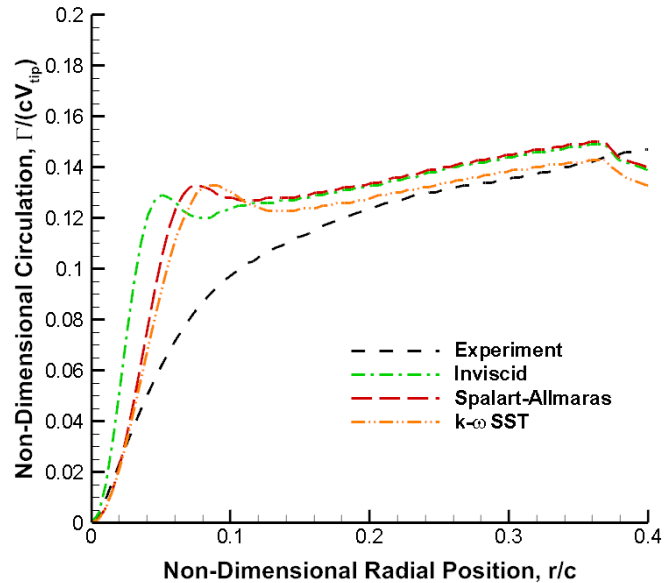


Figure 3.10 Circulation plotted throughout the refined region.

The variation in the values of circulation with respect to the radial distance from the vortex center were indicative of the rotational nature of the tip vortex. Each of the turbulence models predicted a more uniform value of circulation than the measurements as the closed loop of integration was taken closer to the center of the vortex. This outcome suggests that the viscous effects of turbulence in the tip vortex cause a greater reduction in swirl velocity than the simulations predict. However, the vorticity, indicative of the velocity gradients in the vortex core, remained very high in the measurements regardless of the reduction in peak swirl velocity.

3.5 Vorticity

Before comparing the 3-dimensional computational results to the 2-dimensional planar measurements, the velocities needed to be interpolated and projected onto the five individual wake planes at 2° , 4° , 7° , 10° , and 15° . The velocity fields were transformed into a local coordinate system at each of these planes to ensure that the measurements and computational results were being compared on an exactly equivalent basis.

Figure 3.11 shows the cross-section of the tip vortex at 15° of wake age in terms of vorticity contours from the experiment and for the baseline (inviscid) case. Similarly, Figs. 3.12 and 3.13 show the vorticity obtained using the various correction terms applied to the SA and $k - \omega$ SST models, respectively. For brevity, the 15° wake age case is used here to show the primary differences in the solutions, the earlier wake ages showing similar outcomes and so providing no additional insight to the effects of each variation to the RANS solutions. These types of presentations provide a more intuitive representation of the diffusion of vorticity caused by the modeling of turbulence.

As previously described, reducing the grid size so that the solution could be efficiently interpolated onto these planes was only possible after extensive grid refinement. Even still, the numerical dissipation resulted in the peak vorticity from the baseline, inviscid case ($|\omega|_c/V_{\text{tip}} = 19.3$) to fall short of the peak vorticity from the measurements, which reached a value of $|\omega|_c/V_{\text{tip}} = 63.6$ in the center of the vortex.

Each case in which a turbulence model was applied exhibited diffusion of the vorticity, while the rotational correction terms generally reduced this effect. Specifically, the SA-

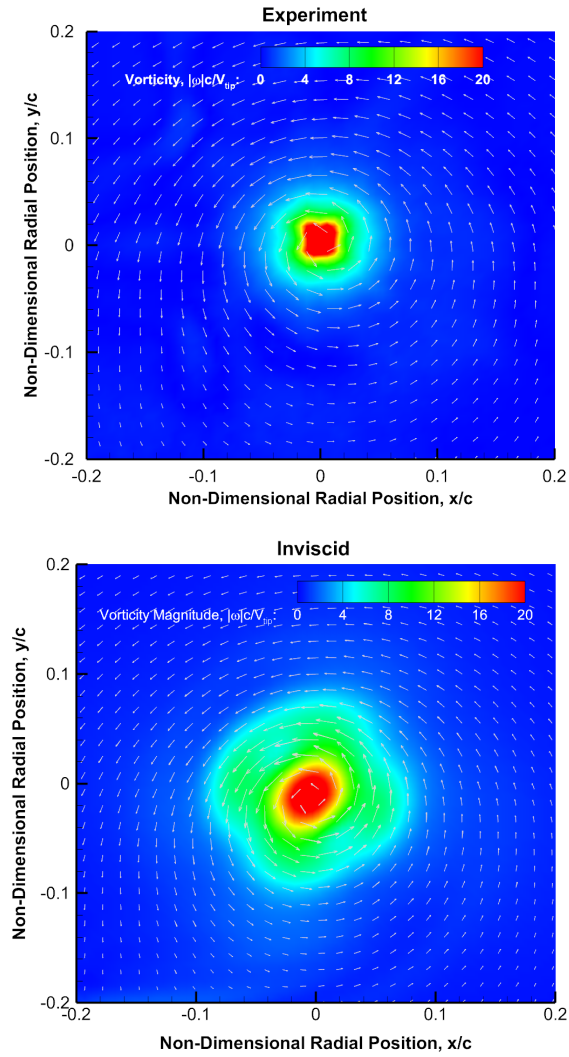


Figure 3.11 Baseline vorticity magnitude comparison at $\zeta = 15^\circ$

RC case (Spalart Allmaras model with the Spalart-Shur rotational/curvature correction) provided the least diffusion of vorticity, which turned out to have the best correlation to the measured behavior of the tip vortex.

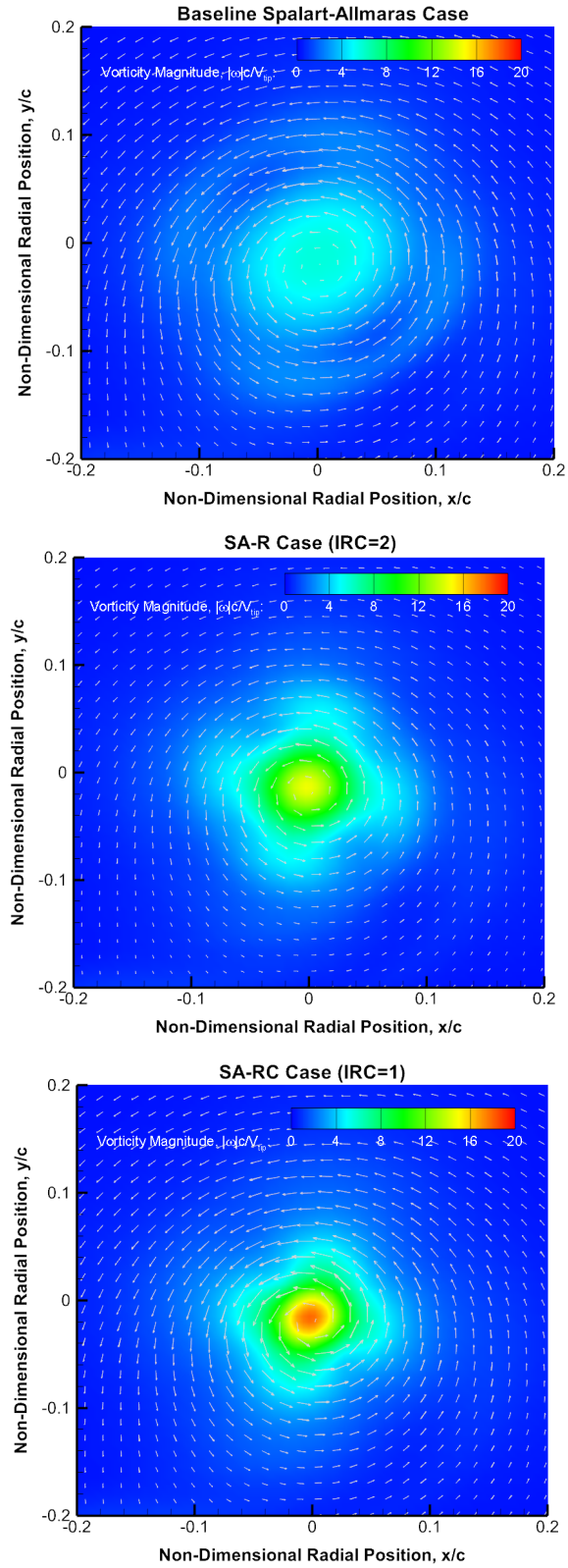


Figure 3.12 SA comparison of vorticity magnitude at $\zeta = 15^\circ$

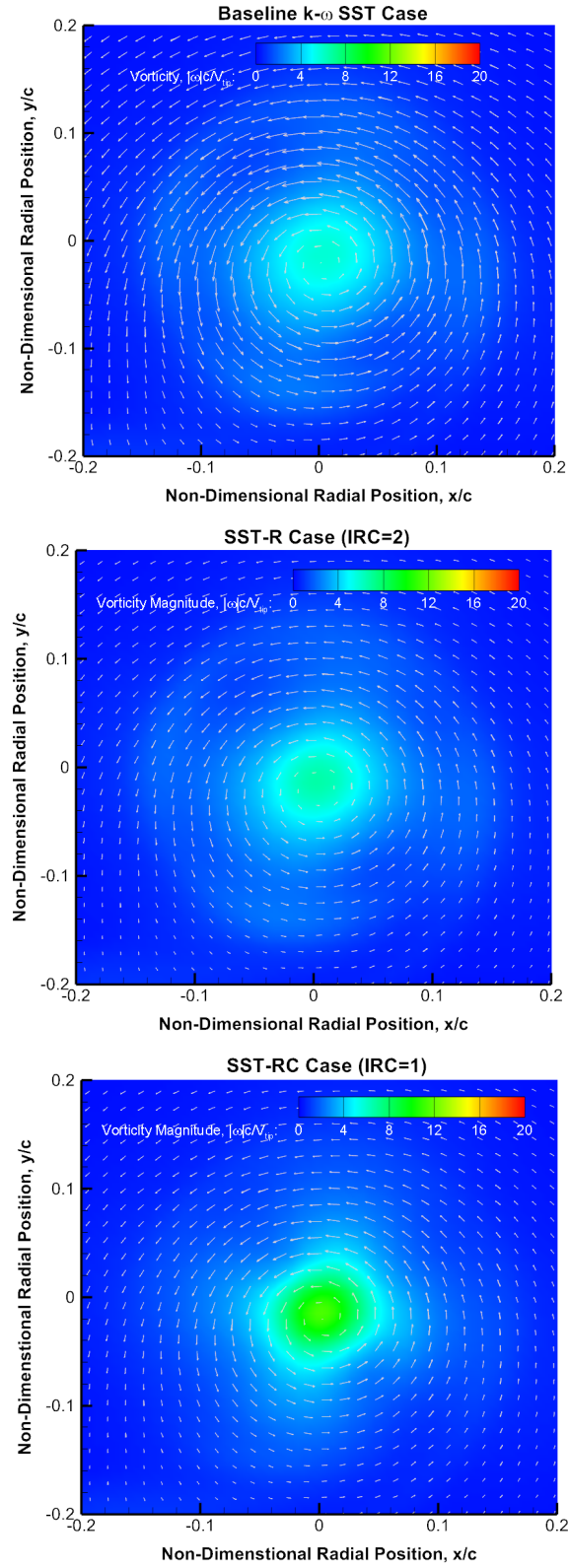


Figure 3.13 SST comparison of vorticity magnitude at $\zeta = 15^\circ$

3.6 Persistence

The overall persistence of the tip vortex was also assessed throughout the wake. To this end, full flow field representations were obtained using iso-surfaces of the Q-criterion and colored by the vertical component of velocity, w , the results being shown for the SA and $k - \omega$ SST models in Figs. 3.16 and 3.19, respectively.

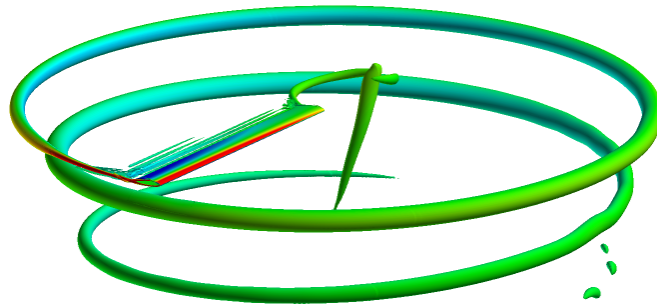


Figure 3.14 Iso-surfaces of Q-criterion colored by w -velocity for SA case.

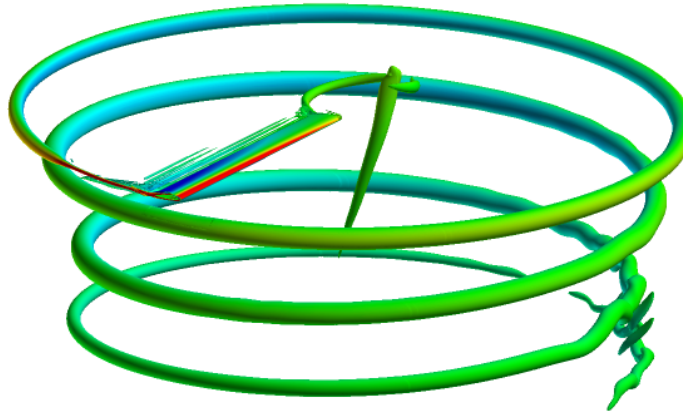


Figure 3.15 Iso-surfaces of Q-criterion colored by w -velocity for SA-R case.

Notice that only the SA-R and SA-RC cases showed that the tip vortex was preserved in the wake until three rotor revolutions, which is consistent with flow visualization performed

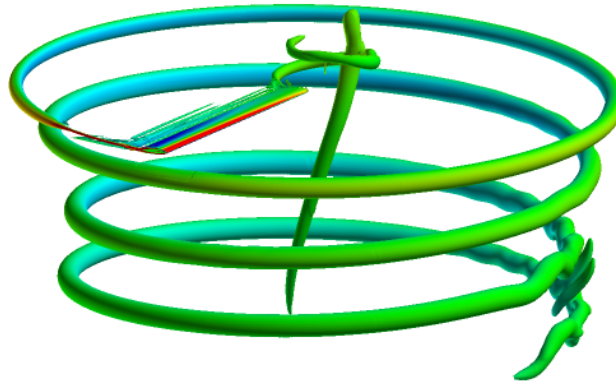


Figure 3.16 Iso-surfaces of Q-criterion colored by w -velocity for SA-RC case.

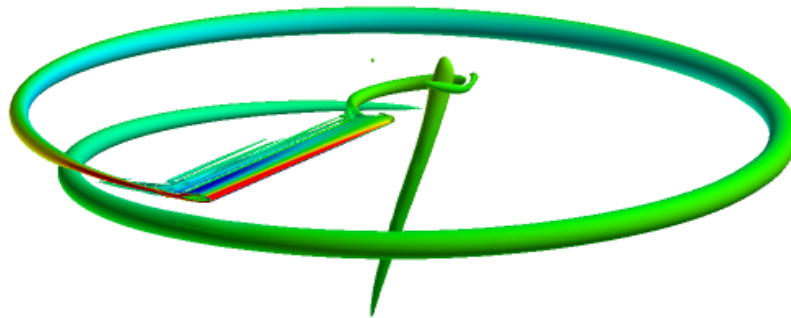


Figure 3.17 Iso-surfaces of Q-criterion colored by w -velocity for SST case.

on this rotor [Ref. 7]. The value of these comparisons of vortex persistence cannot be compared exactly against observations, but they show the effect varying only the turbulence model parameters.

While good predictions of the vortex core size may not be absolutely necessary for the hover condition where the older vortices are convected well below the rotor plane, the same situation may not be true in forward flight. Smaller cores and more concentrated regions of vorticity often lead to far greater loads on the adjacent blades and will likely affect the

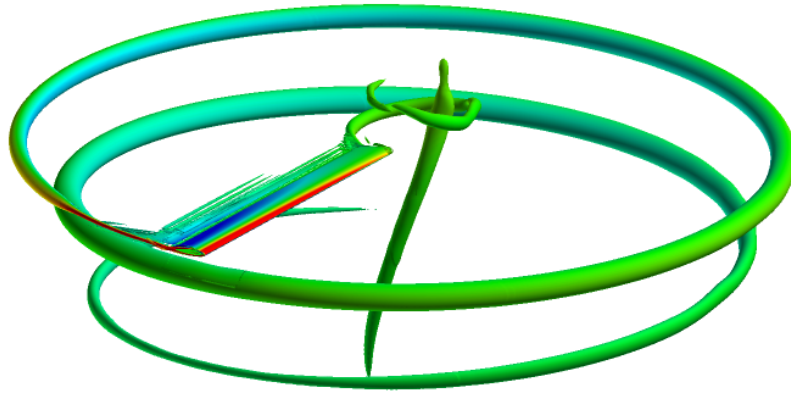


Figure 3.18 Iso-surfaces of Q-criterion colored by w -velocity for SST-R case.

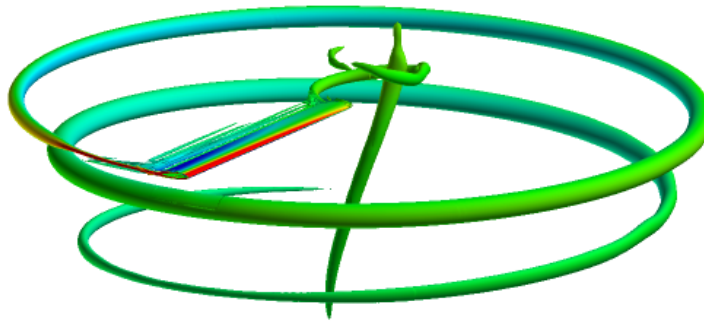


Figure 3.19 Iso-surfaces of Q-criterion colored by w -velocity for SST-RC case.

noise produced by the rotor from blade vortex interactions (BVI), especially in descending flight. Predicting this latter behavior is clearly dependent on the extent to which the tip vortex properties can be preserved to relatively older wake ages on the order of several rotor revolutions.

In addition to the various RANS computations, a DES case was considered to capture the anisotropy of the turbulent fluctuations for comparison with the measured data. An instantaneous flowfield visualization from this case is provided by Fig. 3.22.

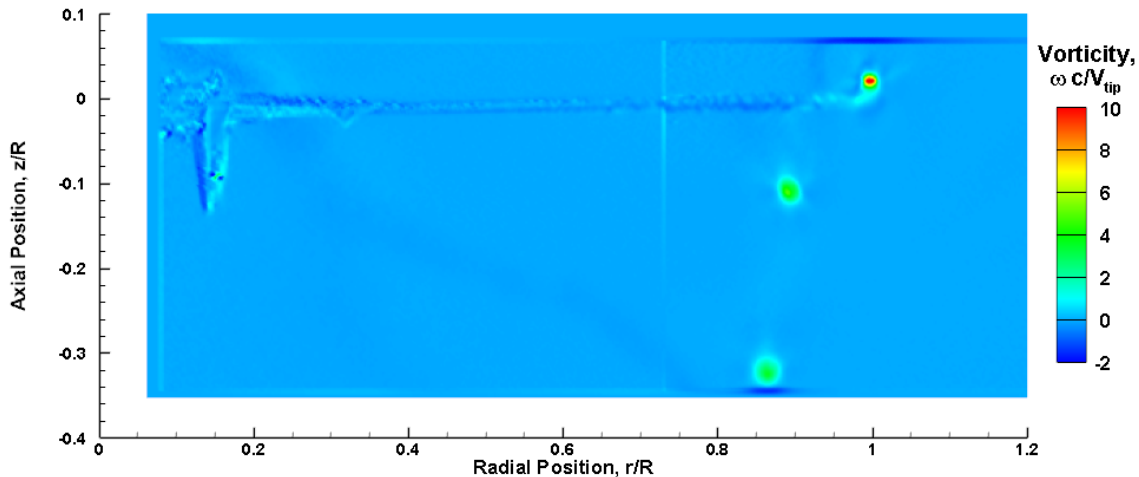


Figure 3.20 Experimental flow field measurements of out-of-plane vorticity.

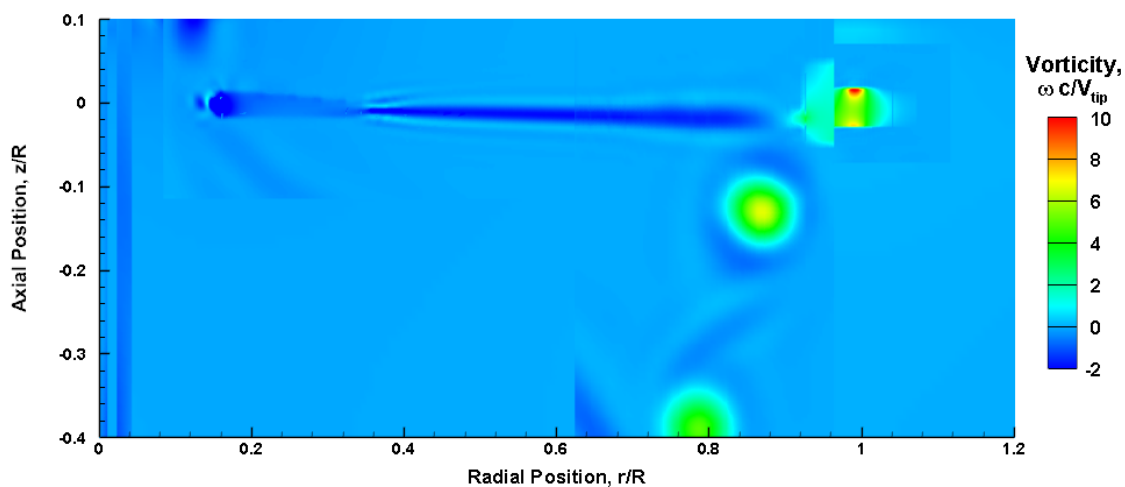


Figure 3.21 SA-RC prediction of out-of-plane vorticity.

The effect of higher-order numerical accuracy on the solution was further exemplified by the results shown in Fig. 3.23, which compares the inviscid cases on the chosen grid refinement to the PIV measurements over later wake ages. The core size is relatively well preserved by the refinement region (see Fig. 3.24), which ends just after 15° . However, past

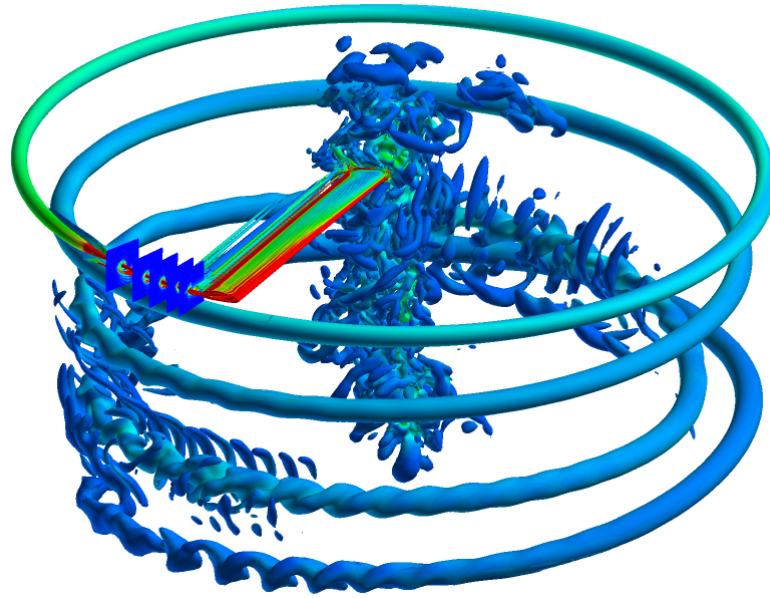


Figure 3.22 Iso-surfaces of Q-criterion colored by vorticity for SA-DES case.

the refinement region, the core size rapidly increased to roughly four or five times the values obtained from the measurements. In this case, the measurements represent an aggregate of core size estimates from Refs. 1, 54 and 55, the different measurements showing good concurrence in the rate at which the core grows with wake age.

While the predicted core size consistently exceeded the measured values, the 6th-order scheme clearly helped to reduce the core size, even in the refined region shown in Fig. 3.24. This outcome shows that the overprediction of the core size is largely influenced by the numerical dissipation, a conclusion that generally agrees with similar findings from other comparative studies such as Refs. 24, 56, and 57.

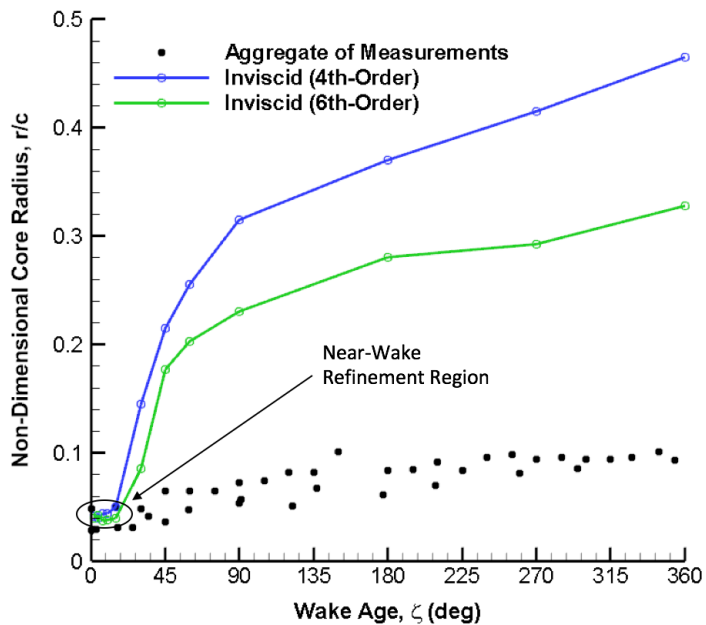


Figure 3.23 Core radius plotted over one complete revolution.

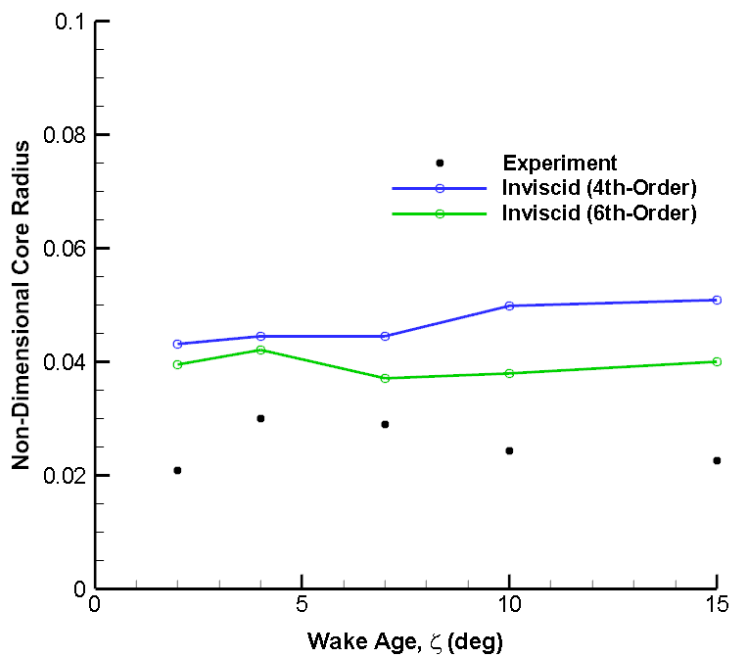


Figure 3.24 Core radius plotted in refined region up to $\zeta = 15^\circ$.

The overestimate of the core size at older wake ages can also be seen by the results in Fig. 3.25, which uses the Q-criterion to show the formation and subsequent growth of the tip vortex, colored by vorticity magnitude. Figure 3.26 shows the region where this growth in core size occurs, clearly associating the rapid growth with a local increase in the grid size.

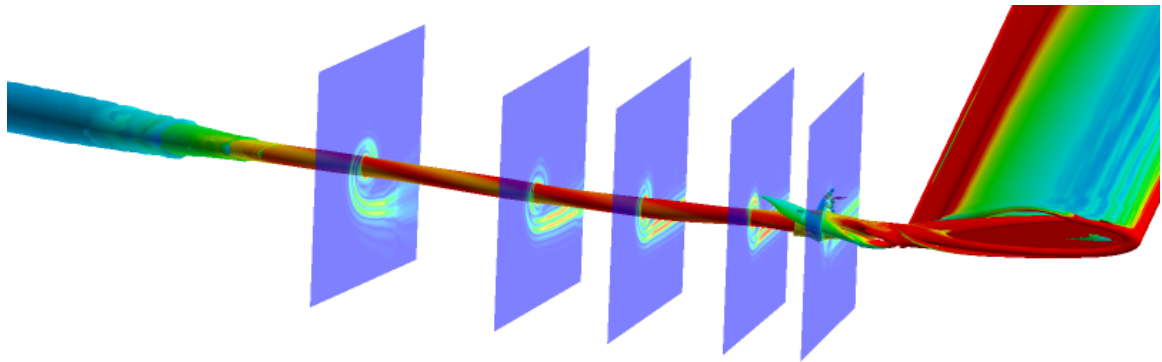


Figure 3.25 Vortex core growth shown directly following refined grid region.

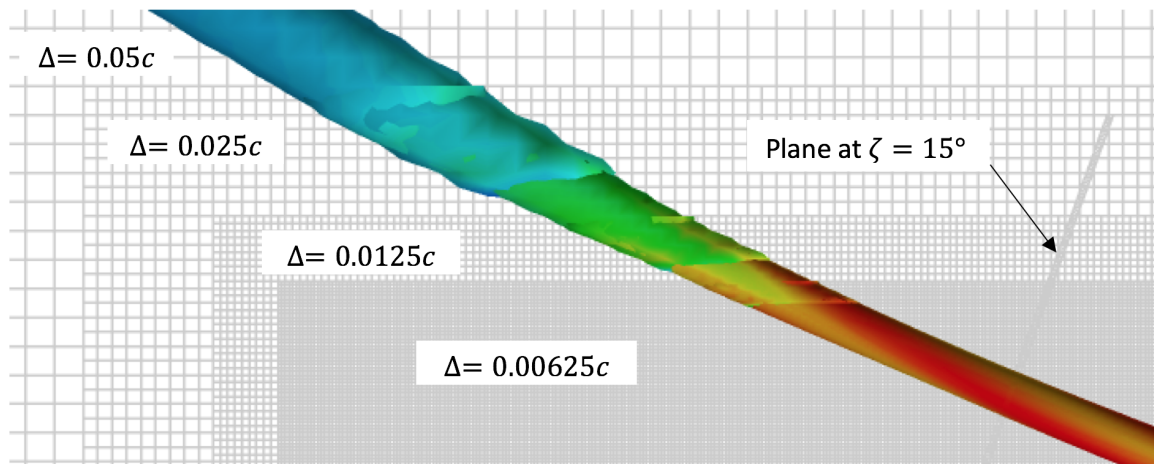


Figure 3.26 Top view of tip vortex transition from highly refined to less refined grid.

3.7 Turbulence

One of the primary goals of the original PIV work reported in Ref. 1 was to obtain turbulence measurements specifically for validation RANS closure models, and the value of such measurements should not be underestimated. An evaluation was performed with respect to the predicted turbulence quantities in the vortex core using various corrected forms of the turbulence models. Some of the results from this work are presented in Figs. 3.29 and 3.30.

Figure 3.29 shows the behavior of the fluctuating $\sqrt{u'^2}$ and $\sqrt{v'^2}$ components from the PIV measurements, which indicate immediately that the turbulence in the tip vortex is non-uniform and anisotropic. The measurements showed that the $\overline{u'}$ and $\overline{v'}$ components reached a maximum at the center of the vortex, with their magnitudes reducing with increasing radial distance away from the core.

The eddy viscosity (or the turbulence) distribution depends on the Reynolds shear stresses, i.e., the $\overline{u'_i u'_j}$ terms, which are summarized by the distribution of $\overline{u'v'}$ shown in Fig. 3.30. These results are at a minimum near the center of the vortex, increase to maximum value close to a radial position of $0.5r_c$, and then diminish further away. The RANS predictions of the eddy viscosity are shown in Figs. 3.33 through 3.36 using the SA and SST models, respectively, with and without each rotational correction.

Vetting the turbulence predictions from the CFD results with respect to the measurements required establishing a qualitative and quantitative means for comparison. The difficulty in assessing the validity of each case against experimental data, however, is fun-

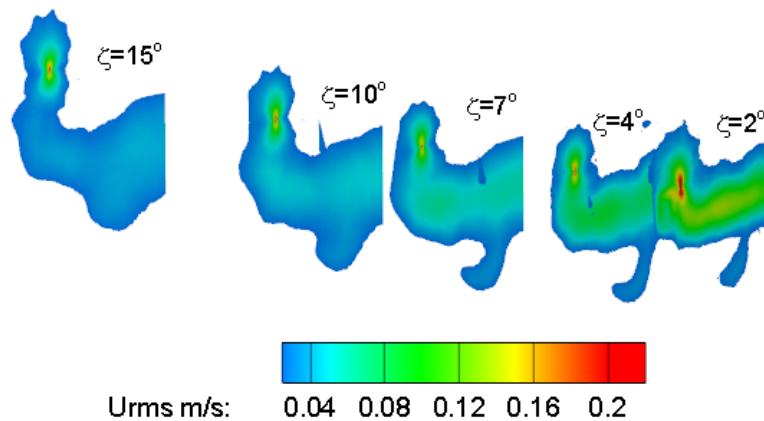


Figure 3.27 Distribution of $\sqrt{u'^2}$ from measurements.

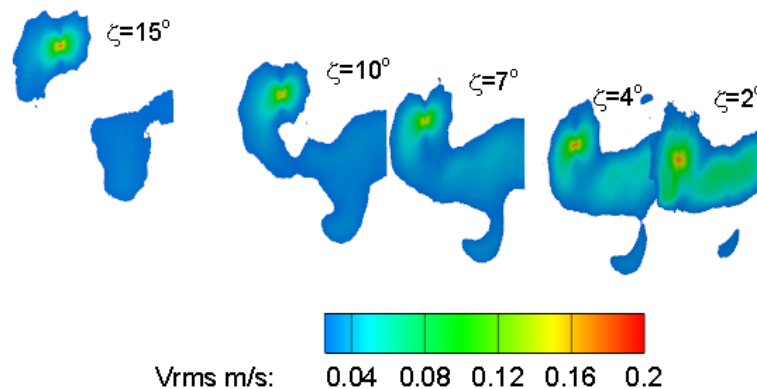


Figure 3.28 Distribution of $\sqrt{v'^2}$ from measurements.

Figure 3.29 Measurements of the fluctuating in-plane velocity in the vortex core.

damentally limited by the Boussinesq linear eddy viscosity assumption. The calculated eddy viscosity was a simplified quantity that assumed isotropic turbulence, with no direct physical analogue. Using this assumption, the eddy viscosity was treated as a linear pro-

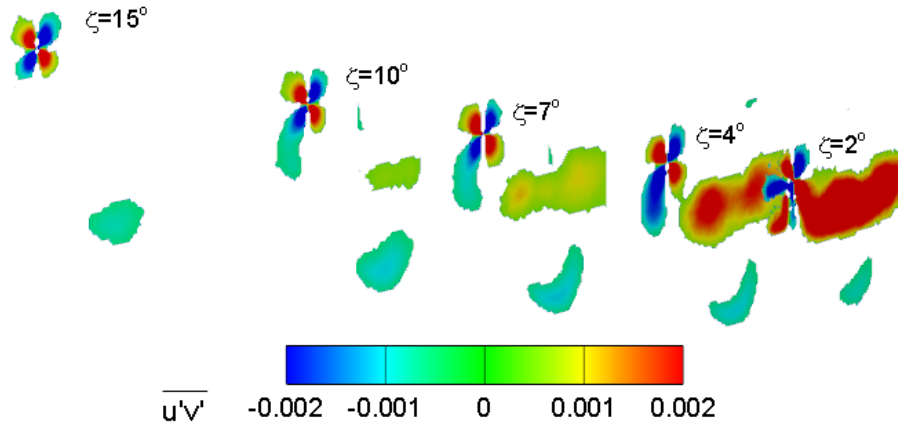


Figure 3.30 Measurements of the Reynolds stress, $\overline{u'v'}$, in the vortex core.

portionality constant to the strain tensor in the calculation of the Reynolds stress terms. For example, the velocity fluctuations were approximated by

$$\overline{(u')^2} = \nu_t \frac{\partial u}{\partial x} + \frac{2}{3}k, \quad \overline{(v')^2} = \nu_t \frac{\partial v}{\partial y} + \frac{2}{3}k \quad (3.1)$$

and the eddy viscosity models then approximated $\overline{u'v'}$ by

$$-\overline{u'v'} = \nu_t \frac{1}{2} \left(\frac{\partial u}{\partial y} + \frac{\partial v}{\partial x} \right) \quad (3.2)$$

The linear eddy viscosity assumption given by Eq. 3.2 provided a means for comparing the Reynolds stress component, $\overline{u'v'}$ between the measurements and RANS simulation. The resulting contours were plotted for the SA model (see Fig. 3.39) and SST model (see Fig. 3.42) in a comparable form to the Reynolds stress measurements shown previously in 3.30.

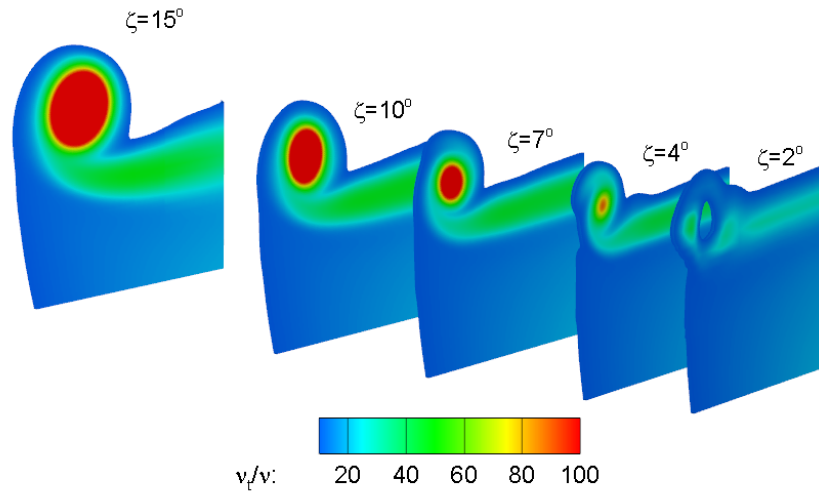


Figure 3.31 Eddy viscosity distribution for SA case

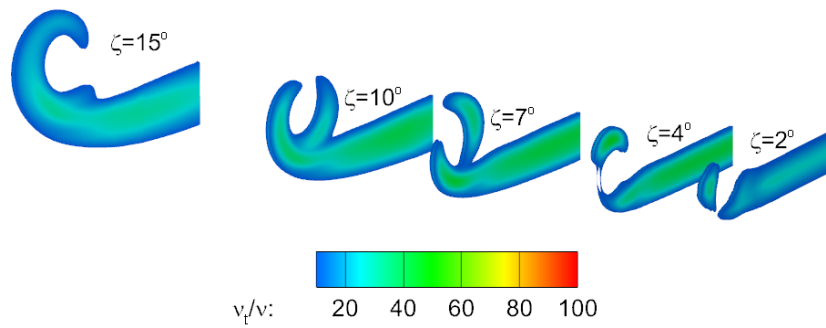


Figure 3.32 Eddy viscosity distribution for SA-R case

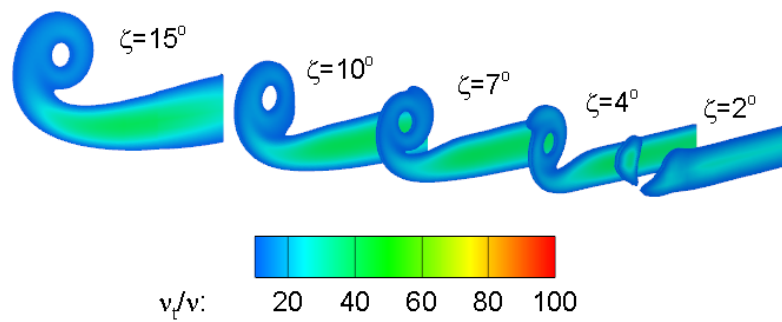


Figure 3.33 Eddy viscosity distribution for SA-RC case

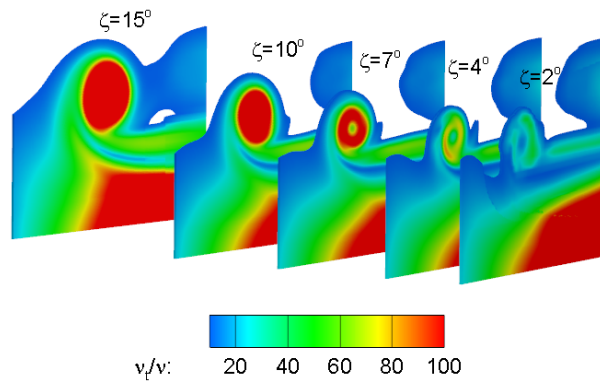


Figure 3.34 Eddy viscosity distribution for SST case

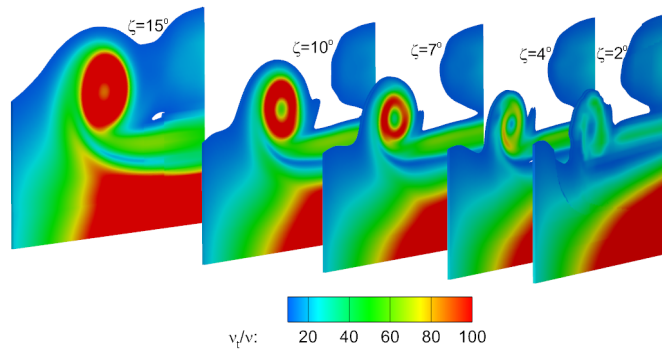


Figure 3.35 Eddy viscosity distribution for SST-R case

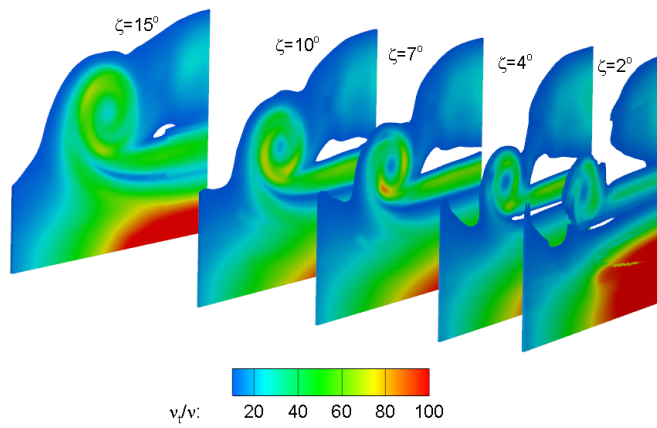


Figure 3.36 Eddy viscosity distribution for SST-RC case

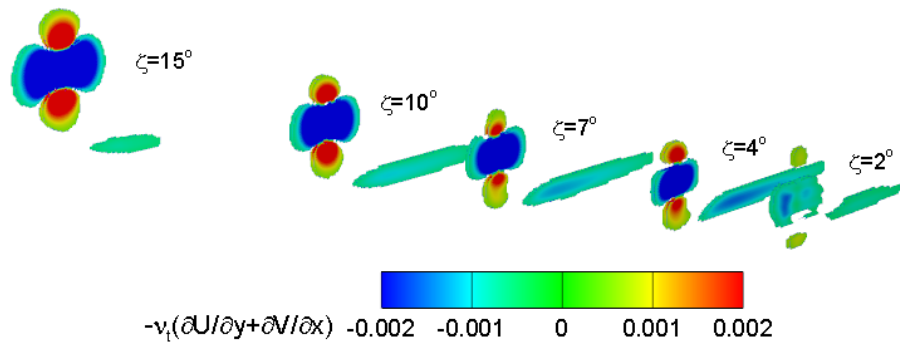


Figure 3.37 Reynolds stress approximation of $\overline{u'v'}$ for SA case

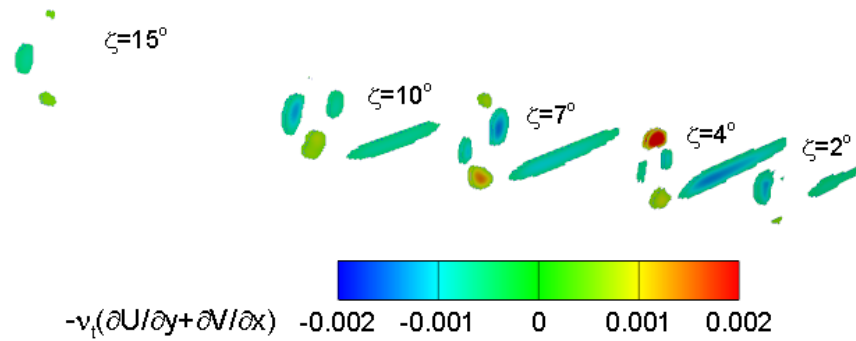


Figure 3.38 Reynolds stress approximation of $\overline{u'v'}$ for SA-R case

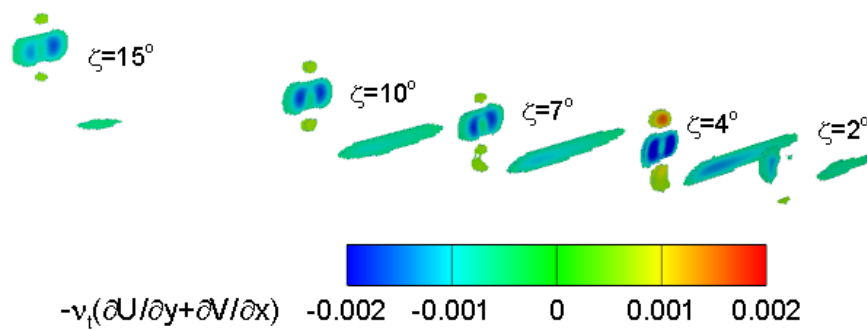


Figure 3.39 Reynolds stress approximation of $\overline{u'v'}$ for SA-RC case

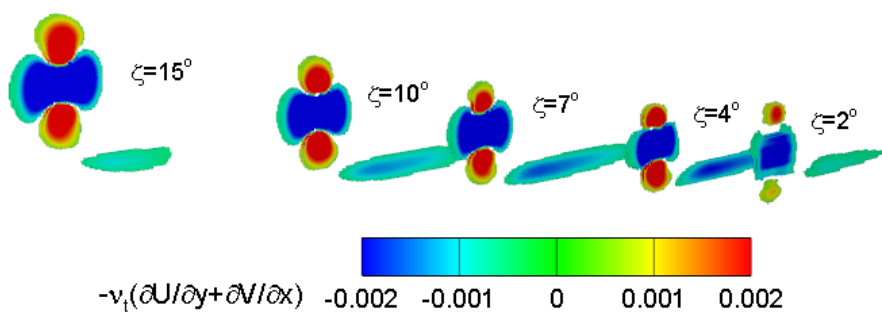


Figure 3.40 Reynolds stress approximation of $\overline{u'v'}$ for SST case

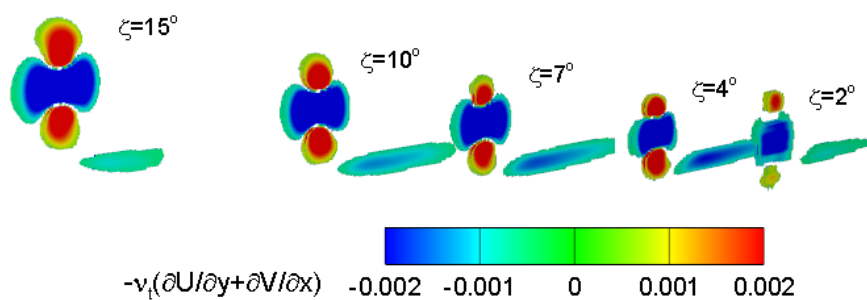


Figure 3.41 Reynolds stress approximation of $\overline{u'v'}$ for SST-R case

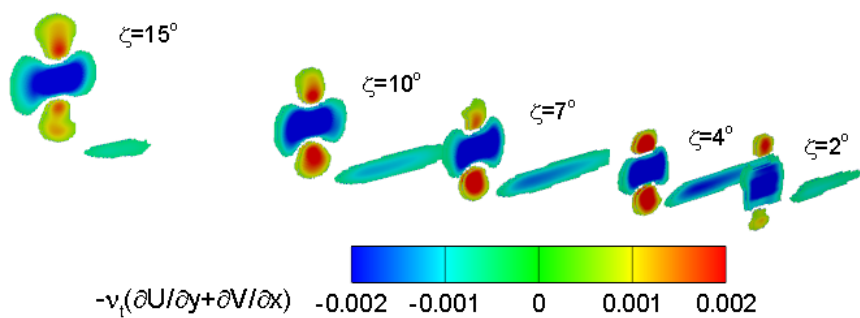


Figure 3.42 Reynolds stress approximation of $\overline{u'v'}$ for SST-RC case

These distributions confirmed the lack of correlation between the linear, isotropic turbulence assumption made by all eddy viscosity models postulated by Refs. 1 and 13. However, they also provided insight to the variation in the turbulent shear stresses in the vortex core between the different turbulence models and their rotational corrections. It is generally understood that anisotropy in the turbulent vortex core may not be possible to model in RANS without the implementation of a 7-equation Reynolds stress model or even by using LES. However, it is important to understand the physical implications of the turbulence predictions made by the commonly implemented eddy viscosity models and corrections because they continue to be widely used.

The comparisons show that both the general rotational correction proposed by Dacles-Mariani et al. [Ref. 45] and the Spalart-Shur rotational/curvature correction [Ref. 29] applied to the SA model greatly reduce the turbulent stress in the vortex core. The upshot is the mitigation of viscous diffusion in the core region, effectively preserving the core size and reducing the spread of vorticity relative to what was obtained by the uncorrected turbulence models. For coarser grid resolutions, this outcome would almost always tend to better match the measurements, in the same way that the inviscid case better preserved core size and vorticity to an extent. However, at this finer resolution the under-prediction of turbulence in the vortex core results in an over-prediction of the peak swirl velocity, and it would likely cause greater differences from the measured velocity distribution in the core as the grid continued to be refined.

The SST-RC case seemed to predict turbulent stresses on a similar scale to the Reynolds stress measurements, which possibly explains why it showed the best agreement to the

measured peak-to-peak swirl velocity. However, even the corrected form of the SST model still over-predicted the core size relative to the baseline (inviscid) and SA-RC cases.

The DES results were examined in addition to the RANS simulations, and the fluctuating components of the velocity were extracted from a transient model of the tip vortex over 2 revolutions using DES; these results are shown in Fig. 3.43

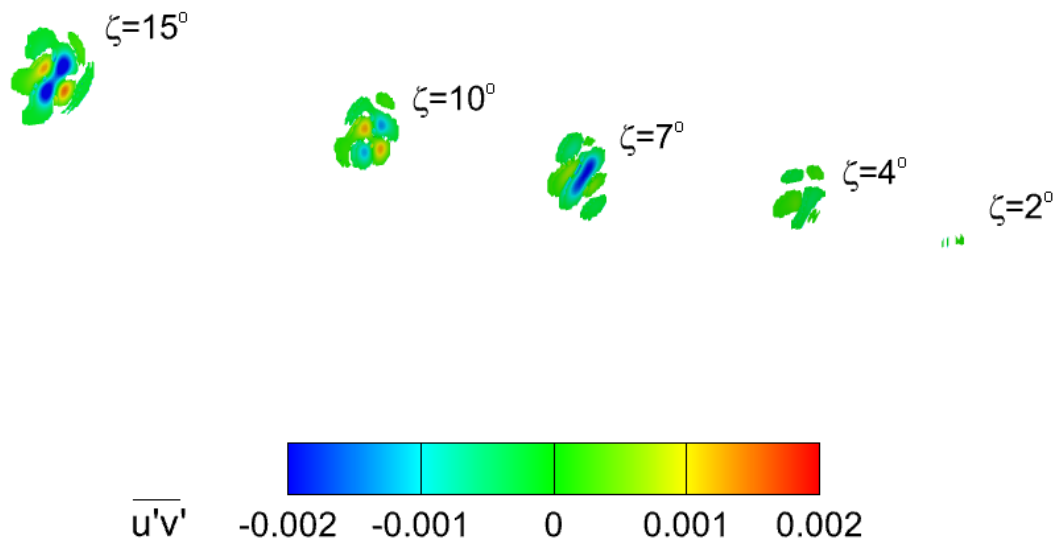


Figure 3.43 Reynolds stress approximation of $\overline{u'v'}$ for SA-DES case

The measurements showed a trend of gradually decreasing Reynolds stresses throughout the first 15° of wake age. On the contrary, the majority of the eddy viscosity turbulence models predicted an increase in Reynolds stress over time. However, this result may have been influenced by applying the Spalart-Shur correction to the near-body grid for the reasons described earlier.

4. Conclusions & Recommendations

Reynolds-Averaged Navier-Stokes (RANS) simulations of the wake properties trailed from a one-bladed rotor have been compared to detailed Particle Image Velocimetry (PIV) measurements of comparable spatial resolution. The effects of the turbulence closure models were systematically assessed by their abilities within the RANS solutions to predict the formative stages of the blade tip vortex, the Reynolds stresses in the developing vortex, the presence of turbulence as flow was entrained into the vortex core region, and the overall persistence of the tip vortex as it aged in the rotor wake. Of particular interest in the present work was to better quantify the effects of the standard “rotational corrections” to the turbulence models compared to the measured turbulence quantities.

4.1 Conclusions

The following conclusions have been drawn from this work.

1. Establishing a nominally periodic hovering wake condition that was faithful to the observed wake geometry required considerable care. By examining various starting conditions for the RANS simulation, it was determined that temporarily imposing a uniform climb inflow velocity was needed to convect the starting vortex ring downstream in the wake of the impulsively started rotor. This approach also allowed a periodic wake solution to be established minimizing time and computational cost.

2. A grid independence study demonstrated the value of higher-order numerical schemes in capturing the steep velocity gradients in the rotor wake, but also highlighted the difficulties in establishing a truly grid-independent solution. A 6th-order central differencing scheme allowed a slightly less refined grid to be used to give comparable outcomes to one with higher spatial resolution. For already highly refined grids, increasing the order of the numerical scheme increased the net computational cost by only 10%. The effect of the higher-order numerical scheme also gave beneficially smaller values of the predicted vortex core size throughout the off-body mesh region.
3. It was found, in general, that the inviscid and laminar assumptions imposed in the RANS solutions overpredicted the swirl velocity and underpredicted the core size of the tip vortex compared to the PIV measurements, while the uncorrected turbulence models significantly underpredicted the swirl velocity and overpredicted the core. Overall, the results indicated that turbulence played a significant role in modulating the peak swirl velocities in the rotor wake, but had a far more limited contribution in establishing the growth of the vortex core.
4. Regardless of differences in core size, peak swirl velocity, and vorticity, the net circulation of the vortex was very accurately modeled by each of the computational cases. This outcome verified that the models are in agreement with Helmholtz's theorems, in that the strength (circulation) of the vortex is preserved. Although the circulation was well-predicted outside of the viscous core, the importance of accurately modeling the flow within the viscous region should not be understated. Indeed, the size of

the vortex core has a significant effect in regard to vortex interactions with the airframe, rotor blades, and adjacent vortices. Even though the grid size and numerical scheme were found to have a greater influence on the core properties than the turbulence model parameters, the comparative analysis performed in this thesis shows that there are large discrepancies between the physical and predicted vortex properties when the influence of the grid is reduced.

5. Each of the rotational correction terms to the turbulence models provided better agreement to the PIV measurements than the baseline models, but to a varying degree. The SA-R and SA-RC corrections had the greatest effect on the solution, with the SA-RC providing the least diffusion of vorticity. However, the SA-RC model did not necessarily provide the closest agreement to the PIV measurements. The predictions with the SST-RC model, however, provided better agreement with the measured peak swirl velocities, but also predicted a quicker diffusion of vorticity and so a larger core size. The extent of the viscous diffusion of vorticity caused by each incarnation of the $k - \omega$ SST model was exemplified by an overall reduction in the vortex persistence throughout the rotor wake.
6. The physical characteristics of each solution were found to correlate directly to the turbulence predictions that were made inside and adjacent to the tip vortex. For example, the SA-R and SA-RC corrections, which provided the greatest peak swirl and persistence of the vortex, did so because they predicted the lowest values of eddy viscosity. The magnitudes of predicted eddy viscosity, generally showed that the

effects of turbulence lay somewhere between the predictions made by the SA-RC and SST-RC (corrected) models. Although the SA-R correction underpredicted the vorticity and the persistence of the vortex, it predicted lower turbulence in the vortex relative to the SA-RC model. The SST-R correction showed a small effect overall and provided the poorest comparison with the measurements.

7. All of the baseline turbulence models and their rotational corrections failed to capture distribution of the Reynolds stress that was determined in the PIV measurements. Indeed, the measurements showed a distribution of Reynolds stress that was offset 45° from the strain, and so this result was fundamentally different to the distributions assumed by each of the eddy viscosity turbulence models. This outcome is because of the linear stress-strain relationship and underlying the Boussinesq assumption that are implicit within each of the turbulence models that were considered. This discrepancy with measurements will likely need to be overcome by the implementation of anisotropic (cubic) eddy viscosity models, the use of Reynolds stress models, or by using LES.

4.2 Recommendations for Future Work

In terms of future work, it is clear that the correction terms to the RANS turbulence models that are currently available for use in vortex flows must continue to be understood with respect to the physical behavior of the turbulence in the vortex before they can be applied to more complex rotor problems. The interdependency of the turbulence model-

ing parameters and numerical discretization suggests that further work is also required to develop a RANS closure model that can better capture the flow physics of a turbulent tip vortex once the required spatial resolution is obtained.

Specifically, moving forward, the RANS simulations provided in this thesis should be compared to methods such as LES and DES, which are becoming increasingly more common. Such methods have shown promising results regarding the mean flow properties, at the time of writing these conclusions, little to no work has been done to evaluate the turbulent fluctuations against experimental data. It would be very important to see whether the DES simulations provided similar Reynolds stress levels and distributions to those shown by the measurements.

In addition to the computational work of simplified cases that are required to better understand present modeling capabilities, additional experiments need to be conducted for larger scale rotors, with emphasis on the tip vortex properties. Currently limited measurements exist resolving the flow field of a rotor wake, and understandably so, given the complexity of the problem. However, it is important that effort be directed towards better understanding these detailed flow features. By simplifying the problem and performing a comparative analysis with no ulterior motive but to evaluate current methods from an academic perspective, the flow physics can be better understood, as well as the efficacy of the computational models.

Bibliography

- [1] Ramasamy, M., Johnson, B., and Leishman, J. G., “Turbulent Tip Vortex Measurements Using Dual-Plane Stereoscopic Particle Image Velocimetry,” *AIAA Journal*, Vol. 478, No. 8, 2009, pp. 1826–1840.
- [2] Leishman, J. G., *The Helicopter: Thinking Forward, Looking Back*, The College Park Press, College Park, MD, 2007.
- [3] Duque, E. P. N., Toyoda, A., Burklund, M. D., Hariharan, N., Narducci, R., and Stone, C. P., “Direct Comparison of Hover Prediction Workshop Results,” AIAA Paper No. 2016-0035, 54th AIAA Aerospace Sciences Meeting, San Diego, CA, 4–8 January, 2016.
- [4] Hariharan, N., Narducci, R., Reed, E., and Egolf, T. A., “Helicopter Aerodynamic Modeling of Rotor with Tip-Shape Variations: AIAA Standardized Hover Evaluations,” AIAA Paper No. 2016-0031, 54th AIAA Aerospace Sciences Meeting, San Diego, CA, USA, 4–8 January, 2016.
- [5] Leishman, J. G., *Principles of Helicopter Aerodynamics*, Cambridge University Press, New York, NY, 2nd Edition, 2006.

- [6] Gray, R. B., “An Aerodynamic Analysis of a Single-Bladed Rotor in Hovering and Forward Flight as Determined by Smoke Studies on the Vorticity Distribution in the Wake,” Princeton University, Report Number 356, 1956.
- [7] Milluzzo, J. and Leishman, J. G., “Fluid Dynamics of the Helicoidal Wake Sheets Trailed from a Hovering Rotor,” *Journal of the American Helicopter Society*, Vol. 61, No.1, January 2016, pp. 1–17.
- [8] Leishman, J. G. and Bhagwat. M. J., “Correlation of Helicopter Rotor Tip Vortex Measurements,” *AIAA Journal*, Vol. 38, No. 2, February 2000, pp. 301–308.
- [9] Spalart, P. R. and Allmaras, S. R., “A One-Equation Turbulence Model for Aerodynamic Flows,” *La Recherche Aérospatiale*, Vol. 1, pp. 5–21.
- [10] Menter, F. R., “Two-Equation Eddy-Viscosity Turbulence Models for Engineering Applications,” *AIAA Journal*, Vol. 32, No. 8, 1994, pp. 1598–1605.
- [11] Potsdam, M. and Pulliam, T., “Turbulence Modeling Treatment for Rotorcraft Wakes,” 46th American Helicopter Society Specialists Conference on Aeromechanics, San Fransisco, CA, 23–25 January, 2008.
- [12] Yoon, S., Pulliam, T. H., and Chaderjian, N. M., “Simulations of XV-15 Rotor Flows in Hover Using OVERFLOW,” Fifth Decennial AHS Aeromechanics Specialists’ Conference, San Francisco, CA, 22–24 January, 2014.
- [13] Chow, J., Zilliac, G., and Bradshaw, P., “Turbulence Measurements in the Near Field of a Wingtip Vortex,” NASA-TM-110418, 1997.

- [14] Wilcox, D. C., *Turbulence Modeling for CFD*, DCW Industries, Incorporated, La Cañada, CA, 1994.
- [15] Pope, S. B., *Turbulent Flows*, Cambridge University Press, New York, NY, 2000.
- [16] Chaderjian, N. M. and Ahmad, J. U., “Detached Eddy Simulation of the UH-60 Rotor Wake Using Adaptive Mesh Refinement,” American Helicopter Society 68th Annual Forum, Fort Worth, TX, 1–3 May, 2012.
- [17] Nichols, R. H. and Buning, P. G., *User’s Manual for OVERFLOW 2.2*, 2016.
- [18] Chaderjian, N. M., “High-Resolution Navier-Stokes Simulation of Rotorcraft Wakes,” Proceedings to the SC10 International Conference for High Performance Computing, Networking, Storage, and Analysis, New Orleans, LA, 15–18 November, 2010.
- [19] Hariharan, N., Potsdam, M., and Wissink, A., “Helicopter Rotor Aerodynamic Modeling in Hover Based on First-Principles: State-of-the-Art and Remaining Challenges,” AIAA Paper No. 2012-1066, 50th AIAA Aerospace Sciences Meeting including the New Horizons Forum and Aerospace Exposition, Nashville, TN, 9–12 January, 2012.
- [20] Chan, W. M., Rogers, S. E., Pandya, S. A., Kao, D. L., Buning, P. G., Meakin, R. L., Boger, D. A., and Nash, S. M., *Chimera Grid Tools User’s Manual*, 2010.
- [21] Meakin, R., “Unsteady Simulation of the Viscous Flow About a V-22 Rotor and Wing in Hover,” AIAA Paper No. 95-3463, AIAA Atmospheric Flight Mechanics Conference, Baltimore, MD, 7–10 August, 1995.

- [22] Hariharan, N. and Sankar, L. N., “Higher Order Numerical Simulation of Rotor Flow Field,” American Helicopter Society Forum and Technology Display, Washington, D. C., 11–13 May, 1994.
- [23] Kim, H., Williams, M. H., and Lyrintzis, A. S., “An Improved Method for Rotor Wake Capturing,” *AIAA Journal of Aircraft*, Vol. 39, No. 5, June, 2001, pp. 794–803, .
- [24] Chaderjian, N. M., “Advances in Rotor Performance and Turbulent Wake Simulation Using DES and Adaptive Mesh Refinement,” ICCFD7-3506, Seventh International Conference on Computational Fluid Dynamics, Big Island, HI, 9–13 July, 2012.
- [25] Hariharan, N., Egolf, A., and Sankar, L., “Simulation of Rotor in Hover: Current State and Challenges,” AIAA Paper No. 2014-0041, 52nd Aerospace Sciences Meeting, National Harbor, MD, 13–17 January, 2014.
- [26] Jain, R. “A Comparison of CFD Hover Predictions for the Sikorsky S-76 Rotor,” AIAA Paper No. 2016-0032, 54th AIAA Aerospace Sciences Meeting, San Diego, CA, USA, 4–8 January, 2016.
- [27] Kolmogorov, A. N., “On Degeneration of Isotropic Turbulence in an Incompressible Viscous Liquid,” *Dokl. Akad. Nauk SSSR*, Vol. 31, pp. 538–540, 1941.
- [28] Davidson, P. A., *Turbulence: An Introduction for Scientists and Engineers*. Oxford University Press, New York, NY, 2004.

- [29] Spalart, P. R. and Shur, M., “On the Sensitization of Turbulence Models to Rotation and Curvature,” *Aerospace Sciences and Technology*, Vol. 1, No. 5, 1997, pp. 297–302.
- [30] Dacles-Mariani, J., Zilliac, G. G., Chow, J. S., and Bradshaw, P., “Numerical/Experimental Study of a Wingtip Vortex in the Near Field,” *AIAA Journal*, Vol. 33, No. 9, 1995, pp. 1561–1568.
- [31] Dacles-Mariani, J., Kwak, D., and Zilliac, G. G., “On Numerical Errors and Turbulence Modeling in Tip Vortex Flow Production,” *International Journal for Numerical Methods in Fluids*, Vol. 30, No. 1, 1999, pp. 65–82.
- [32] Ramasamy, M., Johnson, B., Huisman, T., and Leishman, J. G., “A New Method for Estimating Turbulent Vortex Flow Properties from Stereoscopic DPIV Measurements,” Proceedings of the American Helicopter Society 63rd Annual National Forum, Virginia Beach, VA, May, 2007.
- [33] Pulliam, T. H., Solution Methods in Computational Fluid Dynamics, *NASA Ames Research Center*, 1986.
- [34] Nichols, R. H. and Buning, P. G., *OVERFLOW 2 Training Class*, 2010.
- [35] Garnier, E., Adams, N., and Sagaut, P., *Large Eddy Simulation for Compressible Flows*, Springer, Netherlands, 2009.
- [36] Rumsey, C., Turbulence Modeling Resource, *Langley Research Center*, 2015.
<https://turbmodels.larc.nasa.gov/>.

- [37] Lorin, E., Ali, A. B. H., and Soulaïmani, A., “A Positivity Preserving Finite Element/Finite Volume Solver for the Spalart-Allmaras Turbulence Model,” *Computer Methods in Applied Mechanics and Engineering*, Vol. 196, No. 17-20, 2007, pp. 2097–2116.
- [38] Bradshaw, P., “The Analogy Between Streamline Curvature and Buoyancy in Turbulent Flow,” *Journal of Fluid Mechanics*, Vol. 36, No. 1, 1969, pp. 177-191.
- [39] Bradshaw, P., “Effects of Streamline Curvature on Turbulent Flow,” *AGARDograph*, Vol. 169, 1973.
- [40] Wilcox, D. and Chambers, T., “Streamline Curvature Effect on Turbulent Boundary Layers,” *AIAA Journal*, Vol. 15, No. 4, 1977, pp. 574–580.
- [41] Cotel, A. J. and Breidenthal, R. E., Turbulence Inside a Vortex, *Physics of Fluids*, Vol. 11, No. 10, 1999, pp. 3026–3029, 1999.
- [42] Cotel, A. J., “Turbulence Inside a Vortex: Take 2,” *Physics of Fluids*, Vol. 14, No. 8, 2002, pp. 2933–2934.
- [43] Ramasamy, M. and Leishman, J. G., “A Reynolds Number-Based Blade Tip Vortex Model,” 61st Annual Forum of the American Helicopter Society International, Grapevine, TX, 1–3 June, 2005.
- [44] Hellsten, A., “Some Improvements in Menter’s $k-\omega$ SST Turbulence Model,” AIAA Paper No. 98-2554, 29th AIAA Fluid Dynamics Conference, Albuquerque, NM, 15–18 June, 1997.

- [45] Dacles-Mariani, J., Zilliac, G. G., Chow, J. S., and Bradshaw, P., “Numerical/Experimental Study of a Wingtip Vortex in the Near Field,” *AIAA Journal*, Vol. 33, No. 9, 1995, pp. 1561–1568.
- [46] Nichols, R. H., “Algorithm and Turbulence Model Requirements for Simulating Vortical Flows,” AIAA Paper No. 2008-337, 46th AIAA Aerospace Sciences Meeting and Exhibit, Reno, NV, 7–10 January, 2008.
- [47] Knight, D. D. and Saffman, P., “Turbulence Model Predictions for Flows with Significant Mean Streamline Curvature,” AIAA Paper No. 78-258, AIAA 16th Aerospace Sciences Meeting, Huntsville, AL, 16–18 January, 1978.
- [48] Smirnov, P. E. and Menter, F. R., “Sensitization of the SST Turbulence Model to Rotation and Curvature by Applying the Spalart-Shur Correction Term,” *ASME Journal of Turbomachinery*, Vol. 131, No. 4, 2009.
- [49] Chaussee, D. S. and Pulliam, T. H., “A Diagonal Form of an Implicit Approximate-Factorization Algorithm,” *Journal of Computational Physics*, Vol. 39, 1981, pp. 346–363.
- [50] Schauerhamer, D. G. and Robinson, S. K., “A Validation Study of OVERFLOW for Wing-Tip Vortices,” AIAA Paper No. 2016-1782, 8th AIAA Atmospheric and Space Environments Conference, Washington, D. C., 13–17 June, 2016.

- [51] Meakin, R., “Object X-Rays for Cutting Holes in Composite Overset Structured Grids,” AIAA Paper No. 2001-2537, 15th AIAA Computational Fluid Dynamics Conference, Anaheim, CA, 11–14 June, 2001.
- [52] Taylor, M. K., “A Balsa-Dust Technique for Air-Flow Visualization and Its Application to Flow Through Model Helicopter Rotors in Static Thrust,” NACA, TN-2220, 1950.
- [53] Carpenter, P. J and Friedovich, B., “Effect of A Rapid Blade-Pitch Increase on the Thrust and Induced-Velocity Response of a Full-Scale Helicopter Rotor,” NACA TN 3044, 1953.
- [54] Martin, P. B., Pugliese, G. J., and Leishman, J. G., “High Resolution Trailing Vortex Measurements in the Wake of a Hovering Rotor,” *Journal of the American Helicopter Society*, Vol 48, No. 1, 2003, pp. 39–52.
- [55] McAlister, K. and Heineck, J. “Measurements of the Early Development of Trailing Vorticity From a Rotor,” NASA/TP-2002-211848, AFDD/TR-02-A001, May, 2002.
- [56] Pulliam, T. H., “High Order Accurate Finite-Difference Methods as seen in OVERFLOW,” AIAA Paper No. 2011-3851, 20th AIAA Computational Fluid Dynamics Conference, Honolulu, HI, 27–30 June, 2011.
- [57] Jain, R., “CFD Performance and Turbulence Transition Predictions on an Installed Model-scale Rotor in Hover,” AIAA Paper No. 2017-1871, 55th AIAA Aerospace Sciences Meeting, Grapevine, TX, 9–13 January, 2017.

- [58] Ramasamy, M. , Johnson, B. , Huismann, T., and Leishman, J. G., “Digital Particle Image Velocimetry Measurements of Tip Vortex Characteristics Using an Improved Aperiodicity Correction,” *Journal of the American Helicopter Society*, Vol. 54, No. 1, 2009, pp. 12004.

A. Locating the Vortex Center

The center of the vortex is conceptually understood as the rotational axis of the body of swirling fluid comprising the vortex, however, determining its exact location can be somewhat elusive. In the case of a rotor tip vortex, the line prescribing this axis (i.e., everywhere tangent to the vorticity vector and positioned at the vortex center) follows a helical path, while convecting radially inward (see Fig. 1.2).

Therefore, on a plane perpendicular to the rotational axis, or vortex filament, the center could be located as the point of maximum vorticity, given by the curl of the velocity field, i.e.,

$$\boldsymbol{\omega} = \nabla \times \mathbf{V} \quad (\text{A.1})$$

In an experiment using flow field visualization, this location typically correlates to where a seed particle remains stationary, and where the velocity magnitude drops to a local minimum. However, the convection of the vortex downward below the rotor disk plane, as well as inward toward the rotational axis of the rotor blade, must also be taken into account when determining the position of the vortex center by this method.

Therefore, rather than subjectively identifying the vortex center from the velocity vector field, a helicity-based approach was implemented to calculate the center of the vortex [Ref. 58]. Helicity is traditionally defined by

$$H_{\Psi} = \mathbf{V} \cdot \boldsymbol{\omega} \quad (\text{A.2})$$

but was simplified by the present study to

$$H_{\Psi} \approx V_{\text{ax}} \boldsymbol{\omega}_z \quad (\text{A.3})$$

where $\boldsymbol{\omega}_z$ defines the streamwise or out-of-plane component of vorticity. This quantity is plotted in Fig. A.1 to show how the maximum helicity was used to identify the vortex center.

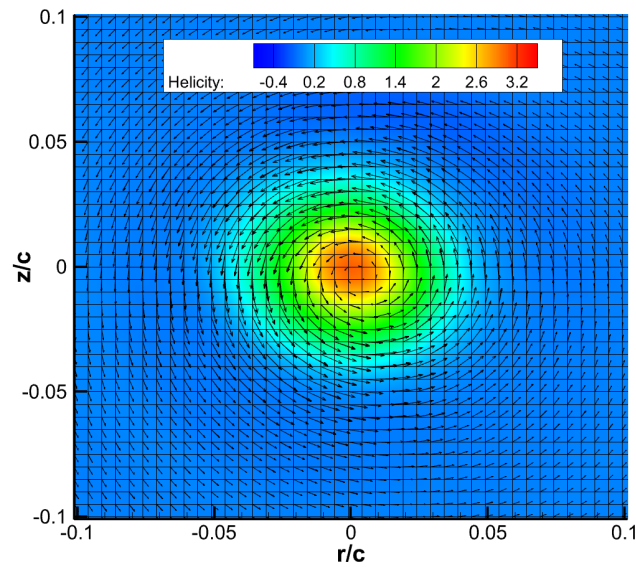


Figure A.1 Helicity-based method for determining vortex center.

B. Calculating Core Size and Peak Swirl Velocity

After determining the index of the center position on the numerical grid, a horizontal slice was taken through this location. The vertical component of velocity, w , was then plotted against the radial position, r . As described in Section 2.5.2, the grid refinement in the near-wake region provided approximately 7 points in the vortex center, so there was some uncertainty in which node defined the maximum value of velocity.

To mitigate the subjectivity of this calculation, a cubic spline interpolation was performed between the available data points using MATLAB, and the maximum velocity and core radius was extracted from this spline. The important point to draw from this is that the core size and peak swirl velocity were calculated from comparable data sets, using an identical methodology. One of the impediments in the efficacy of comparative analyses is the differences in methods employed by various researchers for obtaining vortex core properties. By working directly from the velocity measurements and computational flow field predictions, this source of potential inaccuracy was avoided.

C. Calculating Vortex Circulation

The circulation, which is often used to describe the strength of a vortex, is given by

$$\Gamma = \oint_C \vec{V} \cdot d\vec{s} \quad (\text{C.1})$$

In the present study, the solution was interpolated onto a 360 by 100 node circular grid, as shown in Fig. C.1. Then, the closed loop integration for circulation was performed numerically on each of the concentric, circular paths defined by the radial node locations.

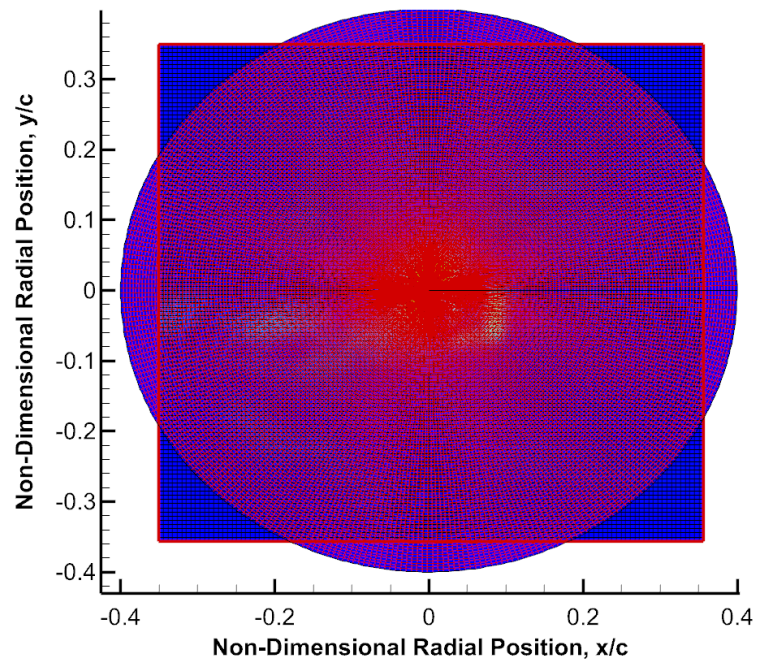


Figure C.1 Grid interpolation used for numerical integration of vortex circulation.

In a potential flow field, the circulation should theoretically remain constant, as the swirl velocity outside of the viscous core region decreases by inverse of the radial distance from the vortex core, i.e.,

$$V_{\theta} = \frac{\Gamma}{2\pi r} \quad (\text{C.2})$$

However, the viscous effects of the laminar region of nearly solid-body rotation in the vortex core and turbulent flow surrounding this region reduce the circulation near the vortex center from that of a fully potential vortex. Any non-zero value of circulation at the vortex center would require an infinite swirl velocity, as can be inferred from Eq. C.2. Therefore, calculating the circulation of a vortex requires taking multiple closed-loop integrals around the vortex core until the circulation becomes independent of the path along which the integral is taken.

An example of the circulation calculated by this integration is given by Fig. C.2. It is important to note that the circulation never fully converged on a value in the limited domain around the vortex where the PIV measurements were performed. This is likely because of the viscous effects of the turbulent, vortical wake sheet, which prevent the behavior of the external flow field from being fully potential, making it difficult to obtain a path independent integral result for circulation.

Because the circulation never fully converged on a single value, the maximum value of circulation was taken from the distribution at similar radial locations between the measurements and computational data. This methodology allowed for proper comparison between the results.

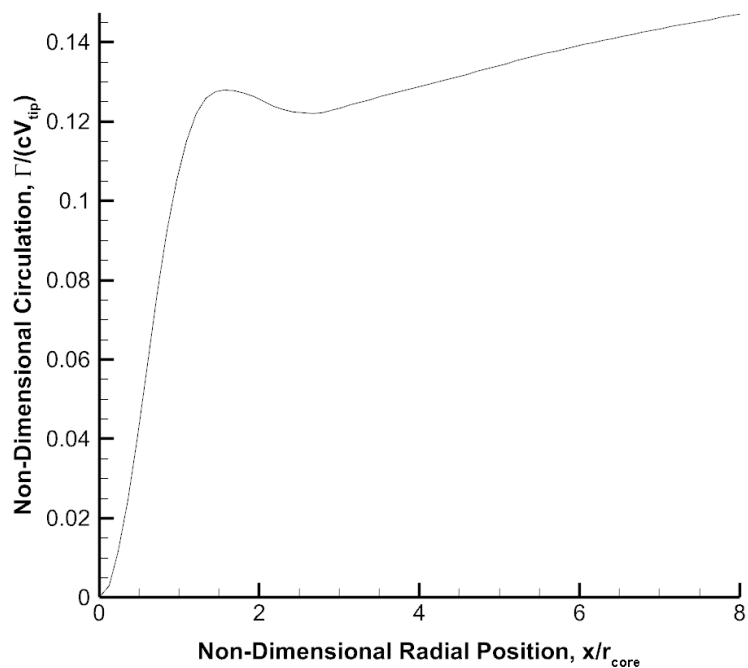


Figure C.2 Circulation from experimental measurements.

As mentioned in Section 3.4, the radial position was non-dimensionalized by the radius of the core extracted from the measurements, rather than from the varying predictions of core radius provided by the numerical simulations.

D. OVERFLOW Input Files

D.1 Namelist Input (over.namelist)

```

$GLOBAL
RESTRT = .F., !need q.restart
NSTEPS = 1, !nrev*1440
NSAVE = 360, !save
NQT = 102, !turbulence model (SA)
!NQT = 205, !turbulence model (SST)
!NQT = 302, !transition model (SA)
!NQT = 405, !transition model (SST)
NQC = 0, !single species
NITNWT = 15, !temporal sub-iterations
DTPHYS = 0.03978, !time step
FSONWT = 2, !time marching order
RF = 0.109611, RFAXIS=3, !rotational frequency (70*pi rad/s)
ISTART_QAVG = 0, !generate q.avg
!DEBUG = 1, !write q.turb
$END

$OMIGLB
IRUN = 0,
LFRINGE = 3, !fringe points
DYMCS = .F.,
I6DOF = 2, !use Config.xml
IBXMIN = 47, IBXMAX = 47,
IBYMIN = 47, IBYMAX = 47, !impose freestream
IBZMIN = 47, IBZMAX = 47,
NREFINE = 4, !refinement levels
LAMINAR_OB = .F., !force off-body grids to be laminar
NADAPT = 180, !regenerate off-body grids every 90 deg
ETYPE = 1, !sensor function for vorticity magnitude
EREFINE = 0.076, !solution error estimate tolerance
ECOARSEN = 0.046,
$END

```

```

$DCFGLB
DQUAL = 1.0, !acceptable donor stencil quality
MORFAN = 1, !enable wall region stencil repair
NORFAN = 20, !number of points subject to repair
$END

$GBRICK !off-body grid generation
OBGRIDS = .T.,
OFRINGE = 2, !3rd-order spatial (use 3 for 5th-order)
DFAR = 180, !far-field
DS = 0.1, !local spacing
CHRLLEN = 1.0, !characteristic length (chord)
XNCEN = 0,
YNCEN = 0, !center of off-body grid
ZNCEN = 0,
$END

$NBINP
REFLVL_DEFAULT = 1, !refine only off-body cartesian grids
$END

$BRKINP !user-specified refinement regions
NBRICK = -3, !must specify 3 regions
XBRKMIN (1) = -10.95,
XBRKMAX (1) = 10.95,
YBRKMIN (1) = -10.95, !near-wake grid
YBRKMAX (1) = 10.95,
ZBRKMIN (1) = -6.843,
ZBRKMAX (1) = 0.912,
BRKLVL (1) = -1, !grid level (use - for refinement)
DELTAS (1) = 0.0,
IBDYTAG (1) = 0,
XBRKMIN (2) = 0.85,
XBRKMAX (2) = 9.65,
YBRKMIN (2) = -1.5, !near-wake grid
YBRKMAX (2) = 0.5,
ZBRKMIN (2) = -1.0,
ZBRKMAX (2) = 1.0,
BRKLVL (2) = -2, !grid level (use - for refinement)
DELTAS (2) = 0.0,
IBDYTAG (2) = 0,
XBRKMIN (3) = 8.30,
XBRKMAX (3) = 9.50,

```

```

YBRKMIN (3) = -4.30, !vortex refinement 3
YBRKMAX (3) = 0,
ZBRKMIN (3) = -0.30,
ZBRKMAX (3) = 0.20,
BRKLVL (3) = -4,
DELTAS (3) = 0.0,
IBDYTAG (3) = 0,
!Refinement Regions
REFLVL (1) = -2,
XREFMIN (1) = -10.95,
XREFMAX (1) = 10.95,
YREFMIN (1) = -10.95, !near-wake grid
YREFMAX (1) = 10.95,
ZREFMIN (1) = -6.843,
ZREFMAX (1) = 0.912,
REFINOUT(1) = "OUTSIDE", !limit grid level in far-wake
$END

$GROUPS !load balancing
USEFLE = .F.,
MAXNB = 0,
MAXGRD = 0,
WGHTNB = 1.0, !weight factor for near-body grids
$END

$SPLITM
!XFILE = 'x_plane',
QFILE = 'planes/q',
NSAVE = 5,
IPRECIS = 1,
IG(1) = 4
JS(1) = 1, JE(1) = -1,
KS(1) = 1, KE(1) = -1,
LS(1) = 1, LE(1) = -1,
IG(2) = 5
JS(2) = 1, JE(2) = -1,
KS(2) = 1, KE(2) = -1,
LS(2) = 1, LE(2) = -1,
IG(3) = 6
JS(3) = 1, JE(3) = -1,
KS(3) = 1, KE(3) = -1,
LS(3) = 1, LE(3) = -1,
IG(4) = 7

```

```
JS(4) = 1, JE(4) = -1,  
KS(4) = 1, KE(4) = -1,  
LS(4) = 1, LE(4) = -1,  
IG(5) = 8  
JS(5) = 1, JE(5) = -1,  
KS(5) = 1, KE(5) = -1,  
LS(5) = 1, LE(5) = -1,  
$END  
  
$XRINFO  
IDXRAY = 1,  
IGXLIST = -1, !body ID for cutting (-1 for off-body)  
XDELTA = 0.075, !begin outside boundary layer  
$END  
  
$FLOINP  
FSMACH = 0.0, !uniform inflow  
REFMACH = 0.26, !tip mach number  
ALPHA = -90.0,  
BETA = 0.0,  
REY = 272000,  
TINF = 524.5, !temperature (R)  
$END  
  
$VARGAM $END !uniform gas constant  
  
$GRDNAM  
NAME = 'Blade',  
$END  
  
$NITERS $END !no sub-iterations per grid  
  
$METPRM  
IRHS = 0, !RHS: central differencing  
ILHS = 2, !LHS: beam warming  
IDISS = 3, !dissipation scheme  
BIMIN = 1.0, !disable low-mach pre-conditioning  
$END  
  
$TIMACU  
ITIME = 3, !constant CFL value  
CFLMAX = 10,  
$END
```

```

$SMOACU
SMOO = 1.0, !reduce smoothing in low-speed regions
DIS2 = 2.0, DIS4 = 0.04, !smoothing coefficients
FSO = 5, !central differencing order of accuracy
$END

```

```

$VISINP
VISC = .T.,
IDES = 2, !delayed detached eddy simulation
IRC = 1, !Spalart/Shur RC correction
$END

```

```

$BCINP
IBTYP = 5, 10,
IBDIR = 3, 1,
JBCE = -1, 1,
KBCE = -1, -1,
LBCE = 1, -1,
$END

```

```

$SCEINP $END !no need for species continuity
$SIXINP $END !no body motion

```

```

$GRDNAM !root defaults to blade grid parameters
NAME = 'Root',
$END

```

```

$NITERS $END
$METPRM $END
$TIMACU
ITIME = 3, CFLMAX = 5.0,
$END

```

```

$SMOACU $END
$VISINP
VISC = .T.,
IDES = 2, !delayed detached eddy simulation
IRC = 1, !Spalart/Shur RC correction
$END

```

```
$BCINP
IBTYP = 5,
IBDIR = 3,
JBCS = 1,
JBCE = -1,
KBCS = 1,
KBCE = -1,
LBCS = 1,
LBCE = 1,
$END

$SCEINP $END
$SIXINP $END
$GRDNAM !tip defaults to blade grid parameters
NAME = 'Tip',
$END

$NITERS $END
$METPRM $END
$TIMACU
ITIME = 3, CFLMAX = 5.0,
$END

$SMOACU $END
$VISINP
VISC = .T.,
IDES = 2, !delayed detached eddy simulation
IRC = 1, !Spalart/Shur RC correction
$END

$BCINP
IBTYP = 5,
IBDIR = 3,
JBCS = 1,
JBCE = -1,
KBCS = 1,
KBCE = -1,
LBCS = 1,
LBCE = 1,
$END

$SCEINP $END
```

\$SIXINP \$END

\$GRDNAM

NAME = 'Cut plane 1',

\$END

\$NITERS \$END

\$METPRM \$END

\$TIMACU \$END

\$SMOACU \$END

\$VISINP \$END

\$BCINP \$END

\$SCEINP \$END

\$SIXINP \$END

\$GRDNAM

NAME = 'Cut plane 2',

\$END

\$NITERS \$END

\$METPRM \$END

\$TIMACU \$END

\$SMOACU \$END

\$VISINP \$END

\$BCINP \$END

\$SCEINP \$END

\$SIXINP \$END

\$GRDNAM

NAME = 'Cut plane 3',

\$END

\$NITERS \$END

\$METPRM \$END

\$TIMACU \$END

\$SMOACU \$END

\$VISINP \$END

\$BCINP \$END

\$SCEINP \$END

\$SIXINP \$END

\$GRDNAM

NAME = 'Cut plane 4',

\$END

\$NITERS \$END

\$METPRM \$END


```
$TIMACU $END  
$SMOACU $END  
$VISINP $END  
$BCINP $END  
$SCEINP $END  
$SIXINP $END
```

```
$GRDNAM  
NAME = 'Cut plane 5',  
$END  
$NITERS $END  
$METPRM $END  
$TIMACU $END  
$SMOACU $END  
$VISINP $END  
$BCINP $END  
$SCEINP $END  
$SIXINP $END
```

```
$GRDNAM !off-body grids must be adjusted  
NAME = 'Off-body grids',  
$END
```

```
$NITERS $END  
$METPRM  
IRHS = 0, !RHS: central differencing  
ILHS = 2, !LHS: beam warming  
IDISS = 3, !dissipation scheme  
$END
```

```
$TIMACU  
ITIME = 1, !local time step scaling  
DT = 2., !time step factor  
CFLMIN = 1.0,  
CFLMAX = 100.0,  
$END
```

```
$SMOACU  
SMOO = 0.0,  
DIS2 = 0.0, DIS4 = 0.02, !adjust smoothing coefficients  
FSO = 5, !central difference order of accuracy  
$END
```

```

$VISINP
VISC = .T., !include all viscous terms
IDES = 2, !detached eddy simulation
IRC = 1, !rotational curvature correction term
$END

$BCINP $END
$SCEINP $END

```

D.2 Configuration File (Config.xml)

```

<?xml version='1.0' encoding='utf-8'?>
<!DOCTYPE Configuration [
<!ENTITY te "4.7153"> <!--wake age of the TE with axis at 0.25c -->
]>

<Configuration AngleUnit="degree">

<Component Name="Blade" Type="struc">
<Data> Grid List=1-3 </Data>
<Transform>
<Rotate Center="0.0, 0.0, 0.0" Axis="1.0, 0.0, 0.0" Angle="4.5" />
</Transform>
</Component>

<Component Name="Plane 1" Type="struc">
<Data> Grid List=4 </Data>
<Transform>
<Rotate Center="0.0, 0.0, 0.0" Axis="0.0, 0.0, -1.0" Angle="&te; + 2" />
</Transform>
</Component>

<Component Name="Plane 2" Type="struc">
<Data> Grid List=5 </Data>
<Transform>
<Rotate Center="0.0, 0.0, 0.0" Axis="0.0, 0.0, -1.0" Angle="&te; + 4" />
</Transform>
</Component>

```

```
<Component Name="Plane 3" Type="struc">
<Data> Grid List=6 </Data>
<Transform>
<Rotate Center="0.0, 0.0, 0.0" Axis="0.0, 0.0, -1.0" Angle="&te; + 7" />
</Transform>
</Component>

<Component Name="Plane 4" Type="struc">
<Data> Grid List=7 </Data>
<Transform>
<Rotate Center="0.0, 0.0, 0.0" Axis="0.0, 0.0, -1.0" Angle="&te; + 10" />
</Transform>
</Component>

<Component Name="Plane 5" Type="struc">
<Data> Grid List=8 </Data>
<Transform>
<Rotate Center="0.0, 0.0, 0.0" Axis="0.0, 0.0, -1.0" Angle="&te; + 15" />
</Transform>
</Component>

</Configuration>
```

E. Fortran 90 Codes

E.1 DES Transient Data Averaging

```

program ads_avg
use p3dio_sp

implicit none

!general
integer :: f, fcount
character(len=7) :: fname

!file set
integer, parameter :: f1 = 21000, skip = 3, fmax = 23859
!integer, parameter :: f1 = 21984, skip = 3, fmax = 22884

!arrays
real(4), dimension(16) :: info
integer, dimension(:), allocatable :: ni, nj, nk
real(4), dimension(:), allocatable :: u_velocity, v_velocity, &
w_velocity, vr_velocity
real(4), dimension(:,:,:), allocatable :: U, V, W, Vr, Vt
real(4), dimension(:,:,:), allocatable :: Q, Q_sum, Q_rms, &
Q_rey, Q_avg

!write(*,'(A)',advance='no') 'Start, End: '
!read(*,*) f1, fmax
fcount = 0

!loop over files
do f = f1, fmax, skip

!count
fcount = fcount + 1

!read solution file at step number f
write(fname, '(A2,I5)') 'q.', f

```

```

call p3dread(fname, info, ni, nj, nk, Q, 's')

!intialize arrays
if (f.eq.f1) then
allocate(Q_sum(ni(1),nj(1),nk(1),size(Q,4),size(Q,5)))
allocate(U(ni(1),nj(1),nk(1),size(Q,4)))
allocate(V(ni(1),nj(1),nk(1),size(Q,4)))
allocate(W(ni(1),nj(1),nk(1),size(Q,4)))
allocate(Vr(ni(1),nj(1),nk(1),size(Q,4)))
allocate(Vt(ni(1),nj(1),nk(1),size(Q,4)))
allocate(Q_rms(ni(1),nj(1),nk(1),size(Q,4),3))
allocate(Q_rey(ni(1),nj(1),nk(1),size(Q,4),3))
allocate(Q_avg(ni(1),nj(1),nk(1),size(Q,4),size(Q,5)))
end if

!add solution to running total
Q_sum = Q_sum + Q
write(*,*) fcount

end do !file

!average transient solution
Q_avg = Q_sum/fcount

!prepare array for transient velocity
allocate(u_velocity(fcount))
allocate(v_velocity(fcount))
allocate(w_velocity(fcount))
allocate(vr_velocity(fcount))
fcount = 0

!write solution to new file
call p3dwrite('Average.q', info, ni, nj, nk, Q_avg, 's')

!loop over files
do f = f1, fmax, skip

!read solution file at step number f
write(fname, '(A2,I5)') 'q.', f
call p3dread(fname, info, ni, nj, nk, Q, 's')
fcount = fcount+1

!write u_momentum

```

```

u_velocity(fcount) = Q(120,120,1,5,2)/Q(120,120,1,5,1)
v_velocity(fcount) = Q(120,120,1,5,2)/Q(120,120,1,5,1)
w_velocity(fcount) = Q(120,120,1,5,2)/Q(120,120,1,5,1)
vr_velocity(fcount) = u_velocity(fcount)*0.94138 - & v_velocity(fcount)*0.33735

!rewrite Q array
Q = Q - Q_avg

!write solution to new file
call p3dwrite('output/'//fname, info, ni, nj, nk, Q, 's')

!extract velocity components
U = Q(:, :, :, :, 2)/Q_avg(:, :, :, :, 1)
V = Q(:, :, :, :, 3)/Q_avg(:, :, :, :, 1)
W = Q(:, :, :, :, 4)/Q_avg(:, :, :, :, 1)

!project to planar coordinates
Vr(:, :, :, 1) = U(:, :, :, 1)*0.99314 - V(:, :, :, 1)*0.11694
Vt(:, :, :, 1) = -V(:, :, :, 1)*0.99314 - U(:, :, :, 1)*0.11694
Vr(:, :, :, 2) = U(:, :, :, 2)*0.98845 - V(:, :, :, 2)*0.15152
Vt(:, :, :, 2) = -V(:, :, :, 2)*0.98845 - U(:, :, :, 2)*0.15152
Vr(:, :, :, 3) = U(:, :, :, 3)*0.97917 - V(:, :, :, 3)*0.20305
Vt(:, :, :, 3) = -V(:, :, :, 3)*0.97917 - U(:, :, :, 3)*0.20305
Vr(:, :, :, 4) = U(:, :, :, 4)*0.96720 - V(:, :, :, 4)*0.25402
Vt(:, :, :, 4) = -V(:, :, :, 4)*0.96720 - U(:, :, :, 4)*0.25402
Vr(:, :, :, 5) = U(:, :, :, 5)*0.94138 - V(:, :, :, 5)*0.33735
Vt(:, :, :, 5) = -V(:, :, :, 5)*0.94138 - U(:, :, :, 5)*0.33735

!calculate root mean square of fluctuations
Q_rms(:, :, :, 1) = Q_rms(:, :, :, 1) + Vr**2
Q_rms(:, :, :, 2) = Q_rms(:, :, :, 2) + W**2
Q_rms(:, :, :, 3) = Q_rms(:, :, :, 3) + Vt**2

!calculate reynolds stress components
Q_rey(:, :, :, 1) = Q_rey(:, :, :, 1) + Vr*W
Q_rey(:, :, :, 2) = Q_rey(:, :, :, 2) + W*Vt
Q_rey(:, :, :, 3) = Q_rey(:, :, :, 3) + Vt*Vr

end do

!write rms solution to new file
Q_avg(:, :, :, 2:4) = sqrt(Q_rms/fcount)
call p3dwrite('RMS.q', info, ni, nj, nk, Q_avg, 's')

```

```
!write solution to new file
Q_avg(:, :, :, :, 2:4) = Q_rey/fcount
call p3dwrite('REY.q', info, ni, nj, nk, Q_avg, 's')

!write fluctuating velocity
open(10, file='u.dat', form='formatted')
do f=1,fcount
write(10,*) u_velocity(f)
end do

!write fluctuating velocity
open(10, file='v.dat', form='formatted')
do f=1,fcount
write(10,*) v_velocity(f)
end do

!write fluctuating velocity
open(10, file='w.dat', form='formatted')
do f=1,fcount
write(10,*) w_velocity(f)
end do

!write fluctuating velocity
open(10, file='vr.dat', form='formatted')
do f=1,fcount
write(10,*) vr_velocity(f)
end do

end program
```